NONTHERMAL PARTICLE PROPAGATION AND RADIATION IN SUPERNOVA REMNANTS

Xiaping Tang
Zhengzhou, China

B.A., Peking University, 2009

M.A., University of Virginia, 2011

A Dissertation Presented to the Graduate
Faculty of the University of Virginia
in Candidacy for the Degree of
Doctor of Philosophy

Department of Astronomy

University of Virginia
Aug, 2015

Roger Chevalier

ZhiYun Li

Phil Arras

Hank Thacker

Patrick Slane

Abstract

After a supernova (SN) explosion, the expanding ejecta drive a strong shock into the surrounding medium, creating a supernova remnant (SNR). Galactic SNRs are efficient particle accelerators. Nonthermal particles are accelerated in SNRs while propagating through the remnant shocks, and then produce nonthermal radiation. For core collapse supernovae, a magnetized spinning neutron star may be left behind after the SN explosion. The fast relativistic pulsar wind, powered by the spinning neutron star, drives a strong shock into the slow non-relativistic SN ejecta, producing a so-called pulsar wind nebula (PWN) which is characterized by nonthermal synchrotron and Inverse Compton emission. The study of nonthermal particle propagation and radiation in SNRs (including PWNe) is not only important for understanding the evolution of SNRs but also crucial for exploring the nature of cosmic ray (CR) origin. SNRs are believed to be the CR accelerators at least up to the knee of the CR spectrum ($\sim 10^{15}$eV). In this thesis, I present several pieces of work related to nonthermal particle propagation and radiation in SNRs (including PWNe).

In the first part of my thesis, I investigate particle transport in young PWNe such as the Crab Nebula. The classical toroidal magnetohydrodynamic (MHD) model for PWNe treats the shocked pulsar wind as an MHD flow. It successfully explained many observed features close to the central pulsar, including the termination shock and the jet-torus structure (e.g., Kennel & Coroniti 1984a; Del Zanna et al. 2006), but failed in the outer part of the nebula where more chaotic structure is present (e.g., Amato et al. 2000; Slane et al. 2004). To interpret the observed photon index distribution and shrinking nebular size, I propose a phenomenological advection and diffusion model for particle transport in young PWNe. In this model, advection dominates in the inner part of the nebula with toroidal structure, while diffusion dominates in the outer part of the nebula with chaotic structure. Monte Carlo simulations for the model provide good fits to the observed data. I also derive an analytical solution for particle transport with pure diffusion, which proves to be a good approximation for young PWNe in which toroidal structure is not significant.

Recent observations from both space-based GeV observatories and ground-based TeV observatories have revealed γ-ray emission consistent with a hadronic origin from several middle-aged SNRs interacting with molecular clouds (MCs) (e.g., SNR IC 443 and W44). To reveal the nature of the observed γ-ray emission and to identify the CR proton component from these middle-aged SNRs, I studied the interaction between a radiative SNR and MCs along with the associated particle acceleration in slow SNR shocks. I developed a 1-dimensional analytical model describing direct interaction between a radiative SNR, with a dense cooling shell, and clumpy MCs, with a moderate density interclump medium and high density molecular clumps. In the model, both the radiative shell and the clump interaction region contribute to the γ-ray emission, but the clump interaction region dominates the emission due to its higher density. I investigate diffusive shock acceleration (DSA) in the test particle limit, within the framework of re-acceleration of pre-existing CRs in slow SNR shocks, and derive the time-dependent solutions to the problem for both energy-independent diffusion and energy-dependent diffusion. By combining the time-dependent DSA solution and clump interaction model discussed above, the overall shape of the IC 443 and W44 spectra from GeV to TeV energies can be reproduced through pure pion-decay emission with a hadronic origin.

Acknowledgements

Time flies by. It is hard to believe that it's time to leave Charlottesville, the beautiful small town, and time to leave the astronomy department at UVA, with all the friendly and enthusiastic astronomers here. There are a lot of people who helped me through my 6 years' life here, I owe each of them a debt of gratitude.

At first I would like to show my greatest respect and gratitude to my advisor Roger Chevalier. Without him, I probably wouldn't become a astronomer and pursue this far. I was impressed by his constant patience and sustained support for my naive research ideas. I was also impressed by the angle he thinks about the scientific problems and the way he enjoys the research. I learned the way of thinking with scientific skepticism and the ability to carry out independent research.

Next I would like to sincerely thank my committee members ZhiYun Li, Phil Arras, Patrick Slane and Hank Thacker, for their helpful conversations and useful career advice. My special thank to Li for sharing your experience with me and providing constructive advice for my future research career.

My thanks to my cool and lovely office mates and fellow students, Tim Pennucci, Siraprapa Sanpa-arsa, Chris Irwin, Bin Chen, Bo Zhao, Charles Romero, Kristen Jones, Loreto Barcos, Guillermo Damke, Chenliang Huang, Meng Sun, Haifeng Yang, William Dirienzo, Rachael Beaton, Kimberly Sokal, Dom Pesce and Scott Suriano for building such a warm atmosphere in the department. I'm not a very talkative person, especially during work. But I really enjoy the time at the department with you guys. Special thanks to Tim Pennucci, Dom Pesce, Chris Irwin and Scott Suriano for reading my thesis and providing useful comments.

To my former and current roommates Chao Gu, Zukai Wang, Xiuchang Yang, Qiyang Qiao and Tianshu Li for being amazing friends and treating me as family. I feel lucky to have roommates like you guys and really cherish your friendship. I will never forget those good time and bad time we spent together.

To my old and new friends, Jiayao Zhou, Zebo Li, Xue Bai, Jun Yang, Meng Wang, Xiaotian and Zhengzheng Wang, for your company in several amazing trips to explore the beauty of nature, which further confirm my belief in studying astronomy. I really cherish your friendship and will never forget those magnificent views and splendid moments we shared together.

Finally, to my dad Baoquan, who was my childhood teacher and idol, and now is my friend and life mentor, for continuously encouraging me to pursue my dream in science. To my mom Meiwen, for being open minded about my scientific career and deep concern about my life. It might be hard to imagine, but most of the students in China don't have the freedom to choose their career by themselves. I feel lucky to have a family supporting me all the time. To my little sister, Hanqi, for always being a big fan of me. I'm really proud of you for taking care of dad and stepmother, when I'm not at home, and continuously bring joy to the family.

I would also like to thank the AAS travel grant for supporting my first conference to the IAU meeting in 2012 at Beijing.

Table of contents

List of Figures

List of Tables

Chapter 1

General Introduction

In this section I introduce the basics about cosmic rays (CRs), the evolution of supernova remnants (SNRs) (including pulsar wind nebulae) and particle acceleration in strong shocks. I start with a discussion of CRs, as one of the most important motivations for studying nonthermal particle propagation and radiation in SNRs is to reveal the CR origin.

1.1 Cosmic rays

The story of CR starts in the early 20th century, when puzzling ionization, inconsistent with radioactivity from the ground, was measured by scientists both in air and underwater. To reveal the nature of the mysterious ionizing radiation, Victor Hess carried out a series of ten balloon flights both in daytime and night from 1911 to 1913. The measured ionization rate in the atmosphere increases with altitude, indicating an extraterrestrial origin of the mysterious radiation source. To further rule out the Sun as the radiation source, he even performed a balloon experiment during a near-total eclipse in 1912 (see Schuster 2014 for a review). The term CRs was then coined for the source causing the mysterious ionizing radiation by Robert Millikan, who measured the CRs' induced ionization rate from deep under water to very high altitudes and believed that the CRs were primarily made of energetic photons (e.g., Amato 2014). Later, Clay (1927) suggested that CRs are primarily made of charged particles as the observed variations of CR intensity along latitude was consistent with charged particles being deflected by the geomagnetic field. Today we know that 99% of CRs are atomic nuclei, about 1% are electrons and a very small remaining fraction are antimatter, according to observations from space satellites, balloon flights in the upper atmosphere and ground-based telescopes (e.g., Abraham et al. 2010; Ahn et al. 2010; Adriani et al. 2011). Despite the fact that CRs are mainly particles, not photons, the name CRs has been kept.

Ever since their discovery, the study of CRs has been a very important topic in both physics and astronomy. It is a frontier of particle physics as it provides a unique opportunity for physicists to investigate the properties of a variety of particle species with energy far exceeding what can be achieved in a modern particle accelerator like the Large Hadron Collider. As astronomers, we are particularly interested in the mysterious origin and propagation of CRs in interstellar and intergalactic media, as well as their feedback in various astrophysical environments. By measuring the ratio between the flux from parent nuclei and the flux from those nuclei that can only be produced by spallation during CR propagation, astronomers found that the travel time of CRs in our Galaxy exceeds the ballistic time by several orders of magnitude (e.g., Blasi 2013), suggesting that CR particles travel diffusively through our Galaxy. The stochastic nature of diffusion hides the spatial information about the birth site of CR particles, so we can only use the energetic and spectral information of CRs to reveal their origin. This makes the identification of the origin of CRs a very difficult problem.

The all-particle spectrum of CRs shows an almost featureless broken power law above 30 GeV, below which solar modulation is important. The power law index steepens from -2.7 to -3.1 at $\sim 10^{15}$ eV (CR knee) and flattens at $\sim 10^{19}$ eV (CR ankle). The spectral break at the CR knee suggests a transition from Galactic sources to extragalactic sources. The chemical composition around the knee region shows an increase of heavy nuclei towards higher energy, which could be the result of a superposition of the cutoffs from the spectra of individual elements (e.g., Hörandel 2003, 2004). As many of the particle acceleration mechanisms are rigidity dependent (rigidity is defined as p/q in cgs units, with p being particle momentum and q being particle charge), which implies particles with charge Z can be accelerated to Z times higher energies. The highest energy particles, so-called ultra high energy cosmic rays (UHECRs), appear to manifest the GZK cutoff (Greisen 1966; Zatsepin & Kuz'min 1966) due to interactions between CRs and the cosmic microwave background radiation (CMB) photons

$$\gamma_{\rm CMB} + p \;\rightarrow\; \Delta^{+} \rightarrow p + \pi^{0}, \tag{1.1}$$

$$or \tag{1.2}$$

$$\gamma_{\rm CMB} + p \;\rightarrow\; \Delta^{+} \rightarrow n + \pi^{+} \tag{1.3}$$

where Δ^{+} is the Delta baryon composed of two up quarks and one down quark. Recent observations of different compositions in CRs with advanced instruments reveal more interesting features, such as spectral hardening around several hundreds GeV (e.g., Ahn et al. 2010; Adriani et al. 2011), a positron excess around several tens of GeV (e.g., Adriani et al. 2009; Aguilar et al. 2013), and an antiproton excess, which are beyond the scope of this discussion. For further information about the CR spectrum, see, for example, the review by Blasi (2013) and references therein.

Energetic particles with energies up to 10^{20} eV must be generated from very powerful astrophysical objects. Many candidates have been proposed as possible origins for very high energy CRs, including intergalactic shock fronts (e.g., Kang et al. 1996), γ-ray bursts (e.g., Mészáros 2007), active galactic nuclei (e.g., Berezhko 2008) and spinning magnetars (e.g., Fang et al. 2012). However, supernovae (SNe) and their remnants have long been considered to be the most promising CR accelerator for energies at least up to $\sim 10^{15}$ eV (CR knee), which marks the transition from Galactic to extragalactic CRs. Massive stars ($> 8\,{\rm M}_{\odot}$) end their lives with an energetic explosion (so-called SN). The ejecta released from the progenitor star drive a strong shock into the surrounding medium, creating a SNR. During the evolution of a SNR, part of the kinetic energy E_{kin} released by the supernova is transferred to the surrounding medium and is believed to accelerate the CR particles. SNe were first proposed as CR accelerators in Baade & Zwicky (1934), based on the energy budget. The observed CR energy density can be explained if SNe can transfer a few percent of their kinetic energy into the surrounding medium to accelerate particles. If we assume the SN explosion rate in our Milky Way is $\Lambda_{SN} \sim 1$ century^{-1}, each SN injects a kinetic energy $E_{kin} \sim 10^{51}$erg into the surrounding medium, the CR particles confined in our galaxy have an energy density $\zeta_{CR} \sim 1$eV cm^{-3} and an escape time $t_{esc} \sim 100$ Myr, then for our Galaxy with a radius of $R_{MW} = 15$ kpc and scale height of $H = 3$ kpc, the CR acceleration efficiency could be estimated

$$e = \frac{\pi R_{MW}^2 H \zeta_{CR}}{E_{kin} t_{esc} \Lambda_{SN}} \approx 10\%. \tag{1.4}$$

Nonetheless, to unambiguously establish SNe and their remnants as CR accelerators, it is necessary to identify energetic particles from them with spectra consistent with the observed CR spectrum, after taking propagation effects into account. In the last several decades, extensive efforts and exciting progress have been made in both observation and theory. In observations, energetic electrons have been identified in SNRs through detection of synchrotron radiation in both radio and X-ray wavelengths, which proves SNRs to be efficient particle accelerators (e.g., Reynolds 2008; Vink 2012). In theory, an efficient particle acceleration mechanism, diffusive shock acceleration (DSA) (e.g., Blandford & Eichler 1987), was proposed to explain CR acceleration in SNRs as it naturally produces a power law energy spectrum of energetic particles close to the observed CR spectrum, after taking propagation effects into account.

1.2 Evolution of SNRs

Historically, the expansion of a SNR in a homogeneous medium without consideration of magnetic field and relativistic particles has been divided into four discrete phases based on the dominant physical process and essential physical quantities that determine the dynamical evolution of the remnant: (1) an ejecta dominated (ED) phase, in which the SN ejecta mass $M_{ej} > M_{sw}$ the ambient medium mass swept up by the SN blast wave; (2) a Sedov-Taylor (ST) phase, in which $M_{sw} > M_{ej}$ while radiative losses are still not dynamically important (i.e. $\dot{E}_{rad}t \ll E_{kin}$); (3) a radiative phase, in which radiative cooling becomes dynamically important; and (4) a mixing phase, in which the shock velocity and postshock temperature become comparable with the turbulent velocity and temperature of the surrounding medium (e.g., Woltjer 1972). A complete description of the evolution of a SNR requires solving the general fluid equations, which incorporate various physical process, such as thermal conduction and viscosity, and taking into account various structures and states of the surrounding interstellar medium (ISM) or circumstellar medium (CSM). However, in limiting situations, where many physical variables can be neglected due to their limited effect on the SNR evolution and where there is no specific internal scale of the problem, the kinematics of the remnant $R(t)$ can be derived through dimensional analysis and follow a simple power law relation $R \propto t^{\beta}$. In addition, the set of partial differential fluid equations determining the system reduce to a set of ordinary differential equations which only depend on a dimensionless variable obtained through dimensional analysis. The dimensionless variable is then called the similarity variable of the system, and the solution to the reduced set of ordinary differential equations is then called the similarity solution of the problem which is considered to be the exact solution to the dynamical structure of the remnant under such idealized conditions.

In the next few paragraphs, I discuss how to derive the power law index β in the ejecta dominated phase, ST phase and radiative phase under extreme conditions.

In the early ED phase, when the unshocked ejecta dominate the remnant mass and energy (i.e. $M_{ej} \gg M_{sw}$ and $E_{ej} \approx E_{kin}$, where E_{ej} is the energy stored in the unshocked ejecta after the SN explosion), the dynamical evolution of a SNR is mainly characterized by the expansion of SN ejecta. Based on dimensional analysis

$$R = f_{ej}(E_{ej}, M_{ej}, t) = f_{ej}(E_{kin}, M_{ej}, t) \propto \left(\frac{E_{kin}}{M_{ej}}\right)^{0.5} t. \tag{1.5}$$

If we assume that the SN ejecta have a uniform density distribution, then detailed calculations give

$$R = \sqrt{\frac{10E_{kin}}{3M_{ej}}}t = 0.6\,\mathrm{pc}\left(\frac{E_{kin}}{10^{51}\ \mathrm{erg}}\right)^{0.5}\left(\frac{5\,\mathrm{M}_\odot}{M_{ej}}\right)^{0.5}\left(\frac{t}{100\,\mathrm{yr}}\right) \tag{1.6}$$

As the blast wave expansion velocity $u = dR/dt = const$, the ED phase is sometimes also referred to as the free expansion phase. When the SN ejecta collide with the surrounding ISM or CSM, both a forward shock running into the ambient medium and a reverse shock resulting from shocked SN ejecta are formed. In order to derive the above free expansion solution, we assume that the thickness of both the shocked ejecta layer and the shocked ambient medium layer are much smaller than the radius of the remnant. In addition, the forward shock velocity and reverse shock velocity are close to each other and to the velocity of the unshocked SN ejecta front. Thus the estimated kinetic relation in equation (1.6) for the unshocked SN ejecta front can be a very good approximation for the SNR forward shock.

As the remnant evolves, the two layer structure (shocked ejecta and shocked ambient medium) starts to affect the dynamical evolution of the SNR. The thickness, mass and energy of this shell region become significant compared to the value of the unshocked SN interiors. More importantly, the reverse shock velocity starts to deviate from the forward shock velocity and the velocity of the unshocked ejecta front. As a result, the kinematics of the SNR can no longer be described by the free expansion solution. A similarity solution is derived for this particular situation in Chevalier (1982), which is also referred to as the self-similar driven wave (SSDW) solution. In the SSDW solution, the two layer structure is self-similar. The thickness, mass and energy ratio, between the two shocked layers remain constant during the evolution, so we have

$$M_{sw} \propto M_{sej} \tag{1.7}$$

where M_{sej} is the shocked ejecta mass. If we assume the ejecta have a power law density profile $\rho_{ej} = t^{-3}(R/gt)^{-n}$ while the ambient medium density follows $\rho_a = qR^{-s}$ (here g and q are normalization constant), then the above equation becomes $\rho_{ej}R^3 \propto \rho_a R^3$. After some calculation, we obtain

$$R \propto \left(\frac{g^n}{q}\right)^{1/(n-s)} t^{(n-3)/(n-s)}. \tag{1.8}$$

The SSDW solution corresponds to a transition phase between the free expansion solution and the ST solution which we will discuss next. In order to derive the SSDW solution, the power law index of the ejecta and ambient medium must satisfy $s < 3$ and $n > 5$. When $s > 3$, the two layer structure undergoes accelerated expansion which is not a physical solution for the problem. When $n < 5$, the resulting solution in equation (1.8) has a power law index even steeper than the ST solution. Thus the remnant will evolve directly from the free expansion solution into the ST solution, as the SSDW solution doesn't exist for the SNR evolution in such cases. Chevalier

(1982) found that solution with $n = 7$ and $s = 0$ provides a reasonable fit to type Ia SNe while solutions with $s = 2$ could be applied to core collapse SNe.

As the remnant evolves further, the reverse shock starts to move back towards the remnant center and eventually sweeps up all the SN ejecta. Due to the Rayleigh-Taylor instability, the shocked ejecta and shocked ambient medium mix together and the contact discontinuity between them eventually vanishes. The remnant ends up with a forward shock and a mixed interior containing both shocked ejecta and shocked ambient materials. When the ambient medium swept up by the blast wave dominates the remnant mass and energy (i.e. $E_{SW} \approx E_{kin}$ and $M_{sw} \gg M_{ej}$, where E_{SW} is the energy transferred into the swept up ambient medium), then based on dimensional analysis

$$R = f_{SW}(E_{SW}, M_{sw}, t) = f_{SW}(E_{kin}, M_{sw}, t) \propto \left(\frac{E_{kin}}{M_{sw}}\right)^{0.5} t. \tag{1.9}$$

If the ambient medium follows a power law density distribution $\rho_a = qR^{-s}$, assuming $s < 3$ to ensure M_{sw} converges for a point explosion, then $M_{sw} \propto \rho_a R^3 \propto qR^{3-s}$. The resulting kinetic relation for the remnant radius becomes

$$R \propto \left(\frac{E_{kin}}{q}\right)^{1/(5-s)} t^{2/(5-s)}. \tag{1.10}$$

Defining the similarity variable $Rq^{1/(5-s)}/\ E_{kin}^{1/(5-s)}\, t^{2/(5-s)}$, the problem has a self-similar solution. When $s = 0$, the solution recovers the classical ST solution

$$R = 1.152 \left(\frac{E_{kin} t^2}{\rho_a}\right)^{1/5} = 5\mathrm{pc} \left(\frac{\mathrm{E_{kin}}}{10^{51}\,\mathrm{erg}}\right)^{1/5} \left(\frac{\mathrm{t}}{10^3\,\mathrm{yr}}\right)^{2/5} \left(\frac{1\mathrm{cm}^{-3}}{\rho_\mathrm{a}/\mathrm{m_p}}\right)^{1/5} \tag{1.11}$$

derived by Sedov and Taylor, with the specific heat ratio $\gamma = 5/3$. m_p is the proton mass in cgs units. Unless specifically noted otherwise, when I mention the ST solution I'm referring to the general solution corresponding to equation (1.10) for arbitrary s.

In the late ST phase, the evolution of the remnant follows the ST solution.

In the radiative phase, the dynamical evolution of the SNR is characterized by a dense shell formed in the outer part of the remnant as a result of radiative cooling. The hot gas in the interior of the remnant then pushes the shell outward, and the remnant enters the so-called pressure-driven snowplow stage. The expansion of the shell is determined by the equation

$$4\pi R^2(P - P_0) = \frac{d(M_{sh}u)}{dt} \tag{1.12}$$

where P is the pressure of the hot interior gas, P_0 is the pressure of the ambient medium (which is negligible compared with P), $u = dR/dt$ is the blast wave velocity, and $M_{sh} \approx M_{sw} = 4\pi\rho R^3/3$ is the shell mass. If we assume that the radiative cooling of the hot interior gas is negligible and that the hot interior gas undergoes adiabatic expansion, then we have $PV^\gamma = const$, where V is the remnant volume and $\gamma = 5/3$ is the specific heat ratio. Plugging it into eq (1.12) and assuming ρ is constant, we obtain $R \propto t^{2/7}$. As the remnant evolves, the pressure P of the hot interior gas decreases with time. When P eventually becomes dynamically negligible, the remnant enters the so-called momentum-conserving snowplow stage, which is described by the equation $d(M_{sh}u)/dt = 0$. If we again assume that ρ is constant for the ambient medium, then the remnant radius $R \propto t^{1/4}$. Cioffi et al. (1988) investigated the evolution of a SNR in the radiative phase in a homogeneous uniform medium with numerical simulations. They found that a simple offset power law relation

$$R = R_{PDS}\left(\frac{4t}{3t_{PDS}} - \frac{1}{3}\right)^{3/10} \tag{1.13}$$

provides a better fit to the numerical simulation results than the relation $t \propto t^{2/7}$

derived above for radiative SNRs (see Cioffi et al. 1988 for the definition of R_{PDS} and t_{PDS}). Cioffi et al. (1988) also claim that in most cases the remnant starts to mix with the ISM before it reaches the momentum-conserving snowplow stage.

The above framework provides deep insight into the physics behind the problem and also offers a convenient way to model the expansion of the SNR. Despite the fact that the various power law relations $R \propto t^{\beta}$ discussed above are only valid under idealized conditions, as a first order approximation a piece-wise power law relation made by connecting them together still offers a decent description of the SNR evolution. Detailed comparison between observation and theoretical modeling, however, still requires a unified model with smooth and accurate modeling of the transition among different limiting cases (e.g., Truelove & McKee 1999).

In the above discussion, we did not take a magnetic field into account, which is probably a good assumption for the global expansion of the remnant. As a SNR evolves in an ambient medium with ambient magnetic field B_0, the ratio between the accumulated magnetic energy in the swept up material and the SN kinetic energy E_{kin} satisfies

$$\left(\frac{B_0^2 R^3}{6E_{kin}}\right) = 0.1\% \left(\frac{B_0}{5\,\mu\mathrm{G}}\right)^2 \left(\frac{R}{20\,\mathrm{pc}}\right)^3 \left(\frac{10^{51}\ \mathrm{erg}}{E_{kin}}\right). \tag{1.14}$$

So the magnetic field is only important for the global dynamical evolution of large old remnants with a strong ambient magnetic field. Besides, a magnetic field can affect the morphology and dynamical structure of small regions with a locally enhanced and concentrated magnetic field. Balsara et al. (2001) did 3D MHD simulations of SNR evolution through the ST phase and found that the magnetic field doesn't affect the dynamical evolution of the remnant in the non-radiative phase.

Particle acceleration within the remnant might also affect its evolution. It will be discussed in detail in section 1.4.

Recently SNR evolution in an inhomogeneous medium has been studied with 3D numerical simulations, but with a focus on SNR feedback into the ISM such as the momentum injected into the surrounding medium by the SN (Martizzi et al. 2014; Kim & Ostriker 2015). Both works found that the evolution of a SNR in an inhomogeneous medium is qualitatively similar to the homogeneous case with the same mean density, but quantitatively different.

1.3 Pulsar wind nebula

In the last section, I discussed the evolution of SN ejecta in the surrounding CSM or ISM. For core collapse SNe, the evolution of its remnant is more complicated due to the formation of a neutron star at the center of the remnant (Baade & Zwicky 1934). A neutron star formed during the SN explosion inherits a significant amount of magnetic flux and angular momentum from the progenitor star, and ends up with a fast spin and strong magnetic field. In addition, emission from the neutron star is highly beamed. As a result, the emission from such a fast spinning magnetized neutron star is characterized by strongly pulsed emission. Neutron stars were first discovered observationally through such pulsed emission (Hewish et al. 1968), leading to the term pulsar.

A pulsar wind nebula (PWN) is created when the relativistic magnetized wind induced by the pulsar runs into the non-relativistic freely expanding ejecta. Both a forward shock towards the SN ejecta and a reverse shock (so-called termination shock) towards the pulsar form during the interaction. The PWN is a combination of both the shocked cold SN ejecta and the shocked pulsar wind. Due to magnetic Rayleigh-Taylor instability, the two shocked layers interpenetrate, producing the filamentary structures observed in the outer part of the PWN (Hester et al. 1996). While the optical line emission in the PWN is produced by the shocked SN ejecta materials, relativistic particles in the shocked pulsar wind interact with wound up magnetic field lines, resulting in the emission of non-thermal synchrotron radiation from radio to soft γ-ray. The same population of relativistic particles further up-scatters the synchrotron photons and photons from other radiation fields, like the cosmic microwave background (CMB), producing Inverse Compton (IC) emission in γ-rays. As synchrotron radiation and IC emission have different dependencies on the magnetic field, by comparing the intensity of synchrotron and IC emission we can estimate the magnetic field in the PWN.

1.3.1 Pulsar

Pulsars are the engines powering PWNe, and they are also the source of relativistic particles and magnetic fields for PWNe. The spin period T and spin-down rate $\dot{T} = dT/dt$ are two key observational quantities for a pulsar, which provide rich information about its intrinsic physical properties and time evolution, as temperature and absolute magnitude (luminosity) do for stars.

The pulsar spin-down luminosity is a measure of its rotational energy E_{rot} dissipation rate

$$\dot{E} = -\frac{dE_{rot}}{dt} = 4\pi^2 I \frac{\dot{T}}{T^3} \tag{1.15}$$

where I is the neutron star's moment of inertia and takes on a value of $\sim 10^{45}\,\mathrm{g\,cm^2}$ for a neutron star with a mass of $1.4\,\mathrm{M_\odot}$ and a radius of 10 km. Observational values of $\dot{E}$ vary from $\sim 5\times10^{38}$ erg s^{-1} to $\sim 3\times10^{28}$ erg s^{-1} (Manchester et al. 2005).

If we assume that the angular velocity Ω of a pulsar decays with the relation $\dot{\Omega} = -k\Omega^n$, where k is a constant and n is the braking index, then the age of a pulsar with initial period T_0 becomes

$$t = \frac{T}{(n-1)\dot{T}}\left[1 - \left(\frac{T_0}{T}\right)^{n-1}\right], \tag{1.16}$$

when $n \neq 1$. For the case where $T_0 \ll T$ and the rotational energy of pulsar is dissipated through magnetic dipole radiation (i.e. $n = 3$), the above expression simplifies to

$$t_c = \frac{T}{2\dot{T}}, \tag{1.17}$$

which is defined as the characteristic age of a pulsar.

For magnetic dipole radiation, with $\dot{E}_{rad} = -dE_{rot}/dt$, we obtain (Lorimer & Kramer 2012)

$$B = \left(\frac{3c^3 I}{8\pi^2 R^6 \sin^2\vartheta}\right)^{1/2} (T\dot{T})^{1/2} \tag{1.18}$$

where R is the neutron star radius and ϑ is the angle between the magnetic dipole and the rotation axis.

In theory, we are particularly interested in the evolution of pulsar spin-down power, which serves as the engine for the pulsar wind. If we assume that the initial spin-down luminosity of the pulsar $\dot{E}_0$ and the braking index n are constant, then (Pacini & Salvati 1973)

$$\dot{E} = \dot{E}_0\left(1 + \frac{t}{t_0}\right)^{-\frac{n+1}{n-1}} \tag{1.19}$$

where $t_0 = T_0/(n-1)\dot{T}_0$ is the initial characteristic timescale for the pulsar. At early times (when $t \ll t_0$) the pulsar spin-down luminosity $\dot{E}$ remains constant, while at late times (when $t \gg t_0$), the pulsar spin-down luminosity decreases rapidly as $\dot{E} \propto t^{-(n+1)/(n-1)}$.

For more information about pulsars see, e.g., Lorimer & Kramer (2012) and references therein.

1.3.2 Evolution of a PWN

If the pulsar kick velocity (due to asymmetric collapse during SN explosion) is negligible and the expansion of PWN and SNR follow spherical symmetry, then the evolution of a PWN can be divided into 3 different phases: supersonic expansion phase, reverse shock interaction phase and subsonic expansion phase (e.g., Reynolds & Chevalier 1984; van der Swaluw et al. 2004; Gelfand et al. 2009).

In the supersonic expansion phase, the relativistic magnetized pulsar wind drives a strong shock in the freely expanding SN ejecta, producing a PWN with both a bubble of shocked pulsar wind and a thin shell of shocked cold SN ejecta. The evolution of the PWN radius at this stage mainly depends on three physical quantities: pulsar luminosity $\dot{E}$, PWN age t and the density of freely expanding SN ejecta ρ_{ej}. Based on dimensional analysis

$$R \propto \left(\frac{\dot{E}t^3}{\rho_{ej}}\right)^{1/5}. \tag{1.20}$$

If we assume that the SN ejecta have a uniform density, then $\rho_{ej} \propto M_{ej}^{5/2}/E_{kin}^{3/2}\,t^3$. For spherical expansion, a similarity solution for this stage is discussed in Chevalier (1977) and Reynolds & Chevalier (1984). Detailed calculations show (Chevalier 1977)

$$\begin{aligned} R &= 1.5\dot{E}^{1/5}\,E_{kin}^{3/10}\,M_{ej}^{-1/2}\,t^{6/5} & (1.21)\\ &= 2\mathrm{pc}\left(\frac{\dot{\mathrm{E}}}{10^{38}\ \mathrm{erg\ s^{-1}}}\right)^{1/5}\left(\frac{\mathrm{E_{kin}}}{10^{51}\mathrm{erg}}\right)^{3/10}\left(\frac{3\,\mathrm{M_\odot}}{\mathrm{M_{ej}}}\right)^{1/2}\left(\frac{\mathrm{t}}{10^3\mathrm{yrs}}\right)^{6/5}, & (1.22)\end{aligned}$$

which implies that the PWN undergoes accelerated expansion in the early phase of evolution. If the pulsar has a large kick velocity, it will be offset from the remnant center. In the supersonic phase, the sound speed in the shocked relativistic pulsar wind bubble is close to the speed of light, which is much larger than the PWN expansion velocity. As a result, pressure perturbations in the PWN are balanced rapidly. The PWN/SNR system ends up with a pulsar located near the center of the PWN, which is offset from the remnant center.

As I already discussed in section 1.2, when the SN ejecta run into the surrounding medium, both a forward shock and a reverse shock are created. In the observer's frame, the reverse shock at first expands outward, but eventually moves inward when the SNR evolves from the free expansion phase to the ST phase. In the absence of a PWN, the reverse shock reaches the SNR center at (Reynolds & Chevalier 1984):

$$t_{rev} \approx 7 \left(\frac{M_{ej}}{10\,\mathrm{M}_\odot} \right)^{5/6} \left(\frac{E_{kin}}{10^{51}\mathrm{ergs}} \right)^{-1/2} \left(\frac{n_0}{1\,\mathrm{cm}^{-3}} \right)^{-1/3} \mathrm{kyr} \tag{1.23}$$

if a constant ambient medium density n_0 is assumed. When a PWN is present within the remnant, the SNR reverse shock inevitably collides with the fast expanding PWN forward shock. Then the reverse shock interaction phase starts. Due to reverberations of the SNR reverse shock, the PWN experiences oscillations between expansion and compression which can last for several thousands of years before it relaxes and reaches balance with the SNR interior (van der Swaluw et al. 2004). In the reverse shock interaction phase, Rayleigh-Taylor instabilities can develop and lead to the mixing of the SN ejecta and the pulsar wind materials, which can further produce the observed filamentary structure with complex morphology (Blondin et al. 2001). If the pulsar has a large velocity, the PWN is offset from the remnant center when the reverse shock starts to collide with the PWN forward shock. During the oscillation phase, the pulsar can possibly be stripped away from the PWN when it contracts, or reenter the PWN when it expands (Gelfand et al. 2009). This results in a radio-bright relic

PWN, which consists of mixed SN ejecta and pulsar wind materials, and an X-ray bright new PWN, which is offset from the relic PWN.

After the reverse shock interaction stage, the reverberation of the reverse shock almost vanishes and the PWN starts to expand subsonically in the SNR ejecta heated by the reverse shock, which has a much higher sound speed. The evolution of the PWN in this stage is characterized by pressure balance between the PWN and the surrounding shocked SN ejecta, i.e. $P_{PWN} = P_{SNR}$. Depending on whether $t/t_0 < 1$ or $t/t_0 > 1$ in equation (1.19), the evolution of the PWN has two possible solutions. If $t/t_0 < 1$, the pulsar spin-down luminosity L remains constant. The pressure in the PWN satisfies $P_{PWN} \propto Lt/R^3_{PWN}$. Combining this with the pressure of the shocked SN ejecta in the ST phase $P_{SNR} \propto E_{kin}/R^3_{SNR}$, we obtain (van der Swaluw et al. 2001)

$$R_{PWN} \propto \left(\frac{Lt}{E_{kin}}\right)^{1/3} R_{SNR} \propto \left(\frac{Lt}{E_{kin}}\right)^{1/3} \left(\frac{E_{kin}t^2}{\rho_a}\right)^{1/5} \propto t^{11/15}, \tag{1.24}$$

assuming the ambient medium has a uniform density distribution. If $t/t_0 > 1$, the PWN undergoes adiabatic expansion and its pressure satisfies $P_{PWN} \propto (R^{-3}_{PWN})^{\gamma} \propto R^{-4}_{PWN}$. After some calculation, one obtains (Reynolds & Chevalier 1984)

$$R_{PWN} \propto t^{3/10}. \tag{1.25}$$

According to the above discussion, PWNe in this subsonic expansion stage experience decelerated expansion which implies that a pulsar with a large kick velocity will eventually escape from the original wind bubble and SNR. As the sound speed of the shocked SN ejecta decreases with radius from the remnant center, the pulsar's motion within the SNR eventually becomes supersonic again. The pulsar will drive a bow shock with cometary morphology through the SNR interior (Blondin et al. 2001; van der Swaluw et al. 2004; Gelfand et al. 2009).

In this thesis, I focus on young PWNe in which the SNR reverse shock has not yet interacted with the PWN. For more information about the evolution of PWNe, see, e.g., Gaensler & Slane (2006) and references therein.

1.4 Particle acceleration

Diffusive shock acceleration (DSA), which is a form of first-order Fermi acceleration, is the particle acceleration mechanism believed to occur in most astrophysical environments involving strong shocks. It is also by far the most successful mechanism for CR acceleration in SNRs, as it produces a uniform power law spectrum close to the observed CR spectrum after taking into account propagation effects. In DSA, energetic particles around the shock front interact with the self-generated magnetohydrodynamic (MHD) turbulence and undergo pitch-angle scattering. To see the shock front as a discontinuity, the energetic particles need to have a gyroradius larger than the thickness of the shock transition layer. Such energetic seed particles could be either extracted from the shock-heated thermal particles in the downstream region or come from a pre-existing population of energetic particles in the upstream region. The acceleration of nonthermal particles at the shock front is regulated by the self generated MHD turbulence. The particles with the highest energy can escape the system and be injected into the ISM. Understanding CR escape is important in exploring CR acceleration in SNRs. Particles that stay within the remnant until the mixing phase suffer extreme energy loss due to expansion of the remnant, and thus won't be able to explain the CR spectrum up to the knee energy.

A complete description of CR transport in the turbulent shock environment with detailed kinetic theory is extremely difficult. But under certain assumptions the problem can be largely simplified without losing its essence, and an important analytical solution for the accelerated nonthermal particle spectrum becomes available.

Following the discussion in Drury (1983), if we assume that particles experience isotropic pitch-angle scattering imposed by the magnetic irregularities (scattering centres), then the particle transport in the fluid can be described simply by a diffusion equation

$$\frac{\partial f}{\partial t} = \nabla \cdot (\kappa \, \nabla f) \tag{1.26}$$

where $f(\vec{p}, \vec{r}, t)$ is the phase space density for the accelerated nonthermal particles. κ is the particle diffusion coefficient which depends on the process of pitch-angle scattering. When a shock is present, the scattering centers follow the advective motion of the fluid. As a result, the above diffusion equation becomes

$$\frac{\partial f}{\partial t} + \vec{U} \cdot \nabla f = \nabla \cdot (\kappa \, \nabla f), \tag{1.27}$$

where $\vec{U}$ is the velocity of the advective flow. To account for the convergence or divergence of the flow, an extra term, $(\nabla \cdot \vec{U}) \, p \partial f / 3 \, \partial p$ representing the particle adiabatic energy loss, should be included in the particle transport equation. However, for a uniform flow $\vec{U}$ is constant in space, and this term goes to 0. After taking into account the advection of the fluid, in order to maintain the isotropic pitch-angle scattering assumption, we require that the shock velocity $U \ll c$, the speed of light. Such a condition is naturally satisfied by the non-relativistic shock in SNRs. So far we have assumed that the scattering centers are frozen into the fluid. In reality, the scattering centers have a random velocity on the order of the Alfven velocity, V_A, relative to the background fluid motion. Because of this random component the particle momentum changes by a small amount on the order of $\Delta p \sim pV_A/v$ during each scattering, which gives rise to a diffusion term in momentum space due to the classical second-order Fermi acceleration. In SNRs, V_A is usually much smaller than U (the shock velocity), and the momentum diffusion term can be neglected. In summary, under the assumptions of isotropic pitch-angle scattering and in the limit $V_A \ll U \ll c$, we end up with the following advection and diffusion equation for the simplified particle transport when adiabatic energy losses are negligible

$$\frac{\partial f}{\partial t} + \vec{U} \cdot \nabla f = \nabla(\kappa \nabla f) + Q(\vec{p}, \vec{r}, t) \tag{1.28}$$

where $Q(\vec{p}, \vec{r}, t)$ is the source term for energetic seed particles.

The steady-state DSA spectrum can be obtained by solving above advection and diffusion equation with appropriate matching conditions. But here we follow the method in Bell (1978) to derive the accelerated nonthermal particle spectrum through investigating the microphysics that an energetic particle experiences when bouncing back and forth around the shock front. For simplification, we constrain our discussion to a one-dimensional parallel shock (magnetic field is parallel to the shock normal). Considering a relativistic particle bouncing back and forth across the shock discontinuity, every time the particle comes across the shock discontinuity, it receives an average momentum gain through pitch-angle scattering by the magnetic irregularities (Bell 1978)

$$\Delta p = 2(U_1 - U_2)p/3c, \tag{1.29}$$

where c is the speed of light. In this section, the subscripts 1 and 2 refer to upstream and downstream of the shock, respectively. The mean time taken for a particle to complete one cycle of back and forth motion is (Drury 1983)

$$\Delta t = 4\left(\kappa_1/U_1 + \kappa_2/U_2\right)/c. \tag{1.30}$$

Particles entering the downstream region have a chance to escape the DSA site and move to ∞ in the downstream region due to the advective flow towards ∞. The probability for a particle to not return to the acceleration site is given by the ratio between the flux of the downstream advective flow and the flux for particles experiencing random diffusion across the shock front (Drury 1983)

$$P_{esc} = \frac{nU_2}{nc/4} = \frac{4U_2}{c}, \tag{1.31}$$

where n is the downstream CR particle number density.

Based on the above discussion, the diffusion and advection equation can be further simplified to the following conservation equation for the total number of accelerated particles $N(E)$

$$\frac{\partial N(E)}{\partial t} = -\frac{\partial}{\partial E}\left[\frac{dE}{dt}N(E)\right] - \frac{P_{esc}N}{\Delta t} + Q(E) \tag{1.32}$$

where $dE/dt = 2c\Delta p/\Delta t$ is the energy gain rate for relativistic particles according to equation (1.29) and (1.30). Here we have already neglected the adiabatic energy loss term. The steady-state solution for the problem then can be solved easily and provides

$$N(E) = E^{-\alpha_E}\int^{E} Q(E')\, t_{acc}\, E'^{\alpha_E - 1} dE' \tag{1.33}$$

where

$$t_{acc} = \frac{E}{dE/dt} = \frac{3}{U_1 - U_2}\left(\frac{\kappa_1}{U_1} + \frac{\kappa_2}{U_2}\right) \tag{1.34}$$

is defined as the particle acceleration time and

$$\alpha_E = \frac{U_1 + 2U_2}{U_1 - U_2} = \frac{2 + r_c}{r_c - 1} \tag{1.35}$$

is the power law index for the steady-state DSA spectrum. Here r_c is the shock compression ratio, which only depends on the Mach number of the shock, and equals 4 for a strong shock. According to the above calculation, the shape of the resulting DSA spectrum is determined by the source spectrum when the source spectrum $Q(E)$ is flatter than $E^{-\alpha_E}$, and follows simple power law $E^{-\alpha_E}$ when the source particle spectrum $Q(E)$ is steeper than $E^{-\alpha_E}$. In addition, the shape of the accelerated nonthermal particle spectrum doesn't depend on the diffusion process, which is mainly because both the energy gain Δp and the escape probability P_{esc} are independent of κ. However the diffusion process is very important in determining the maximum attainable energy of the system, as the particle acceleration time t_{acc} does depend on κ.

So far we have assumed that the shock structure is not modified by the accelerated nonthermal particles, i.e. the flow velocity $U_{1,2}$ and diffusion coefficient $\kappa_{1,2}$ are independent of the particle distribution function $f(\vec{p}, \vec{r}, t)$. The advection and diffusion equation for the problem is linear and the system is in the so-called test particle limit. Recently, people have been focused on the study of nonlinear effects of diffusive shock acceleration (NLDSA). The dynamical back-reaction from the CR particles can modify the shock structure when the DSA is efficient and a significant amount of the shock kinetic energy is transferred to the accelerated particles. A CR precursor is formed ahead of the shock due to CR particles streaming upstream of the shock, and a subshock discontinuity is also formed (corresponding to the shock discontinuity in the test particle limit). The subshock has a smaller compression ratio than the shock compression ratio in the test particle limit, as the CR precursor tends to smooth the discontinuity induced by the subshock front. The total compression ratio, between the downstream region close to the subshock and the upstream region beyond the CR precursor, is larger than the shock compression ratio in the test particle limit, because energetic particles can escape from the DSA site and carry away the kinetic energy of the shock front. Due to the larger total compression ratio, the postshock temperature will be lower than in the test particle case. Because of the formation of the CR precursor, particles with higher energy can diffuse further away from the subshock front and thus experience higher compression. As a result, the accelerated nonthermal particles show a concave spectrum comparing with the test particle case. CR particles streaming in the upstream region suffer from instabilities that can transfer momentum to magnetic waves to amplify the magnetic field. Magnetic field amplification (MFA) is crucial for CR acceleration in SNRs, as a stronger magnetic field provides faster diffusion of CR particles, which can further increase the maximum attainable energy in SNRs to a value close to the CR knee energy. All of the predictions discussed above from NLDSA, lower downstream temperature (e.g., Helder et al. 2009), concave particle spectrum (e.g., Vink 2012) and MFA (e.g., Uchiyama et al. 2007) have already been confirmed by recent radio, optical and X-ray observations of several young SNRs, and they further support DSA as the CR acceleration mechanism in SNRs.

For further information about DSA and its application in SNRs, see e.g. reviews from Drury (1983); Blandford & Eichler (1987); Malkov & Drury (2001); Amato (2014) and references therein.

PWNe are also very efficient particle accelerators, according to observed synchrotron and Inverse Compton radiation, which can contribute to at least the leptonic component of CRs. Particle acceleration in PWNe involves relativistic shocks which are found to be hostile for the DSA described above. 3D particle-in-cell simulations show that DSA in a relativistic shock is inefficient unless the magnetic field is nearly parallel to the shock normal or the relativistic flow is weakly magnetized (Sironi & Spitkovsky 2009). However neither of these conditions is satisfied in PWNe. The jet-torus structure revealed in the Crab Nebula (Weisskopf et al. 2000) implies a strong toroidal field around the termination shock (TS), where the pulsar wind is slowed down and particles are accelerated. The magnetization parameter (defined to be the ratio between Poynting flux and kinetic energy) at the termination shock, derived through comparing simulation results with the observed jet-torus structure (Del Zanna et al. 2004), synchrotron and Inverse Compton emission (Del Zanna et al. 2006; Volpi et al. 2008), is also too high for applying DSA to interpret the observed acceleration efficiency in the Crab Nebula. Two alternative mechanisms have been proposed for particle acceleration at the TS: magnetic reconnection in the striped pulsar wind (Sironi & Spitkovsky 2011) and resonant absorption of ion-cyclotron waves in a ion-doped plasma (Amato & Arons 2006). Since the work described in this thesis doesn't involve particle acceleration in PWNe, I will not discuss about it in detail.

The remainder of this thesis is based on my work published in Tang & Chevalier (2012, 2014, 2015) with slight changes and updates, and summarized as follows. In Chapter 2, I present a phenomenological advection and diffusion model for particle transport in young PWNe and emphasize the role of diffusion in interpreting the observed spectral index distribution and nebular size behavior. In Chapter 3, the direct interaction between a radiative SNR and dense clumps is discussed and then used to interpret the observed hadronic emission from middle-aged SNRs interacting with MCs. For particle acceleration, re-acceleration of pre-existing CRs in the ambient medium through DSA and adiabatic compression are considered. While the observed GeV emission can be reproduced with a steady-state DSA solution, the TeV emission shows a spectrum requiring a time-dependent DSA solution. In Chapter 4, I derive a time-dependent DSA solution in the test particle limit, involving re-acceleration of pre-existing CRs. By applying the new time-dependent DSA solution for particle acceleration, the observed GeV and TeV emission can be explained consistently within the framework of direct interaction between the SNR and MCs. Chapter 5 discusses future work as a continuation of the thesis work presented here.

Chapter 2

Particle Transport in Young Pulsar Wind Nebulae

Tang, X., & Chevalier, R. A. 2012, ApJ, 752, 83

Abstract

The model for pulsar wind nebulae (PWNe), as a result of the magnetohydrodynamic (MHD) downstream flow from a shocked relativistic pulsar wind, has been successful in reproducing many features of the nebulae observed close to central pulsars. However, observations of well-studied young nebulae like the Crab Nebula, 3C 58, and G21.5-0.9 do not show the toroidal magnetic field on a larger scale that might be expected in the MHD flow model; in addition, the radial variation of spectral index due to synchrotron losses is smoother than expected in the MHD flow model. We find that pure diffusion models can reproduce the basic data on nebular size and spectral index variation for the Crab, 3C 58, and G21.5-0.9. Most of our models use an energy-independent diffusion coefficient; power-law variations of the coefficient with energy are degenerate with variation in the input particle energy distribution index

in the steady state, transmitting boundary case. Energy-dependent diffusion is a possible reason for the smaller diffusion coefficient inferred for the Crab. Monte Carlo simulations of the particle transport allowing for advection and diffusion of particles suggest that diffusion dominates over much of the total nebular volume of the Crab. Advection dominates close to the pulsar and is likely to play a role in the X-ray half-light radius. The source of diffusion and mixing of particles is uncertain, but may be related to the Rayleigh-Taylor instability at the outer boundary of a young PWN or to instabilities in the toroidal magnetic field structure.

2.1 Introduction

The finding of the diminishing size of the Crab synchrotron nebula with increasing frequency supports the picture that energetic electrons are injected in the vicinity of the pulsar and lose energy to synchrotron radiation in the larger nebula (Wilson 1972; Rees & Gunn 1974). The radial emission profiles were first modeled as a central particle source with diffusion into the larger nebula (Gratton 1972; Wilson 1972). Rees & Gunn (1974) specified a termination shock in the pulsar wind as the source of the particle acceleration and viewed the outer part of the nebula as a place where the pulsar magnetic field winds up and the flow decelerates. This view was put on a firmer basis by Kennel & Coroniti (1984a,b, hereafter KC), who calculated the conditions at the relativistic MHD shock and followed the time independent downstream flow of fields and particles. This 1-dimensional model with advected particles was able to reproduce the observed sizes of the optical and X-ray emission in the Crab Nebula, but did not address the radio emission.

High resolution imaging of the Crab with the *Hubble* Telescope at optical wavelengths and *Chandra* at X-ray wavelengths shows an active system of toroidal filaments and jets close to the pulsar in line with the expected position of the termination shock (Hester 2008). These observations have motivated 2-dimensional MHD simulations, which allow for a polar angle dependence of the pulsar wind power (Komissarov & Lyubarsky 2003; Del Zanna et al. 2004). In these models, the wind is stronger in the equatorial plane, producing the toroidal filaments. Hoop stresses in the shocked flow bring material back to the axis to form the jets. Current models for the filaments are able to reproduce many aspects of the filaments (see Bucciantini 2011, for a review), including the integrated spectrum of the Crab from radio to TeV (Volpi et al. 2008) and the time variability of the inner structure (Volpi et al. 2008; Camus et al.

2009; Komissarov & Lyutikov 2011). The jet-torus structure near the pulsar has been commonly observed in X-ray images of pulsar nebulae (Kargaltsev & Pavlov 2008), and the structure is presumed to be a standard feature of pulsar nebulae. Although models for the toroidal filaments are now convincing, the nature of the flow beyond the filaments to the edge of the nebula remains uncertain.

The primary way of exploring the particle transport is to model the structure of the nebulae at different photon energies or, equivalently, the structure and photon index distribution. The crucial point is that the particles lose energy to synchrotron radiation as they age so that the photon index distribution provides a good test of the particle transport mechanism. Provided the magnetic field is not strongly varying, the spectral index in a particular location gives information on the mean age of the particles. Observations of the Crab Nebula at optical (Veron-Cetty & Woltjer 1993) and infrared (Temim et al. 2006) wavelengths show a monotonic change in spectral index from the center to the edge of the nebula, where edge is defined by the decrease in surface brightness at that particular wavelength. The well-known bays in the Crab are asymmetric structures, but the spectral index at the bay edge is similar to that at other edges. The data do not indicate a highly asymmetric flow in the nebula. Thus, we assume spherical symmetry in our models.

In Section 2 of this paper, we discuss issues with existing models for the larger scale flow and, in Section 3, consider a diffusion/advection model for the particle propagation. The model is applied to the phase when the pulsar wind nebula (hereafter PWN) is expanding into the freely expanding supernova gas, before a reverse shock front moves in due to interaction with the surroundings. We concentrate on comparing our models to the Crab Nebula, 3C 58 and G21.5–0.9 because they are the best observed PWNe within that phase. In Section 4, we discuss the diffusion process.

2.2 Outer structure of young pulsar nebulae

Current data on the Crab Nebula convincingly show that there is a relativistic flow in the interior that must slow to match the outer boundary (Hester 2008). The issue treated in this paper is how the particles are transported between the inner, toroidal region and the outer boundary of the PWN. In the KC model, the particles are advected with a toroidal magnetic field. Cross field scattering of particles is expected to be small (e.g., de Jager & Djannati-Ataï 2009), so that diffusion of particles can be neglected. Problems with this model in reproducing the spectral index distributions in young PWNe have been raised (Reynolds 2003; Slane et al. 2004). This issue is discussed in detail in the next section. Here we note some other points relevant to the toroidal field model for the outer structure.

In the Crab Nebula, the X-ray emission is from a region close to the pulsar because of synchrotron burn-off. If one goes to optical wavelengths, where the particles have longer lifetimes, an analysis of the polarization shows that there are $3-6$ magnetic elements across the nebula with possible smaller scale structure (Felten 1974). Schmidt et al. (1979) find that magnetic structure in the Crab only extends down to about 20 arcsec, or 0.2 pc. Seward et al. (2006) presented deep *Chandra* images of the Crab, finding evidence for fingers with a roughly radial orientation; the spectral index structure implied rapid diffusion along the structures, presumably oriented along the magnetic field, and slow diffusion perpendicular to the fingers. The X-ray emitting particles in 3C 58 have longer lifetimes and imaging X-ray studies with *Chandra* show many magnetic loops without a clear toroidal structure, except close to the pulsar (Slane et al. 2004); the X-ray filaments are related to ones observed at radio wavelengths and with some optical filaments (thermal gas). Overall, there is little evidence for toroidal structure in pulsar nebulae except near the central pulsars. Two PWNe that do show evidence for toroidal field structure are the small nebula around the Vela pulsar (Dodson et al. 2003) and G106.6+2.9 (Kothes et al. 2006); however, these objects are probably in a different evolutionary stage than the Crab, without an unstable outer boundary (Chevalier & Reynolds 2011).

The Crab Nebula, with radio spectral index $\beta = 0.299 \pm 0.009$ (Baars et al. 1977) where flux $\propto \nu^{-\beta}$, shows little radio spectral index variation over the entire nebula, to within 0.01 (Bietenholz et al. 1997), although PWNe themselves show a range of spectral indices, e.g., 3C 58 has $\beta = 0.07 \pm 0.05$ (Bietenholz et al. 2001). There is no indication that the spectral index observed in the Crab is a universal value, so the uniformity of spectral index is surprising. G21.5–0.9 also has a fairly uniform radio spectral index image (Bietenholz & Bartel 2008), as well as 3C 58 (Bietenholz et al. 2001).

These observational considerations support the view that, although there is clearly toroidal structure where the pulsar wind impacts the larger nebula, the flow is more radial in the outer nebula and there is evidence for a mixing process. There are several possible reasons for the apparent mixing of energetic particles. The acceleration of the supernova ejecta by the pulsar bubble is Rayleigh-Taylor unstable (Chevalier 1977; Jun 1998; Hester et al. 1996). The structure observed in the thermal gas filaments in the Crab Nebula and other PWNe is likely due to this instability (Hester 2008), although there are still uncertainties about how the instability operates when the low density fluid is magnetized (Bucciantini et al. 2004; Stone & Gardiner 2007). As discussed by Hester et al. (1995), there is evidence in the Crab for magnetic field lines being 'draped' around thermal filaments and stretched in the radial direction. The

Crab filaments cover the velocity range $700 - 1500\,\mathrm{km\,s^{-1}}$ (Hester 2008).

Another possibility is the action of instabilities occurring at or near the pulsar wind termination shock (Begelman 1998; Camus et al. 2009; Mizuno et al. 2011). However, such instabilities may not be compatible with the apparent regular structure observed in the case of the newly formed nebula around the Vela pulsar (Dodson et al. 2003; Chevalier & Reynolds 2011). There may be feedback between instabilities near the termination shock and the outer boundary. In their axisymmetric numerical simulations, Camus et al. (2009) find that waves and vortices in the larger nebula feed back on the structure at the termination shock, which in turn generates more structure in the nebula. Camus et al. (2009) note that it is impossible to distinguish between the cause and the effect. In addition, some thermal gas from the supernova is entrained in the unstable region, explaining the optical filaments seen in association with nonthermal filaments in the Crab and 3C 58.

These observational and theoretical considerations show that, although the region close to the pulsar has a clear toroidal structure, the larger nebula has a complex structure that includes a radial component to the magnetic field. As summarized by Hester (2008), there are layers of magnetic fields folded on top of each other such that adjoining field lines in one place move away from each other. Although diffusion across magnetic field lines is expected to be small, even a small amount of cross field transport could result in thorough mixing, with this magnetic field configuration. We thus consider models with radial diffusion.

One uncertainty for the models is the degree to which particles are transmitted through the outer boundary of the PWN. The expectation is that the PWN magnetic field is contained within the wind bubble, which is bounded by supernova ejecta in young PWNe; the outer boundary of the Crab Nebula shows loop structures at radio wavelengths that are likely to delineate the magnetic field (Hester 2008). The characteristic mean free path for particles to cross the magnetic field is limited to the particle gyroradius (Bohm limit)

$$\lambda = 10^{-4} \left(\frac{E_e}{100\ TeV}\right) \left(\frac{B}{100\ \mu G}\right)^{-1}\ pc, \tag{2.1}$$

where the particle energy, E_e, corresponds to an energy of synchrotron radiation through $E_e = (20\ TeV)(B/100\ \mu G)^{-1/2} E_{keV}^{1/2}$ and B is the magnetic field. The escape time for Bohm diffusion from a region of size R is then (de Jager & Djannati-Ataï 2009)

$$t_{esc} \approx 16,000 \left(\frac{R}{2\ pc}\right)^2 \left(\frac{E_e}{100\ TeV}\right)^{-1} \left(\frac{B}{100\ \mu G}\right)\ yr, \tag{2.2}$$

which is long compared to the ages of the PWNe considered here ($\sim 10^3$ yr), particularly for particles radiating below X-ray wavelengths. However, there is some chance for escape from a narrow region close to the edge of the nebula.

An observational test for the transmission of particles would be synchrotron emission from energetic particles that have left the main PWN. There has been little evidence for such emission, but Bamba et al. (2010) have recently found X-ray emission around a number of PWNe, which they interpret as synchrotron emission from escaped particles. To have X-ray emitting particles extend to such large radial distances requires a surprisingly low magnetic field strength in order to avoid synchrotron losses. One of the PWNe discussed by Bamba et al. (2010) is G21.5–0.9, which is also one of the primary remnants treated here. However, there are other interpretations for the extended emission. Bocchino et al. (2005) attributed the emission to a combination of a dust scattering halo plus emission from a surrounding shell; Matheson & Safi-Harb (2010) have shown clear evidence for shell emission.

Escape of electrons and positrons from PWNe has also come up in the context of a possible source for features in the Galactic cosmic ray spectrum of electrons and positrons (e.g., Chang et al. 2008). However, the escape can be from elderly PWNe ($> 10^5$ yr old), and does not require escape from young objects like those discussed here (e.g., Malyshev et al. 2009). Hinton et al. (2011) suggested the escape of particles from the Vela X PWN to explain the steeper particle spectrum in the outer parts of the nebula; however, this is an older nebula that has likely been affected by the reverse shock wave (Blondin et al. 2001). Overall, particle escape in PWNe with ages $\sim 10^3$ yr does not appear likely. In Section 3.2, we model the effect of the outer boundary condition for the PWN.

In the early diffusion models for the Crab Nebula (Gratton 1972; Wilson 1972; Weinberg & Silk 1976), the diffusion coefficient was assumed to be constant with energy, and that is the assumption that we make in most of our modeling. Weinberg & Silk (1976) argued for a constant coefficient based on the fact that the diffusion length is likely to be related to the size of magnetic filaments and is much larger than the gyroradius. However, there are reasons to consider energy dependent diffusion of the form $D_E(E) = D_0 E^{\sigma}$, where σ is a constant. On the observational side, cosmic rays are known to diffuse from the Galaxy in an energy dependent way (e.g., Strong et al. 2007, and references therein). The data indicate $\sigma = 0.3 - 0.6$, with a diffusion coefficient of $(3 - 5) \times 10^{28}$ cm^2 s^{-1} at a reference particle energy of 1 GeV (Strong et al. 2007). Interstellar turbulence is thought to play a role in the energy dependent diffusion. Also, there is the possibility that the diffusion coefficient is proportional to the particle gyroradius, as in Bohm diffusion, leading to $\sigma = 1$. This “Bohm-type” value of σ is used by Van Etten & Romani (2011) and Hinton et al. (2011) in their modeling of evolved PWNe. However, the diffusion length is much larger than the particle gyroradius, so there is not a clear argument for $\sigma = 1$ in the PWN case. We consider the possible effect of energy dependent diffusion in Section 3.1.

2.3 Models with diffusion

2.3.1 Pure diffusion model

Wilson (1972) first showed that the spatial and spectral distribution of the Crab Nebula in the optical could be explained by a diffusion model with synchrotron radiation losses. Observations of 3C 58 (Bocchino et al. 2001; Slane et al. 2004) and G21.5-0.9 (Slane et al. 2000; Safi-Harb et al. 2001) taken by *Chandra* also gave a photon index distribution that is similar to the optical spectral index distribution in the Crab and is incompatible with the KC model (Reynolds 2003; Slane et al. 2004). Although observations of the Crab clearly show evidence for a relativistic wind close to the pulsar, a pure diffusion model illustrates one limiting case of the expected particle transport. We used the pure diffusion model developed by Gratton (1972) to fit the spectral index distribution of Crab from radio to optical, and 3C 58 and G21.5-0.9 in X-rays. We also used the model to calculate the half light radius of the Crab from radio to X-rays. This is the same model used by Wilson (1972) in his model for the Crab. The model assumes that a point source injects particles into an infinite space with spherical symmetry, and the injected particles follow a power law distribution $N(E, r = 0) = KE^{-p}$. The transport mechanism for the injected particles is diffusion. In order to satisfy the spherical symmetry assumption, the objects we discuss in this paper are young PWNe that are observed to have approximate spherical symmetry. In our initial model we have a pre-defined PWN radius R; when we calculate the half light radius and integrated spectrum, we only consider the particles that are within the nebular radius R, reasoning that the magnetic field in the freely expanding ejecta outside R is small. The model also assumes that the diffusion coefficient D and magnetic field B inside R are constant with radius. Here we neglect the adiabatic expansion energy losses and assume synchrotron radiation loss is the only energy loss, so that $dE/dt = -QE^2$, where $Q = 2.37 \times 10^{-3} B_\perp^2$ erg s^{-1} in cgs units and $B_\perp^2 = (2/3)B^2$ (Pacholczyk 1970). We examine the assumptions of point source injection, pure diffusion, and a reflecting boundary in Section 3.2. In this section we use this simple pure diffusion model to analyze the spectral index distribution and half light radius of PWNe.

Based on these assumptions, the number density distribution $N(E, r, t)$ is (Gratton 1972)

$$N(E, r, t) = \frac{K}{4\pi r D} E^{-p} f_p(u, v), \tag{2.3}$$

where

$$u = \frac{r^2 QE}{4D}$$

and

$$f_p(u, v) = \frac{1}{\sqrt{\pi}} \int_v^\infty \left(1 - \frac{u}{x}\right)^{p-2} \frac{e^{-x}}{\sqrt{x}} dx.$$

The lower limit v of the integral $f_p(u, v)$ is

$$v = \begin{cases} \frac{r^2}{4Dt} & \text{if } t < \frac{1}{QE} \\ \frac{r^2 QE}{4D} & \text{if } t > \frac{1}{QE} \end{cases}$$

if there is no upper limit for the injection particle energy. Here t is the age of the nebula.

In order to simplify the calculation of the emission, we further assume that all the radiated power W of an electron of energy E goes into radiation of a frequency ν

corresponding to the maximum synchrotron radiation power. Therefore

$$W(\nu) = C(B_{\perp}\nu)^{1/2}N[E(\nu)], \tag{2.4}$$

where C is a constant, and

$$E(\nu) = \left(\frac{4\pi m_e^3 c^5}{0.29 \times 3e}\right)^{1/2} \left(\frac{\nu}{B\sin\theta}\right)^{1/2}, \tag{2.5}$$

where m_e and e are the mass and charge of an electron, and θ is the particle pitch angle. Here we assume $B\sin\theta = B_{\perp} = (2/3)^{1/2}B$, yielding $E(\nu) = 7.42\times10^{-10}(\nu/B_{\perp})^{1/2}$ erg. The spectral index distribution $S(r)$ between frequency ν_1 and ν_2 is given by

$$S(r) = \frac{\log[W_{\nu 1}(r)/W_{\nu 2}(r)]}{\log(\nu_1/\nu_2)} = \frac{\log(\nu_1/\nu_2)^{1/2} + \log[N_{tot}(\nu_1, r)/N_{tot}(\nu_2, r)]}{\log(\nu_1/\nu_2)}, \tag{2.6}$$

where $N_{tot}(\nu, r)$ is the total number of particles emitted per unit area per unit time, per unit frequency with frequency ν and at radius r from a central point source after integration along the line of sight. Gratton (1972) assumed a point source which makes $r = 0$ a singularity in $N_{tot}(\nu, r)$. We performed integrations along the line of sight starting at a cutoff radius, but this did not affect the larger scale results.

There is a critical energy for synchrotron cooling, $E_{crit} = 1/Qt$, which is relevant for the number density distribution $N(E, r, t)$. If $E > E_{crit}$, $N(E, r, t)$ reaches a steady state solution $N(E, r)$. If $E < E_{crit}$, only particles with $E_{initial} < E/(1-QEt)$ contribute to the spectrum at the frequency ν and $N(E, r, t)$ evolves with time. The corresponding peak synchrotron radiation frequency of particle with E_{crit} is

$$\nu_{crit} = 6 \times 10^{14} \left(\frac{10^3\ yr}{t}\right)^2 \left(\frac{100\ \mu\mathrm{G}}{B}\right)^3\ Hz. \tag{2.7}$$

If the injected particles have an upper limit of energy E^*, the lower limit v of the integral $f_p(u, v)$ changes to

$$v = \begin{cases} \frac{r^2}{4Dt} & \text{if } t < \frac{1}{Q}\left(\frac{1}{E} - \frac{1}{E^*}\right) \\ \frac{r^2 Q}{4D\left(\frac{1}{E} - \frac{1}{E^*}\right)} & \text{if } t > \frac{1}{Q}\left(\frac{1}{E} - \frac{1}{E^*}\right) \end{cases}$$

and the critical energy becomes $E^*/(1 + QtE^*)$. When the energy range of interest satisfies $E \ll E^*$, the E^* term in v is not important and can be neglected, which means we can assume the injection particle energy has no upper limit. A plausible estimate for E^* is that the gyroradius of the particle equals to the termination shock radius, R_s, or $R_s = R_{gyro} = E/eB$ for a relativistic electron. We then have $E^* = R_s eB$ and the corresponding peak synchrotron emission frequency is

$$\nu^* = 3.3 \times 10^{22} \left(\frac{R_s}{0.1\text{pc}}\right)^2 \left(\frac{B}{100\mu\text{G}}\right)^3 \; Hz.$$

For the objects considered in this paper, electron energy injection with no upper limit is always a good assumption for frequencies below soft X-rays.

The spectral index distribution of the system at a certain frequency band mainly depends on the ratio η between diffusion distance $d = (6Dt)^{1/2}$ and the nebular size R. At a certain frequency, the same $\eta = d/R = (6Dt/R^2)^{1/2}$ gives roughly the same spectral index distribution. The p index of the injected particles would also affect the spectral index profile to some extent. Since we have good observational data for the spectral index of the PWNe considered here, its value can be directly determined from the observations. If the frequency band is in the steady state regime, then $t = 1/QE$, and we find $\eta \propto (D/\nu^{1/2}B^{3/2}R^2)^{1/2}$. Since the nebular size is usually known, the spectral index distribution is determined by $\eta \propto (D/B^{3/2})^{1/2}$ in a particular frequency band. The diffusion coefficient D and magnetic field B are coupled together in the spectral index fitting; in order to get an accurate diffusion coefficient D, we need to know the magnetic field B of the system. One way to estimate B is based on the synchrotron break frequency in the integrated spectrum (equation [2.7]). However, the break is not a sharp feature and it is difficult to locate the synchrotron break frequency of the Crab and 3C 58 based on current observational data (Slane et al. 2008; Arendt et al. 2011). Another way is to model the high energy inverse Compton emission. The magnetic field obtained by using inverse Compton fitting is slightly different from the magnetic field defined in our pure diffusion model, because in our model we solve for the constant B situation which means the magnetic field B is an average B of the PWN over its lifetime. Our average magnetic field should be slightly larger than the magnetic field indicated by inverse Compton modeling. The minimum energy method for synchrotron emission also gives an estimate for B, but it depends on an uncertain assumption. If the frequency band is in the non-steady state regime, $\eta = d/R = (6Dt/R^2)^{1/2}$, where t is now the age of the nebula. The diffusion coefficient D and magnetic field B are now decoupled and $\eta \propto (D)^{1/2}$. However, in this regime the particles do not suffer synchrotron losses, so their spectrum is not changed from the injection spectrum and they do not give useful information about the diffusion coefficient.

Next we consider how the spectral index profile varies as a function of the ratio η. As we are mainly interested in the steady state case, we now consider the critical frequency ν_R corresponding to the case $\eta \approx (4Dt)^{1/2}/R = (4D/QER^2)^{1/2} = 1$. It is the same as ν_B defined in Gratton (1972):

$$\nu_R = 1 \times 10^{17} \left(\frac{D}{10^{27}\ cm^2\ s^{-1}} \right)^2 \left(\frac{1\ pc}{R} \right)^4 \left(\frac{100\ \mu\mathrm{G}}{B} \right)^3\ Hz. \tag{2.8}$$

We assume a PWN in steady state with $p = 2.5$, and scale to a nebular size $R = 1$ pc, magnetic field $B = 100$ μG and diffusion coefficient $D = 10^{27}$ cm^2 s^{-1}. We calculate the spectral index distribution for the three cases: $\nu \ll \nu_R, \nu \approx \nu_R$, and $\nu \gg \nu_R$ (Figure 2.1). When $\nu \ll \nu_R$, which corresponds to $\eta \gg 1$, the photon index profile is flat. At high frequency the photon index profile first changes into a power law when $\nu \approx \nu_R, \eta \approx 1$, and then into an exponential when $\nu \gg \nu_R, \eta \ll 1$. When the diffusion distance $d \gg R$, the diffusing particles within the nebula are well mixed so the spectral index profile tends to be flat. When the diffusion distance $d < R$, the particle density drops quickly along the radial direction because of the short cooling time, so the spectral index shows steepening in the radial direction.

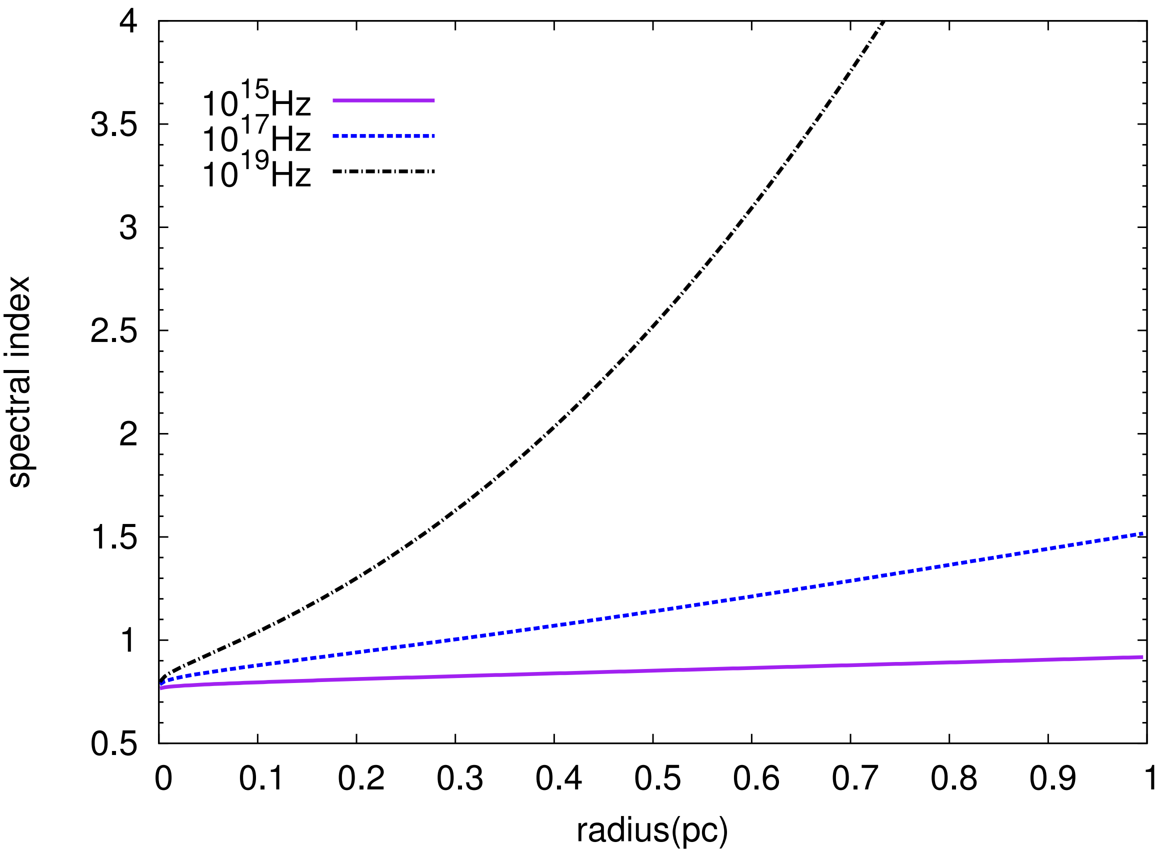

Fig. 2.1.— Flux spectral index (β) distribution of a PWN with $p = 2.5$, nebular radius $R = 1$ pc, $B = 100$ μG, and $D = 10^{27}$ cm^2 s^{-1} in a pure diffusion model.

A calculation of the spectral index distribution in the KC model shows that it has a problem in explaining the observed spectral index profile (see also Reynolds 2003). We take the Crab as an example and use the KC model to calculate the spectral index distribution of the Crab at optical wavelengths, where the KC model is still applicable. We use the best fit parameters given by Kennel & Coroniti (1984b) to do the calculation and assume that there is no synchrotron emission within the termination shock. In order to give a good comparison, we use the same emissivity as used in Kennel & Coroniti (1984b), which is slighty different from our value. We add a pre-defined radius R which is 20 times of the termination shock radius in the simulation; there is no emission beyond this point. The results are shown in Figure 2.2. The spectral index profile in Figure 2.2 does not fit the optical data shown in Veron-Cetty & Woltjer (1993). In the observations, the spectral index profile is approximately a power law distribution, while the results given by the KC model are flat within a certain radius and then increase very quickly beyond that radius. The power law like spectral index distributions are also seen at X-ray wavelengths in 3C 58 (Slane et al. 2004) and G21.5–0.9 (Slane et al. 2000; Safi-Harb et al. 2001) which indicates that diffusion processes could be generally important in young PWNe (Reynolds 2003). Del Zanna et al. (2006) show that a 2D MHD simulation could reproduce most of the toroidal and jet like structure near the termination shock, but the spectral index properties of the Crab Nebula suggest diffusion processes on larger scales.

The nebular size of a PWN is also determined by ν_R or η. When $\nu < \nu_R$, $\eta > 1$ in the steady state case, the nebular size remains the same due to the boundary condition. When $\nu > \nu_R$, $\eta < 1$, the size tends to shrink as the cooling time of particles is smaller than the diffusion time. In the $\nu > \nu_R$, $\eta < 1$ regime, the nebular

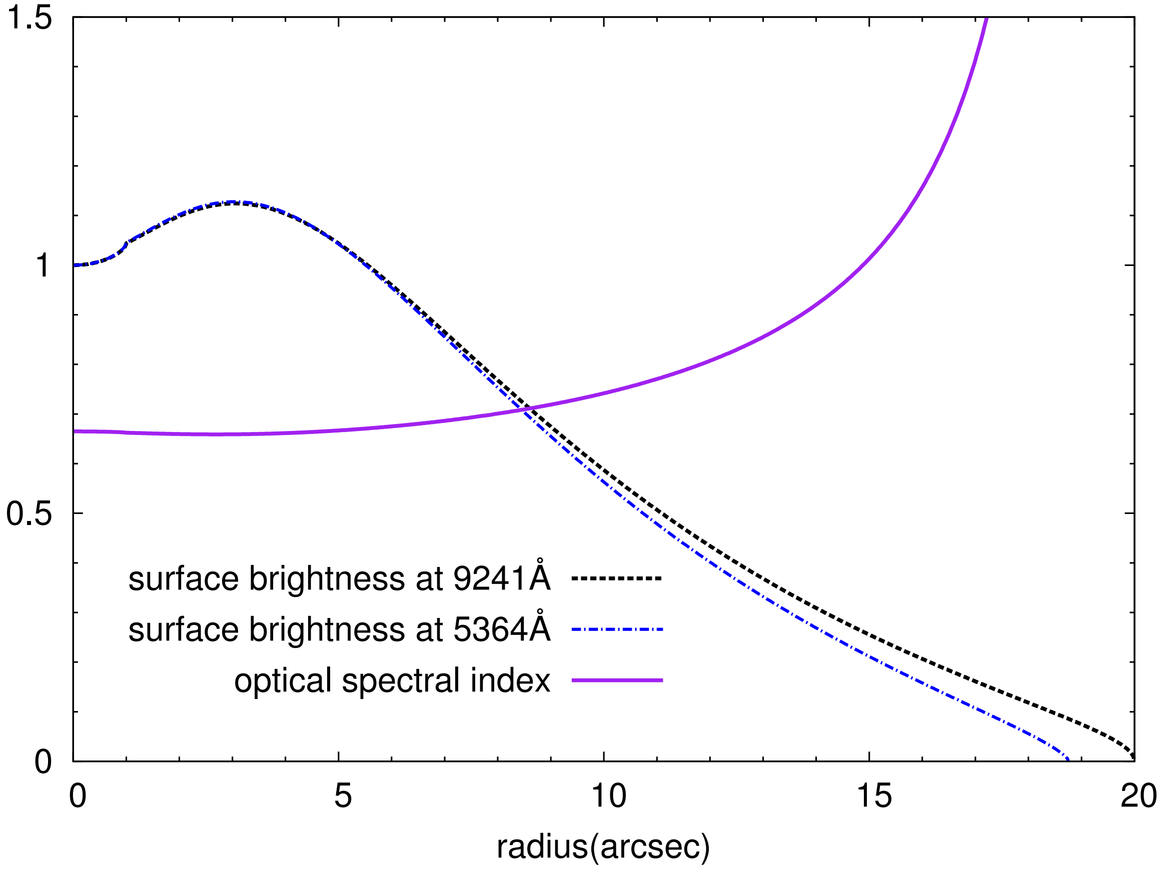

Fig. 2.2.— Flux spectral index (β) distribution of the Crab at optical wavelengths, based on the model of Kennel & Coroniti (1984b). The surface brightness is normalized to the value at the center of Crab.

size for the pure diffusion model can be estimated by setting $\eta = 1$, which yields $R \approx (6D/QE)^{1/2}$.

We first use parameters known from observations such as age t, nebular size R and magnetic field B to fit the spectral index distribution of the Crab, 3C 58 and G21.5–0.9. Fitting a model yields the diffusion coefficient D and p of the PWNe. We then discuss the nebular size behavior. For the Crab we use a magnetic field $B = 300$ μG. This is slightly larger than the value, ~ 200 μG, found by de Jager et al. (1996) and Aharonian et al. (2004) from inverse Compton emission, which gives the current value of the field. Our value gives a sufficiently high diffusion coefficient D to explain the size of the Crab. Radio data for the Crab show $p = 1.52$. The spectral index distribution from radio (5 GHz) to optical 6×10^{14} Hz frequencies is shown in Figure 2.3. By comparing our results with the major axis data in Wilson (1972) we find that $D = 2.5 \times 10^{26}$ cm^2 s^{-1} gives a good fit to the data. Since we do not know exactly the optical frequency used in Wilson (1972), we did not do a least squares fit. We then used the diffusion coefficient $D = 2.5 \times 10^{26}$ cm^2 s^{-1} to calculate the spectral index distribution for infrared ($3.6 - 4.5$ μm) and optical ($5364 - 9241$ Å) wavelengths, which are shown in Figures 2.4. In the infrared (IR), fitting the spectral index variation from 0.3 to 0.8 within the Crab nebula found by Temim et al. (2006) requires the nebular radius to be $\sim 130''$. Our simulation indicates that in the IR the nebular size of the Crab has decreased due to synchrotron losses, which is consistent with Figure 3 of Temim et al. (2006). The spectral index variation from 0.6 to 1.1 within the Crab Nebula at optical wavelengths (Veron-Cetty & Woltjer 1993) implies the nebular size of the Crab is $\sim 100''$, which is consistent with the results in Figure 2 of Amato et al. (2000). Comparing our simulation results in Figures 2.3 and 2.4 with the data in Wilson (1972) and Veron-Cetty & Woltjer (1993) shows that our spectral index in the central region is lower than the observed value if the optical band is involved. We attribute the discrepancy to an intrinsic break in the injected particle spectrum, which is discussed below. The main uncertainty in the model comes from the magnetic field B, although other factors, such as non-spherical symmetry and boundary conditions, also have some effect.

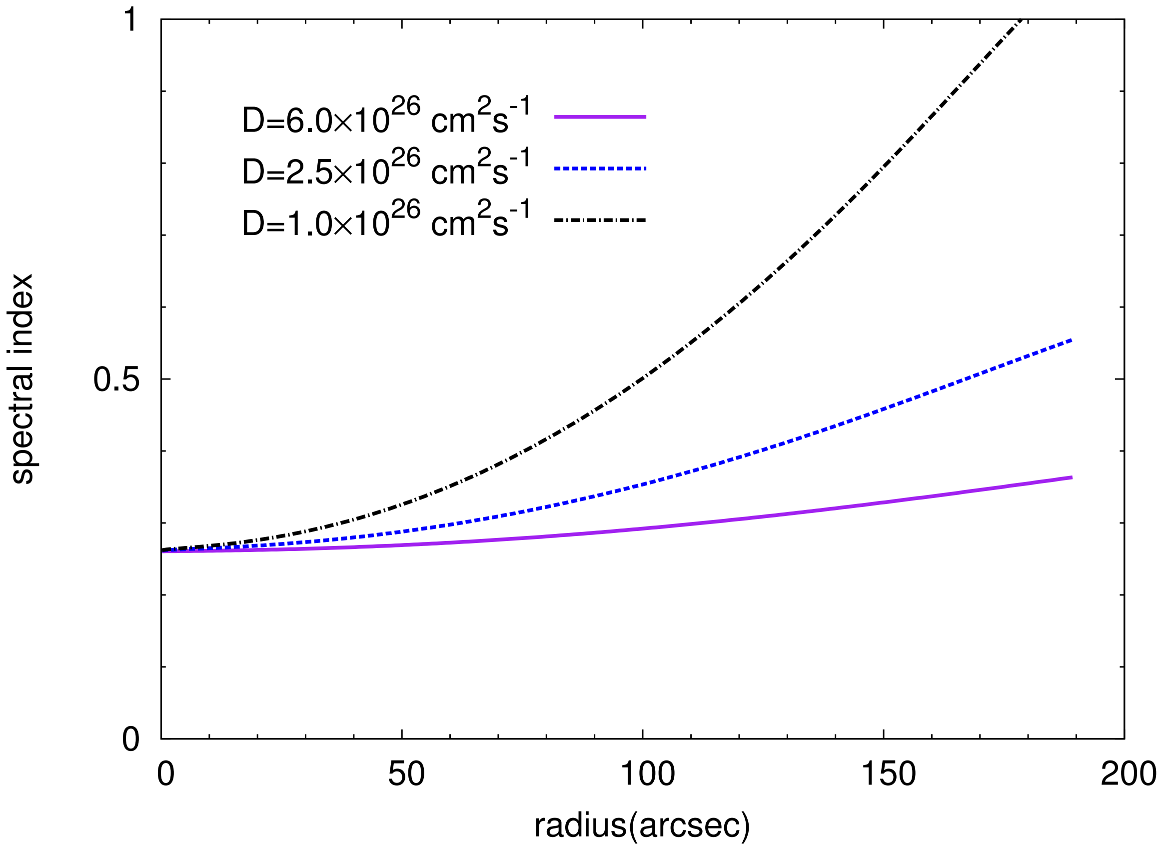

Fig. 2.3.— Flux spectral index (β) distribution of the Crab from 5 GHz to 6×10^{14} Hz, assuming $p = 1.52$ and $B = 300$ μG in a pure diffusion model.

We used the same formalism to fit the X-ray photon index profiles of 3C 58 and G21.5–0.9. According to equation (2.7), the X-ray emitting particles of both 3C 58 and G21.5–0.9 have reached a steady state if they are young PWNe, so their age information is not required for photon index fitting and we can use the steady state solution to calculate the photon index distribution. The parameters we used for 3C

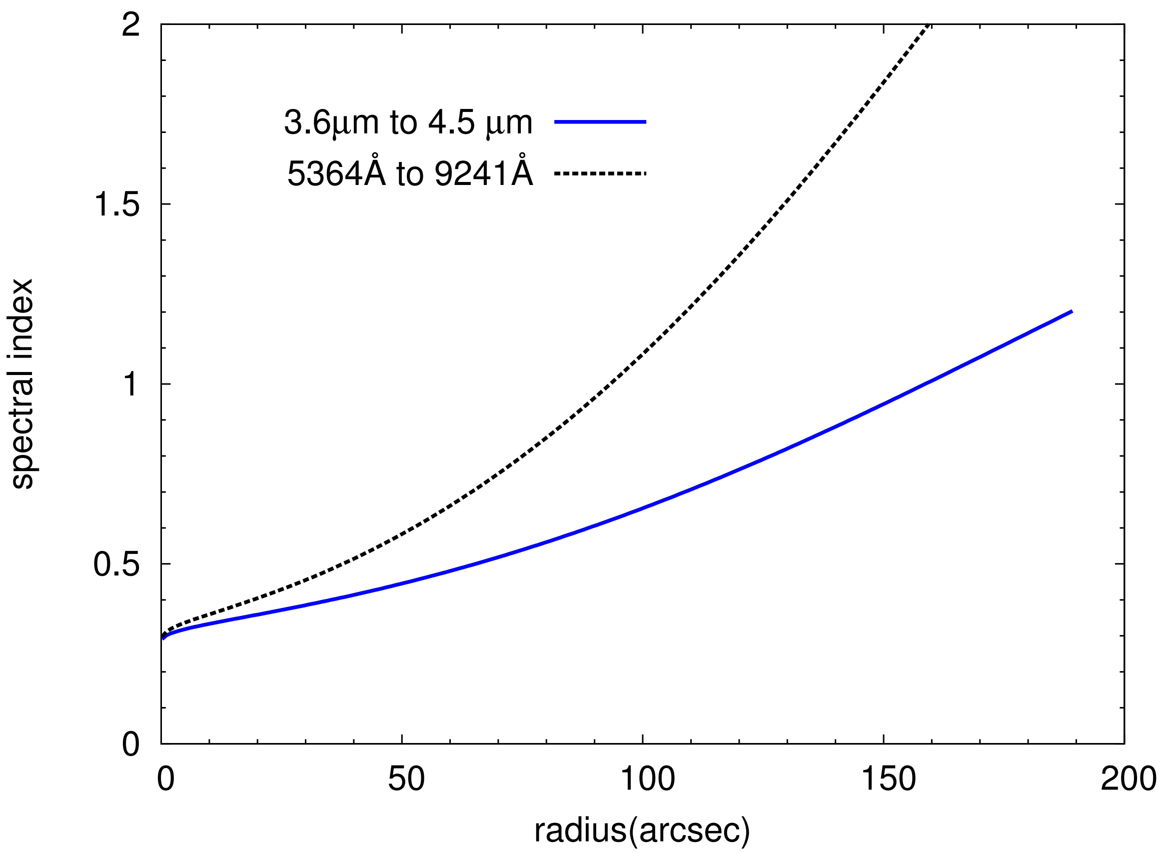

Fig. 2.4.— Flux spectral index (β) distribution of the Crab at IR and optical wavelengths, assuming $p = 1.52$, $B = 300$ μG, and $D = 2.5 \times 10^{26}$ cm^2 s^{-1} in a pure diffusion model,

58 and G21.5–0.9 are listed in Table 2.1. For 3C 58, the magnetic field $B = 80\ \mu$G is based on the minimum energy condition (Green & Scheuer 1992). For G21.5–0.9, the magnetic field $B = 180\ \mu$G is based on the equipartition condition (Safi-Harb et al. 2001). We used a least squares method to fit the photon index data of both 3C 58 (Slane et al. 2004) and G21.5–0.9 (Slane et al. 2000). The 2 parameters in each fit are the injected particle spectral index p and diffusion coefficient D. The best fit for 3C 58 between 2.2 keV and 8 keV with $\chi^2_{red} = 0.83$ gives $p = 2.93$ and $D = 6.1 \times 10^{27}$ cm^2 s^{-1} (Figure 2.5). For G21.5–0.9, the best fit between 0.5 keV and 10 keV with $\chi^2_{red} = 3.28$ gives $p = 2.08$ and $D = 3.7 \times 10^{27}$ cm^2 s^{-1} (Figure 2.6). The diffusion coefficients D we obtained for 3C 58 and G21.5–0.9 are higher than for the Crab. Part of the reason may be uncertainties in the magnetic field B of 3C 58 and G21.5–0.9. As discussed above, the diffusion coefficient D and magnetic field B follow $D \propto B^{3/2}$. If the magnetic field B is lower than our estimate, the diffusion coefficient D also drops; this would imply a high particle energy in the nebulae because we used the minimum energy value of B. We found that the value of p is insensitive to B and D.

Table 2.1: Parameters used for modeling photon index profile

Object	Frequency band	Magnetic field B (μG)	Distance (kpc)	Angular size of PWN (arcsec)	Age (yr)
Crab	$5 \times 10^9 - 6 \times 10^{14}$ Hz	300	2.0	190	957
Crab	$3.6 - 4.5\ \mu$m	300	2.0	190	957
Crab	$5364 - 9241$ Å	300	2.0	190	957
3C 58	$2.2 - 8$ keV	80	3.2	100	
G21.5-0.9	$0.5 - 10$ keV	180	5.0	40	

By using equation (2.8), we obtain $\nu_R = 2 \times 10^{13}$ Hz for the Crab if $D = 2.5 \times 10^{26}$ cm^2 s^{-1} and $B = 300\ \mu$G; $\nu_R = 1.3 \times 10^{18}$ Hz for 3C 58 if $D = 6.1 \times 10^{27}$ cm^2 s^{-1} and $B = 80\ \mu$G; $\nu_R = 2.6 \times 10^{17}$ Hz for G21.5–0.9 if $D = 3.7 \times 10^{27}$ cm^2 s^{-1}

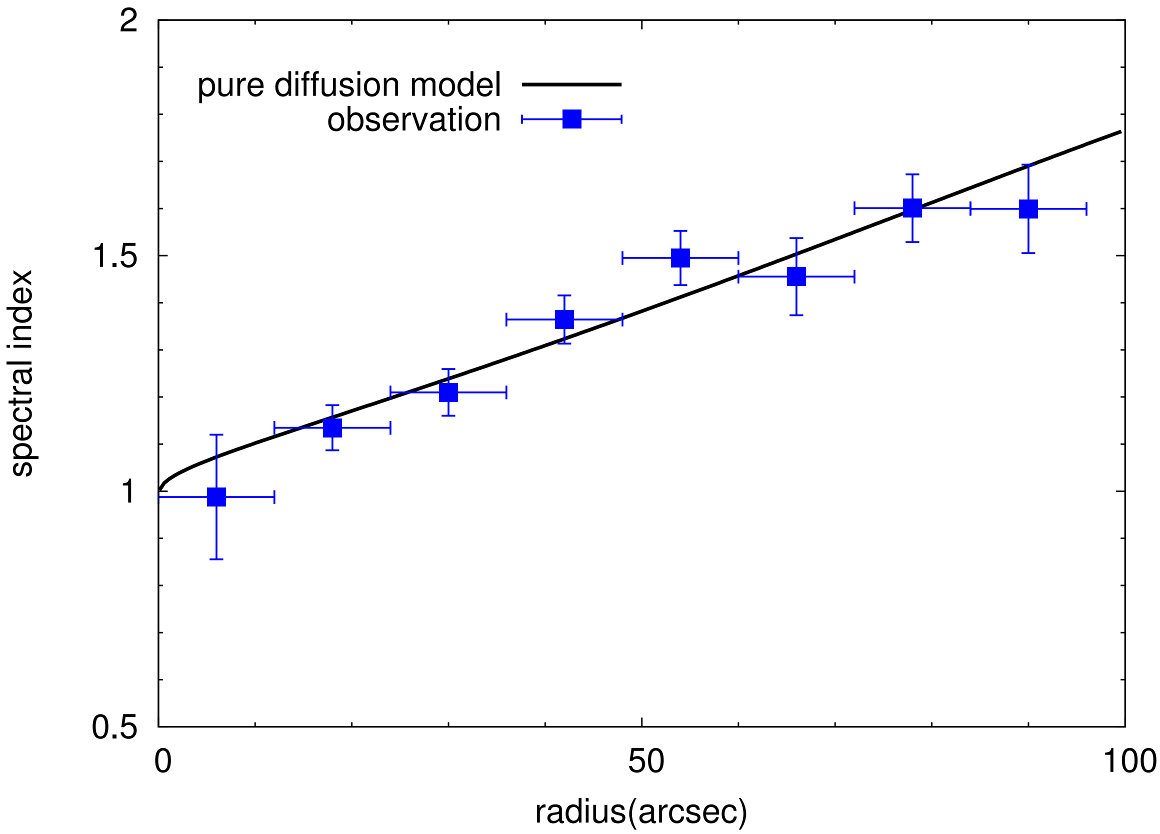

Fig. 2.5.— Flux spectral index (β) distribution of 3C 58 from 2.2 keV to 8 keV, assuming $p = 2.93$, $B = 80$ μG and $D = 6.11 \times 10^{27}$ cm^2 s^{-1} in a pure diffusion model.

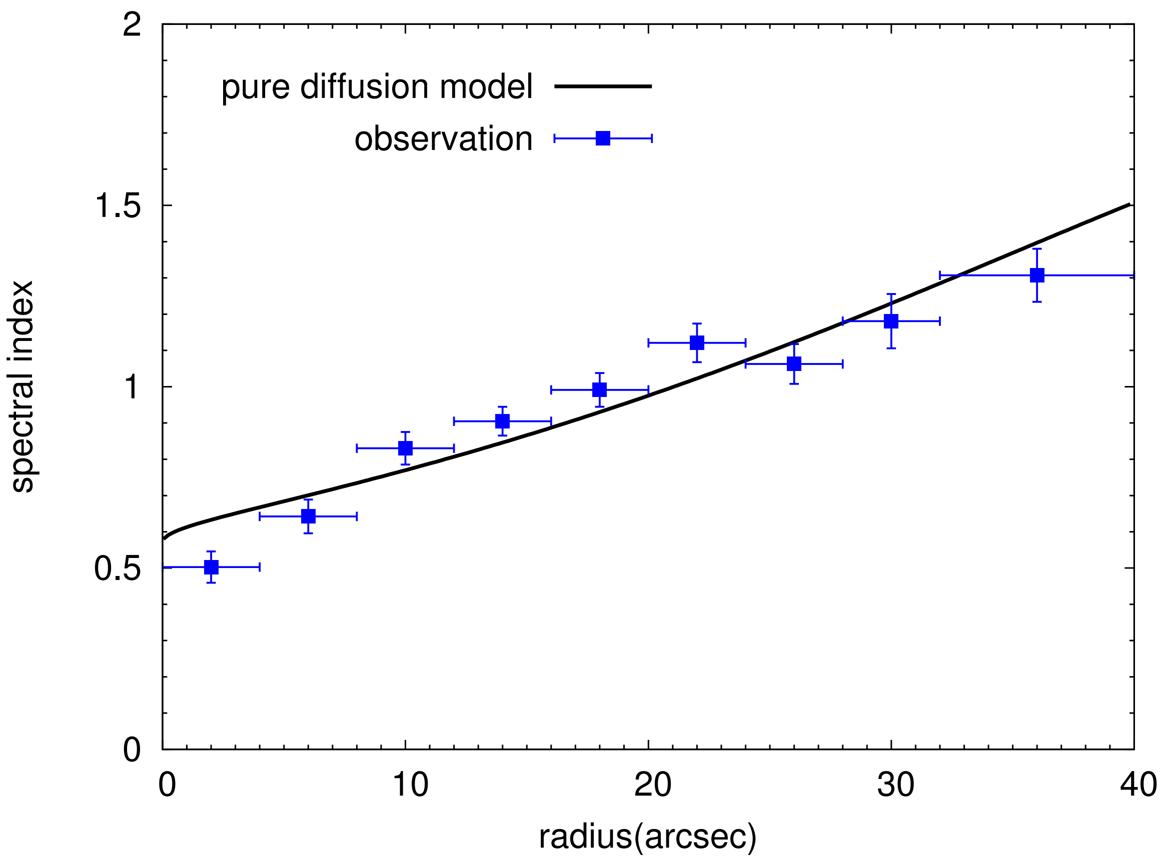

Fig. 2.6.— Flux spectral index (β) distribution of G21.5-0.9 from 0.5 keV to 10 keV assuming $p = 2.08$, $B = 180\ \mu$G and $D = 3.66 \times 10^{27}$ cm^2 s^{-1} in a pure diffusion model.

and $B = 180$ μG. For the Crab, X-ray, optical and near-IR frequencies are all in the $\nu > \nu_R$ regime, so the nebular size decreases from radio to X-ray. For 3C 58 and G21.5–0.9, all frequencies below soft X-rays are in the $\nu < \nu_R$ regime, so the radio, optical and soft X-ray nebular sizes of 3C 58 and G21.5–0.9 tend to be similar. The different behavior of nebular size as a function of frequency among the Crab, 3C 58 and G21.5–0.9 is due to the fact that the Crab has a larger magnetic field but lower diffusion coefficient. We use our pure diffusion model to calculate the half light radius of the Crab Nebula with $p = 1.52$, $B = 300$ μG and $D = 2.5 \times 10^{26}$ cm^2 s^{-1} (Figure 2.7), assuming that there is an upper limit to the injected particle energy E which corresponds to a frequency of 5×10^{22} Hz. There is a bump in the half light radius plot, mainly because for the Crab $p = 1.52$, which is < 2 (Pacholczyk 1970), and we are assuming synchrotron radiation only emits at the peak frequency. If we consider the full synchrotron spectrum, the bump is diminished. Comparing our results to Figure 2 in Amato et al. (2000) shows that our model prediction gives half light radii near the lower limit of radio and optical data for the Crab. At X-ray wavelengths, our theoretical half light radius is much smaller than the observed value. There are several reasons for this. First, the spherical symmetry assumption breaks down at X-ray wavelengths for the Crab. The *Chandra* image of the Crab shows clear toroidal structure near the termination shock (Hester 2008). Second, in our model we assume a point source while it is in fact an extended source. The termination shock has an angular size $\sim 10''$ (0.1 pc) at the Crab Nebula. At radio and optical wavelengths, the nebular size is much larger than the size of the injection region so the point source assumption is adequate, but at X-ray wavelengths it is no longer true. The last reason is that our pure diffusion model does not include the effect of advection. It is likely that both advection and diffusion play a role in PWNe. Assuming $V_{adv} \propto r^{-2}$

near the pulsar wind termination shock (KC), $t_{adv}/t_{diff} \propto R$, so advection becomes more important in the inner regions. We expect advection to play some role in X-ray emission from the Crab, and we discuss it in Section 3.2.

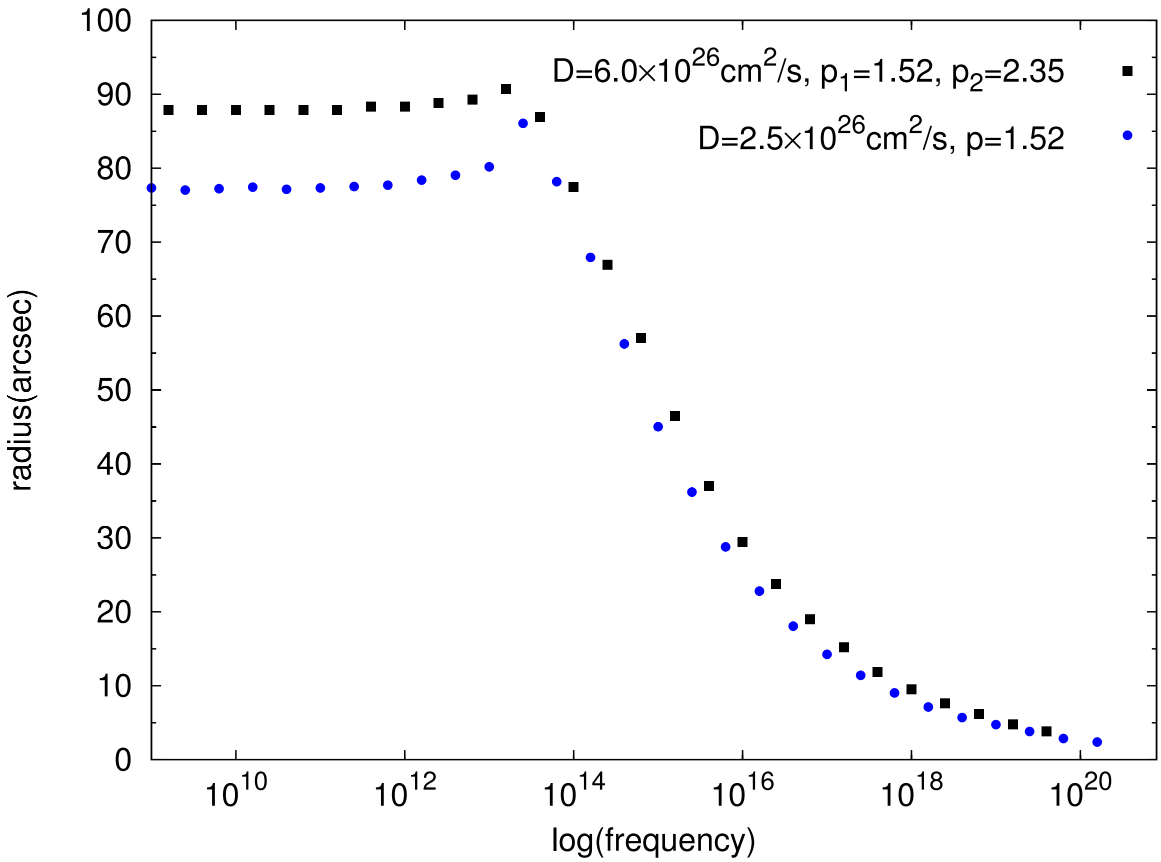

Fig. 2.7.— Crab Nebula half-light radius based on a pure diffusion model with $B = 300\ \mu$G.

In considering the integrated number density $N(E,t)$, we note the result for synchrotron losses only (Pacholczyk 1970)

$$N(E,t) = \frac{K}{(p-1)Q} E^{-(p+1)}[1-(1-QEt)^{p-1}], \qquad \text{if } QEt \leq 1 \tag{2.9}$$

$$= \frac{K}{(p-1)Q} E^{-(p+1)}, \qquad \text{if } QEt > 1. \tag{2.10}$$

Our pure diffusion model deviates from this result because we have a pre-defined

PWN radius R and assume a transparent outer boundary at R; particles that diffuse out of R are not taken into account in the integrated number density $N(E,t)$. The results shown in equation (2.10) would apply to a pure diffusion model with a constant magnetic field B and a reflecting outer boundary which counts all the injection particles. As discussed in Section 2, the issue of transmission through the outer boundary of a PWN is uncertain from the observational point of view. We discuss the spectral index distribution and half light radius of a model with a reflecting outer boundary in Section 3.2.

The Crab, 3C 58 and G21.5–0.9 show flat radio spectra and cannot be fitted by a single power law injection spectrum at radio through X-ray wavelengths even taking into account the evolution of the PWN (e.g., Reynolds & Chevalier 1984). Bucciantini et al. (2011) considered a 1 zone model with a broken power law injection spectrum and long term evolution of the PWN, showing that it can explain the integrated spectra of the Crab and 3C 58 from radio to X-rays. The intrinsic spectral breaks for all PWNe considered are at a similar energy. Sironi & Spitkovsky (2011) did both 2D and 3D particle in cell simulation for the termination shock and show that it could create both a flat power law ($p \sim 1.5$) and steep power law ($p \sim 2.5$) components in the post-shock spectrum. The spectral break of PWNe between radio and optical wavelengths may be a natural consequence of particle acceleration at the termination shock. In fitting the optical spectral index distribution for the Crab, we already mentioned that there are indications of another power law component in the Crab. Here we use a double power law injection spectrum in our pure diffusion model and re-calculate the spectral index distribution and half light radius of the Crab. The evolution of the PWN is still ignored here because of the additional complications. For 3C 58 and G21.5–0.9, the X-ray spectral index data are well above the spectral break frequency and our modeling is not affected by the double power law feature. We continue using a magnetic field $B = 300\ \mu$G and $p_1 = 1.5$ for the low energy component of Crab particle distribution. We use $p_2 = 2.35$ and a break energy 4×10^{11} eV for the other power law component as found by Bucciantini et al. (2011) and find that $D = 6.0 \times 10^{26}$ cm^2 s^{-1} gives a good fit to the major axis data in Wilson (1972), as shown in Figure 2.8. Then we use the same diffusion coefficient D to calculate the spectral index distribution at IR and optical wavelengths (Figure 2.8). After adding another power law component, we obtain a better fit to the central spectral index data in Wilson (1972) and Veron-Cetty & Woltjer (1993). The nebular radius we need to explain the spectral index variation at IR (Temim et al. 2006) and optical (Veron-Cetty & Woltjer 1993) wavelengths becomes smaller: $\sim 110''$ in IR and $\sim 70''$ in optical wavelengths. Our simulation gives a spectral index of 0.7 at the center of the Crab at optical wavelengths, which is slightly larger than the observed value. This is due to the fact that we use $p_2 = 2.35$ (Bucciantini et al. 2011) for the steep power law. However, the best fit parameter Bucciantini et al. (2011) obtained in their 1D evolution model may not be the best fit parameter for our case as we are considering a steady-state situation. If we change the break energy for the two power laws, we could obtain a better fit to the optical nebular radius, but the improvement is not significant in view of the other uncertainties in the model. The half light radius of the Crab with double power law injection spectrum is shown in Figure 2.7. The double power law fit gives a larger nebular size in the radio band which is in the non-steady state regime, mainly because we use a larger diffusion coefficient D in the double power law fit.

So far, the results are under the assumption that all the emission of an electron goes into radiation at a frequency ν corresponding to the maximum synchrotron radi-

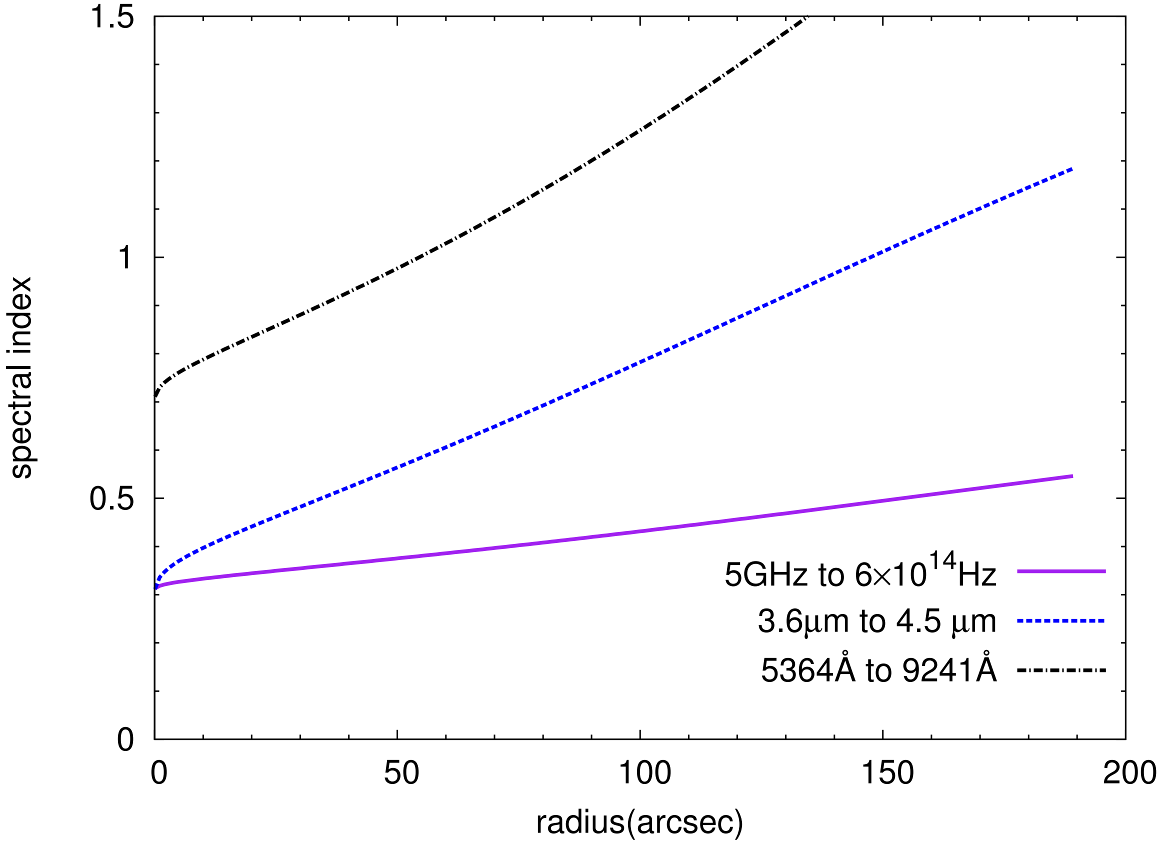

Fig. 2.8.— Flux spectral index (β) distribution of the Crab for different wavelength bands assuming $p_1 = 1.52$, $p_2 = 2.35$, $B = 300\ \mu$G, and $D = 6.0 \times 10^{26}$ cm^2 s^{-1} in a pure diffusion model.

ation power. We will continue to make this assumption in the next section because it speeds the calculations, but here we carry out the calculation with a full synchrotron spectrum to show the uncertainty caused by our approximation. We considered the Crab, 3C 58 and G21.5–0.9, and our numerical results with the full synchrotron spectrum (Figure 2.9) show that the diffusion coefficient D required to fit the observations drops by a factor about 2. Here, we integrate the synchrotron radiation function $F(x = \nu/\nu_c)$ (Pacholczyk 1970) from 0.005 to 500 and assume that for 3C 58 and G21.5–0.9 all the particles within that energy range are in a steady state. Because $F(x = \nu/\nu_c)$ drops very quickly beyond the peak and we are calculating the spectral index distribution of 3C 58 and G21.5–0.9 in X-rays, time dependent effects are expected to be small.

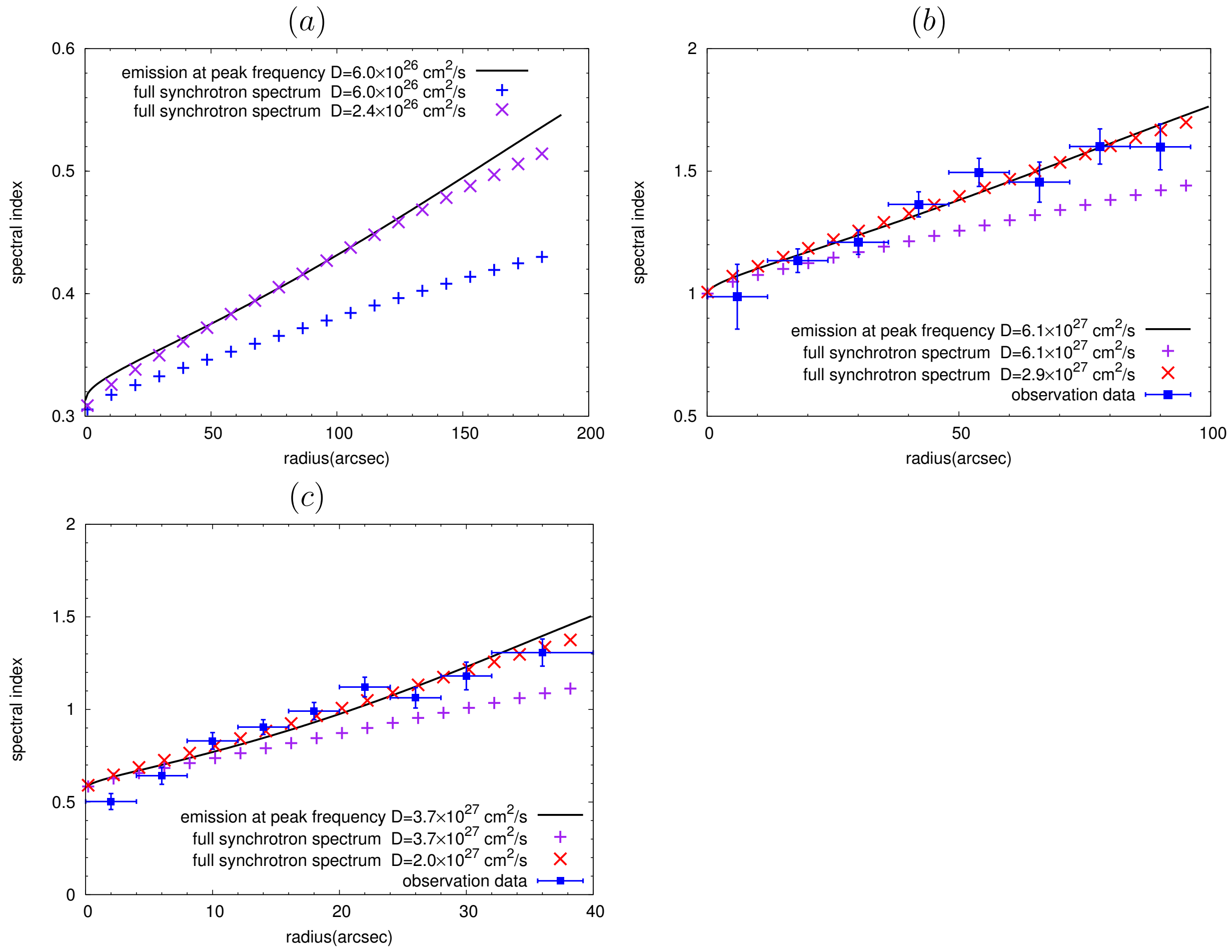

Fig. 2.9.— (a) Flux spectral index (β) distribution of Crab from 5 GHz to 6×10^{14} Hz assuming $p_1 = 1.52$, $p_2 = 2.35$ and $B = 300\ \mu$G, (b) Flux spectral index (β) distribution of 3C 58 from 2.2 keV to 8 keV assuming $p = 2.93$ and $B = 80\ \mu$G, (c) Flux spectral index (β) distribution of G21.5–0.9 from 0.5 keV to 10 keV assuming $p = 2.08$ and $B = 180\ \mu$G.

In the pure diffusion model we have assumed that the diffusion coefficient is constant. However, it is possible that the diffusion coefficient in the PWN has energy dependence $D_E(E)$, as discussed in Section 2, and we now investigate how the energy dependence of the diffusion coefficient would affect our pure diffusion model. We use the Green's function method to solve the steady state equation of the pure diffusion model but now with an energy dependent diffusion coefficient $D_E(E) = D_0 E^\sigma$:

$$D_0 E^\sigma \nabla^2 N + Q \frac{\partial E^2 N}{\partial E} = -K E^{-p} \delta(\vec{r}). \tag{2.11}$$

The resulting particle distribution function is (see Appendix)

$$N(E,r) = \frac{K}{4\pi r D_0 E^\sigma} E^{-p} \frac{1}{\sqrt{\pi}} \int_u^\infty \left(1 - \frac{u}{x}\right)^{\frac{p+\sigma-2}{1-\sigma}} \frac{e^{-x}}{\sqrt{x}} dx, \tag{2.12}$$

where

$$u = \frac{r^2 Q E (1-\sigma)}{4 D_0 E^\sigma}.$$

In the solution, u changes to $u = r^2 QE(1-\sigma)/4D_0E^\sigma$; again, $\sqrt{u}$ can be considered as a ratio of the diffusion distance to the nebular radius. In a steady state, $t = 1/QE$, and we have $\sqrt{u} = r(1-\sigma)^{1/2}/(4D_0E^\sigma t)^{1/2}$. Setting $u = 1$, we find that the nebular size $R \propto E^{-(1-\sigma)/2} \propto \nu^{-(1-\sigma)/4}$. For the spectral index distribution, we note that $\sigma > 0$ implies that more energetic particles diffuse out more rapidly than less energetic particles, which should flatten the spectral index distribution; the same effect results from reducing the magnitude of the diffusion coefficient when $\sigma = 0$. Our simulations show that the case $D_E = D_0 E^\sigma$ corresponds to a constant diffusion coefficient case with D if $D_E = (1-\sigma)^2 D$. The flux spectral index at the center now is $(p_E + \sigma - 1)/2$ (equation [2.12]) because the integral part in the solution approaches some constant when $r \to 0$. In order to get the same spectral index at the center as in constant diffusion coefficient case we need $p_E = p - \sigma$. In Figure 2.10, we consider a PWN with $p_E = p - \sigma = 2.5 - \sigma$, nebular size $R = 1$ pc, magnetic field $B = 100\ \mu$G, and diffusion coefficient $D_E = 10^{27}(1-\sigma)^2$ cm^2 s^{-1} at an energy corresponding to $\nu = 10^{17}$ Hz, and plot the spectral index profile for different σ values. It is clear that they all have a similar slope, implying that for a certain band, if a pure diffusion model with constant D can fit the data, a pure diffusion model with energy dependent D_E can also fit the data but with different p and diffusion coefficient at that band. Although energy dependence of the diffusion coefficient does not change the consequences of spectral index fitting with constant D at one wavelength band, it changes the fitting result when multiband data are considered because now the nebular size $R \propto \nu^{-(1-\sigma)/4}$ instead of $R \propto \nu^{-1/4}$. We previously found with the constant diffusion coefficient assumption, there was a problem in explaining the nebular size of the Crab beyond optical frequencies. If we take the energy dependence of D_E into account, we can fit the data on nebular size and overall appearance of the spectral index profile in the IR and optical better. However it is difficult to determine whether energy dependence is required by the data. Since other factors like advection affect the nebular size and spectral index profile of the Crab in a similar way, and the observational data for the Crab Nebula do not have high precision, the energy dependence of the diffusion coefficient is not determined by our models. However, the decreasing size at higher photon energies implies that $\sigma < 1$; as discussed in Section 2, some treatments of diffusion in old PWNe have assumed $\sigma = 1$.

2.3.2 Diffusion and advection model

We now use Monte Carlo simulations to consider models with diffusion and advection. Monte Carlo methods allow the treatment of cases that cannot be treated in the pure diffusion, analytical model. We expect that advection plays some role in the spectral index distribution and half light radius, especially in the $\nu \gg \nu_R$ regime. In the MHD model of KC, there is an advective flow after the termination shock in which the flow velocity declines from mildly relativistic to the velocity at the edge

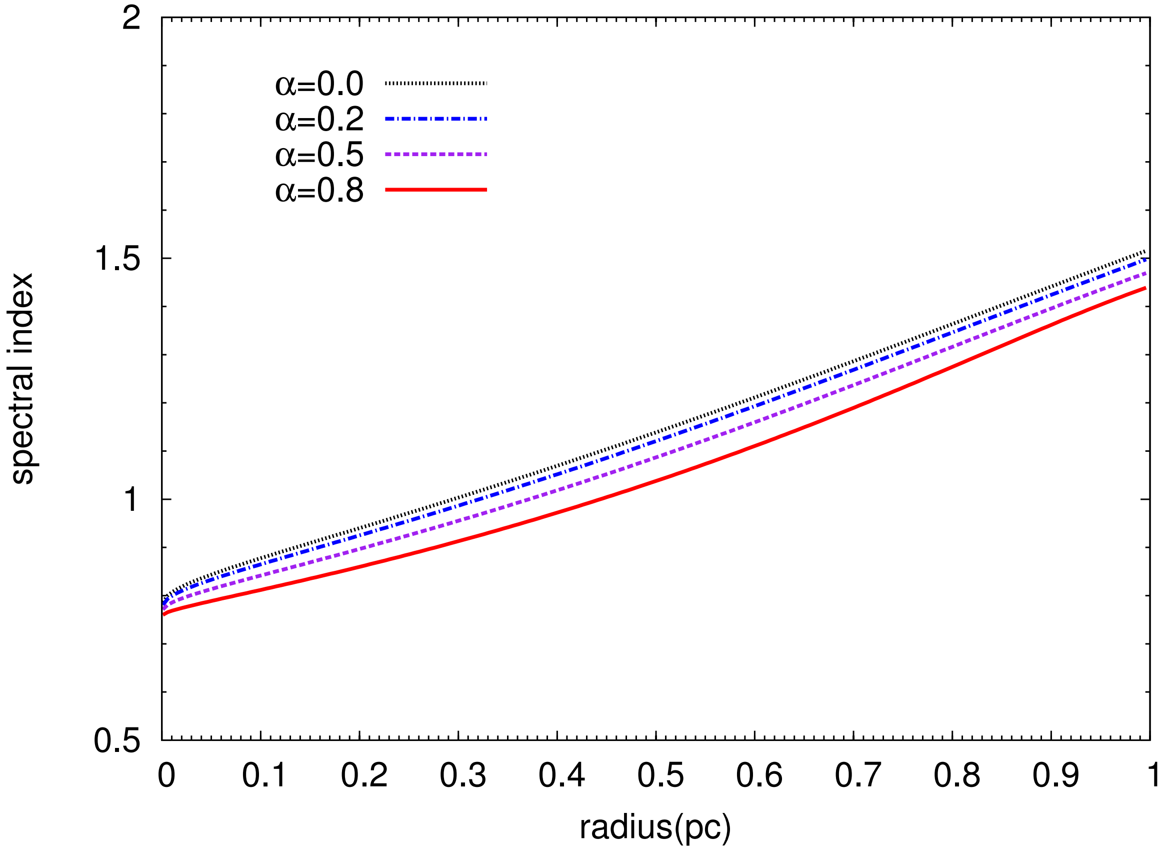

Fig. 2.10.— Flux spectral index (β) distribution of a PWN with $p_E = 2.5 - \sigma$, nebular size $R = 1$ pc, magnetic field $B = 100\ \mu$G, and diffusion coefficient $D_E(\nu = 10^{17}\ Hz) = 10^{27}(1-\sigma)^2$ cm^2 s^{-1}, for various values of σ.

of the nebula, $\sim 2000\,\mathrm{km\,s^{-1}}$. If the magnetic field is not dynamically important, the velocity declines as r^{-2} in a steady flow. Another consideration is a reflecting outer boundary condition. For PWNe satisfying $\eta = (6Dt/R^2)^{1/2} \gg 1$, the reflecting boundary should have a significant effect on the spectral index distribution and half light radius. For the reflecting boundary effect we primarily focus on 3C 58, which has a high diffusion coefficient D. The last improvement is treating an extended source, since the termination shock has a finite size ~ 0.1 pc which can play a role in the central region. The time dependence of the PWN and non-spherical symmetry are not taken into account.

Massaro (1985) discussed a diffusion and advection model, but many assumptions were needed to obtain an analytical model. Weinberg & Silk (1976) and Reynolds & Jones (1991) investigated approximate solutions for a pure diffusion model with an extended source, but they omit some of the physical effects that we wish to include. We therefore developed a code to carry out Monte Carlo simulations that allowed a general treatment of diffusion and advection processes. We modeled both the Crab and 3C 58. For 3C 58 we mainly focus on the variation of spectral index distribution while for the Crab we are interested in the variation of the half light radius with photon energy. In simulating 3C 58, a total number of 10^6 effective particles were injected into a spherical shell at time intervals of 5.4×10^4 s. Since we are considering the X-ray band of 3C 58, which is in a steady state, only particles injected within a time $1/QE$ of the present are taken into account. In simulating the Crab, at least 10^6 effective particles were injected into a spherical shell at time intervals of a half day. The motion of the particles is a superposition of advective motion and 3-dimensional random motion. The displacement in each time interval is

$$\Delta\vec{S}_{tot} = V_{adv}\Delta t\,\vec{r}_o \pm (2D_x\Delta t)^{1/2}\,\vec{x}_o \pm (2D_y\Delta t)^{1/2}\,\vec{y}_o \pm (2D_z\Delta t)^{1/2}\,\vec{z}_o, \tag{2.13}$$

where $\vec{x}_o, \vec{y}_o, \vec{z}_o$ and $\vec{r}_o$ are unit vectors in x, y, z and radial directions. We take $V_{adv} \propto r^{-2}$, $V(r = R_{out}) = 630\,\mathrm{km\,s^{-1}}$(Bietenholz 2006) and the ratio of outer radius to inner radius to be $R_{out}/R_{in} = 100/8 = 12.5$ for 3C 58 (Slane et al. 2004). In this case, we only consider the synchrotron radiation loss since the adiabatic expansion energy loss, $\dot{E} \propto \nabla \cdot V_{adv}$, is zero for our velocity profile. For the Crab, we use some of the parameters from the model of Kennel & Coroniti (1984b), assuming that the velocity at the termination shock is $c/3$, the velocity $V_{adv} \propto r^{-2}$ between the termination shock radius R_s and a critical radius R_c, and V_{adv} remains constant between the critical radius R_c and the outer radius of the nebula R_{out}. We assume $R_s = 15$ arcsec in angular size (Hester et al. 2002), and in order to set $V_{adv}(R_{out}) = 2000$ km s^{-1} (Kennel & Coroniti 1984a) we further assume $R_c = 50^{1/2}R_s$. We consider adiabatic expansion energy losses in addition to synchrotron radiation losses for $R_c < R < R_{out}$; it is $dE/dt = -2V_{adv}(R_{out})E/3r$ for relativistic particles in a medium with constant flow velocity. In all the simulations, we use a constant magnetic field B to simplify the calculation. In spherical symmetry, $D_x = D_y = D_z \equiv D$. If particles move into the inner boundary due to their random motions, they are forced to bounce back into the PWN region. A reflecting boundary was used at the outer radius.

The simulation results for 3C 58 are shown in Figure 2.11. The additional physical processes allow a better fit to the data. In order to discern what role advection and a reflecting boundary play in the photon index distribution, we did one simulation for pure diffusion with only an inner reflecting boundary and one for pure diffusion with both inner and outer reflecting boundaries (Figure 2.11). After comparing the results of the two cases (Figure 2.11), we find that the outer reflecting boundary condition mainly makes the photon index steeper and the part near the outer boundary relatively flat. The diffusion coefficient D required to fit the data becomes higher. Advection is not very important in the fit because the ratio of diffusion time to advection time ratio is low. In the Figures 2.11, we have shown the ratio of diffusion time to advection time t_{diff}/t_{adv}, where t_{diff} is estimated by $(6Dt_{diff})^{1/2} = R_{out} - R_{in}$ and t_{adv} is calculated by $t_{adv} = \int_{R_{in}}^{R_{out}} dr/V_{adv}$. The angular size of the flat region in the radial direction can be estimated as follows. Since $t_{diff} \ll t_{adv}$ in our simulation, advection can be neglected. For particles in a steady state, the diffusion distance is $R_{diff} = (6Dt)^{1/2} = (6D/QE)^{1/2}$, so that $\theta_{flat} \approx \theta \times (R_{diff}/R - 1)$, where θ is the angular size of PWN. Substituting the expression for R_{diff} and recalling that E_R

satisfies $R = (4D/QE_R)^{1/2}$, we obtain

$$\theta_{flat} \approx \theta \left(\left[\frac{3E_R}{2E} \right]^{1/2} - 1 \right) = \theta \left(\frac{6^{1/2}}{2} \left[\frac{\nu_R}{\nu} \right]^{1/4} - 1 \right). \tag{2.14}$$

For 3C 58 with $D = 8.8 \times 10^{27}$ cm^2 s^{-1}, $B = 80$ μG, and $R = 1.55$ pc, equation (2.14) implies $\theta_{flat} \approx 30''$ which is consistent with the results in Figure 2.11. The results shown in Figure 2.11 are calculated for $2.2 - 8$ keV photon energies. When we do the calculation for θ_{flat} we use 8 keV as it gives a lower diffusion distance. We emphasize that equation (2.14) is only correct for a steady state and requires that $1 \gg \frac{\sqrt{6}}{2}(\frac{\nu_R}{\nu})^{\frac{1}{4}} - 1 > 0$. When $\frac{\sqrt{6}}{2}(\frac{\nu_R}{\nu})^{\frac{1}{4}} - 1 < 0$, the cooling time is lower than the diffusion time, and few particles reach the outer boundary. When $\frac{\sqrt{6}}{2}(\frac{\nu_R}{\nu})^{\frac{1}{4}} - 1 > 1$, due to the boundary effect, the diffusion coefficient D is large enough to smear out the spectral index structure in the nebula, so the spectral index distribution is flat within that energy band.

Table 2.2: Half light radius of the Crab Nebula in arcsec

Frequency	10^{15} Hz	10^{16} Hz	10^{17} Hz	10^{18} Hz
pure diffusion	72	43	27	19
diffusion and advection	84	55	35	24

We calculate the spectral index distribution of the Crab at optical wavelengths (Figure 2.12) and its half light radius from ultraviolet (UV) to X-ray frequencies (Table 2.2), which are above the break frequency given by Bucciantini et al. (2011), with $p_2 = 2.0$, $B = 300$ μG and $D = 9.0 \times 10^{26}$ cm^2 s^{-1}. The spectral index variation from 0.6 to 1.1 within the Crab Nebula at optical wavelengths (Veron-Cetty & Woltjer 1993) now implies the nebular size of Crab is $\sim 140''$, which is slightly larger than the pure diffusion case as we now use a larger diffusion coefficient D and take advection into account. The advection process increases the half-light

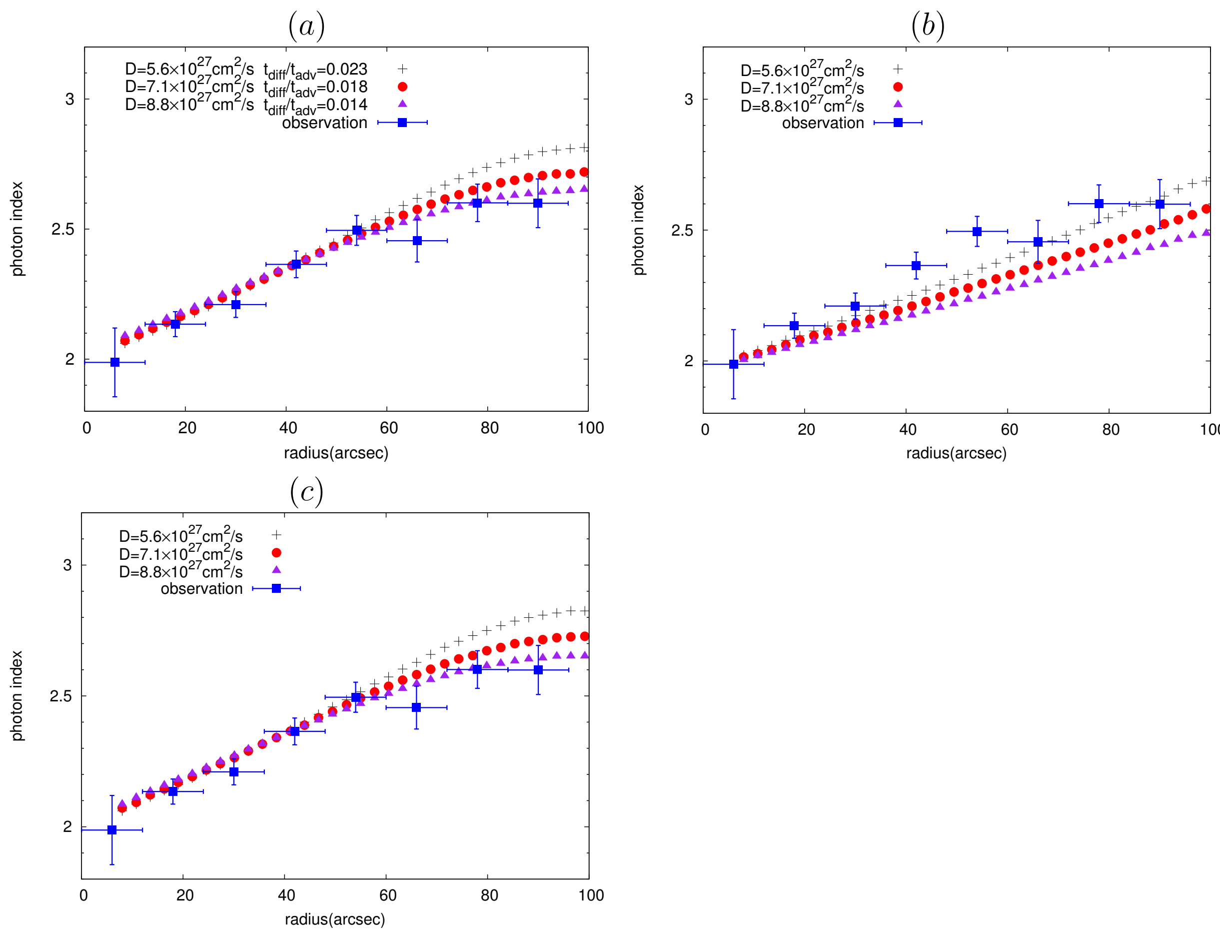

Fig. 2.11.— (a) Monte Carlo simulation with diffusion and advection for 3C 58 from 2.2 keV to 8 keV assuming $p = 2.8$ and $B = 80\mu G$, (b) Monte Carlo simulation with pure diffusion and a reflecting inner boundary, (c) Monte Carlo simulation with pure diffusion and reflecting inner and outer boundaries.

radius of the Crab significantly at X-ray energies. Based on Table 2.2, the ratio $(R_{diff} - R_s)/(R_{diff+adv} - R_s)$ increases rapidly from X-ray to UV wavelengths as we assume the extended source size is $\sim 15''$. The reason advection is important for the Crab in X-rays is because the X-ray size of the Crab is small. As noted in Section 3.1, the ratio of advection time to diffusion time $R_{adv}/R_{diff} \propto R$, the nebular size; advection becomes more important when the nebula is small. The half-light radius derived from the diffusion and advection model can now explain the high frequency part of the Crab nebula size data (Amato et al. 2000). However, the half-light radius we obtained still drops sharply as a function of frequency, which may imply energy dependent diffusion. The values of p_2, magnetic field B, and diffusion coefficient D we choose are not best fit parameters. Certain combinations of parameters would improve the fit to the observational data. The velocity and magnetic field profiles for the diffusion and advection case must be analyzed for more exact models. The uncertainty in the termination shock radius and the flow velocity at the outer radius of the nebula also affect the simulation results.

As discussed in Section 1, 2-dimensional MHD models reproduce many features observed in the inner Crab Nebula. Diffusion is not a factor in this region for 2 reasons: the short advection timescale because of the high flow velocities and a long timescale for radial diffusion because of the toroidal magnetic field. In the Crab, the prominent toroidal structure observed at X-ray and optical wavelengths extends to $\sim 40''$ from the pulsar, while the nebular radius is $200''$. Our model applies to the outer 4/5 of the nebula. Toroidal structure is less prominent in 3C 58 and G21.5–0.9.

We also used Monte Carlo simulations to investigate the case where there is particle transport across the nebular boundary at R and particles are lost from the system once they cross R. The effect is to flatten the spectral index profile in the outer part

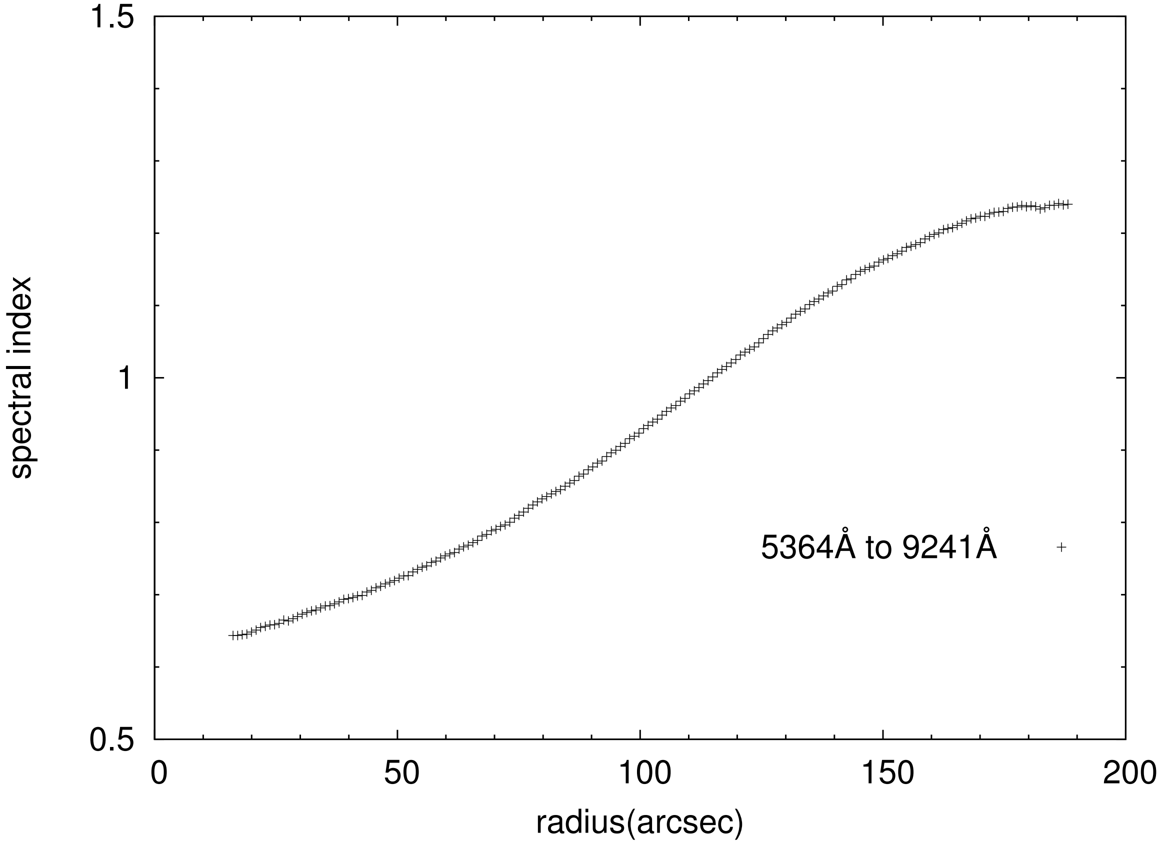

Fig. 2.12.— Flux spectral index (β) distribution of the Crab at optical wavelengths assuming $p = 2.0$, $B = 300\ \mu$G, and $D = 9\times10^{26}$ cm^2 s^{-1} in a Monte Carlo simulation.

of the nebula and to reduce the value of D by a factor of 2 compared to the simple model (Section 3.1). However, we consider the reflecting boundary model to be more plausible, for the reasons given in Section 2.

2.4 Discussion and conclusions

We have argued that the structure of young PWNe is not described by a toroidal magnetic field, as expected in a model like that of Kennel & Coroniti (1984a), but has a more chaotic magnetic structure. In Section 2, we noted various observational studies that showed considerable structure in young nebulae, not a clear toroidal structure. In Section 3, models with diffusion of particles were presented and compared to observations of 3 nebulae. Emphasis was placed on fitting the spectral index profiles of the nebulae, as well as the surface brightness profiles. Models with diffusion were much better able to spectral index profiles than pure advection models. The best estimates of the diffusion coefficient come from the Monte Carlo simulations, but these values need to be somewhat reduced because they do not include the full synchrotron spectrum in the calculation of the emission. Estimates of the diffusion coefficient and the corresponding particle mean free path are given in Table 2.3. The assumed magnetic field is given for each case because $D \propto B^{3/2}$ and the magnetic field strength is uncertain.

Table 2.3: Diffusion coefficient and length

Object	D (cm^2/s)	B (μG)	$\lambda = D/c$ (10^{16} cm)	Particle energy (TeV)
Crab	2.4×10^{26}	300	0.8	0.6
3C 58	2.9×10^{27}	80	10	40
G21.5-0.9	2.0×10^{27}	180	7	30

Table 2.3 shows that the diffusion coefficient and length for the Crab is considerably smaller than that for 3C 58 and G21.5–0.9. The length does not scale with the size of the PWN because the Crab is larger than both 3C 58 and G21.5–0.9. One possibility is that there is frequency dependent diffusion coefficient. The coefficient for the Crab is derived from optical/IR observations, so that the lower energy particles are being observed compared to 3C 58 and G21.5–0.9 where X-ray observations are used. Table 2.3 shows the corresponding particle energies for diffusion coefficients. An energy dependent diffusion with $\sigma \sim 0.5 - 0.6$ would explain the difference between the Crab and the other remnants. As discussed in Section 3.1, this is consistent with our results and we suggest it as a possible explanation for the difference between the PWNe.

The spectral indices along magnetic filaments in the Crab shows relatively little variation while the spectral indices show steepening away from the filament center (Seward et al. 2006; Hester 2008), which is consistent with rapid particle motions along filaments and slow diffusion across filaments. However, the diffusion mean free paths (Table 2.3) are smaller than characteristic structures in the nebulae. The length for the Crab is about a factor 10 smaller than the scale indicated by optical polarization (Section 2), and the length for 3C 58 is about a factor of 10 smaller than the scale of apparent magnetic loops seen in the X-ray image (Slane et al. 2004). The actual longer diffusion time (due to the smaller length) may indicate that the magnetic structure is not completely random.

Our models have been designed for comparison with young PWNe like the Crab, 3C 58, and G21.5–0.9. They are likely to be in an evolutionary phase where the nebulae are accelerating into freely expanding supernova ejecta. In a subsequent phase of evolution, the reverse shock wave from interaction with the interstellar medium comes back toward the center and can push off the PWN, creating an asymmetric nebula (Blondin et al. 2001). Van Etten & Romani (2011) have investigated evolutionary models for the PWN HESS J1825–137, which probably belongs to the class of post-reverse shock nebulae and is observed at X-ray and TeV energies. Of interest is the fact that their modeling shows the need for diffusion of particles. As mentioned in Section 2, Hinton et al. (2011) have considered diffusion from the evolved PWN Vela X. A chaotic magnetic field is expected in these objects because of instabilities related to the interaction with the reverse shock front from the supernova remnants (Blondin et al. 2001). The situation is different for the young remnants discussed here, but a chaotic field may be the result of Rayleigh-Taylor instabilities in the outer parts of the nebulae.

Acknowledgments

This research was supported in part by NASA grant NNX07AG78G and NSF grant AST-0807727.

2.5 Appendix

In order to solve the equation

$$D_0 E^{\sigma} \nabla^2 N + Q \frac{\partial E^2 N}{\partial E} = -K E^{-p} \delta(\vec{r}), \tag{2.15}$$

we first let $\Phi = Q E^2 N$ and $4\pi J = \frac{Q}{D_0} E^{2-\sigma} K E^{-p} \delta(\vec{r})$, so equation (2.15) can be simplified to

$$\nabla^2 \Phi - \frac{Q}{D_0}(1-\sigma) \frac{\partial \Phi}{\partial E^{\sigma-1}} = -4\pi J. \tag{2.16}$$

Further, assuming $m^2 = \frac{Q}{D_0}(1-\sigma)$ and $\tau = E^{\sigma-1}$, we have

$$\nabla^2 \Phi - m^2 \frac{\partial \Phi}{\partial \tau} = -4\pi J. \tag{2.17}$$

Here we only consider the case $m^2 > 0$, which requires $\sigma < 1$, as it is consistent with the situation in the Crab. If $\sigma > 1$, the nebular size of the Crab does not decrease with increasing frequency. Next we consider the Green's function equation corresponding to the above equation:

$$\nabla^2 G - m^2 \frac{\partial G}{\partial \tau} = -4\pi \delta(\tau - \tau') \delta(\vec{r} - \vec{r'}). \tag{2.18}$$

If we do not consider the boundary effect, the Green's function solution for equation (2.18) is

$$G(r,\tau/r',\tau') = \frac{m}{2\sqrt{\pi}}\frac{1}{(\tau-\tau')^{1.5}}e^{-m^2\frac{|r-r'|^2}{4(\tau-\tau')}}u(\tau-\tau'), \tag{2.19}$$

where $u(\tau-\tau')$ is the step function. Here, $G(r,\tau/r',\tau')$ is already normalized to

$$\frac{m^2}{4\pi}\int G d\vec{V} = 1. \tag{2.20}$$

Then

$$\Phi(r,\tau) = \int_0^{\tau} d\tau' \int d\vec{V}' J(r',\tau')G(r,\tau/r',\tau'). \tag{2.21}$$

After some calculation, we obtain

$$\Phi(r,E) = K\frac{Q}{D_0}\frac{1}{4\pi^{1.5}r}E^{-p-\sigma+2}\int_u^{\infty}\left(1-\frac{u}{x}\right)^{\frac{p+\sigma-2}{1-\sigma}}\frac{e^{-x}}{\sqrt{x}}dx, \tag{2.22}$$

where $u = \frac{Q(1-\sigma)r^2}{4D_0}E^{1-\sigma}$. Since $N(r,E) = \Phi/QE^2$, we finally obtain

$$N(r,E) = \frac{K}{4\pi r}\frac{E^{-p}}{D_0 E^{\sigma}}\int_u^{\infty}\frac{1}{\sqrt{\pi}}\left(1-\frac{u}{x}\right)^{\frac{p+\sigma-2}{1-\sigma}}\frac{e^{-x}}{\sqrt{x}}dx, \tag{2.23}$$

where $u = \frac{Q(1-\sigma)r^2}{4D_0}E^{1-\sigma}$.

Chapter 3

Gamma-ray Emission from Supernova Remnant Interaction with Molecular Clumps

Tang, X., & Chevalier, R. A. 2014, ApJ, 784, L35

Abstract

Observations of the middle-aged supernova remnants IC 443, W28 and W51C indicate that the brightnesses at GeV and TeV energies are spatially correlated with each other and with regions of molecular clump interaction, but not with the radio synchrotron brightness. We suggest that the radio emission is primarily associated with a radiative shell in the interclump medium of a molecular cloud, while the γ-ray emission is primarily associated with the interaction of the radiative shell with molecular clumps. The shell interaction produces a high pressure region, so that the γ-ray luminosity can be approximately reproduced even if shock acceleration of

particles is not efficient, provided that energetic particles are trapped in the cooling region. In this model, the spectral shape $\gtrsim$ 2 GeV is determined by the spectrum of cosmic ray protons. Models in which diffusive shock acceleration determines the spectrum tend to underproduce TeV emission because of the limiting particle energy that is attained.

3.1 Introduction

A highlight of high energy γ-ray astronomy, involving space-based observations at GeV energies and ground-based observations at TeV energies, has been the detection of middle-aged supernova remnants (SNRs) interacting with molecular clouds (MCs) (see Uchiyama 2011; Fernandez et al. 2013, for reviews). Following pioneering observations with *EGRET* (Esposito et al. 1996), the *Fermi* and *AGILE* observatories observed GeV γ-ray emission from several middle-aged SNRs which are interacting with MCs, including W51C (Abdo et al. 2009), W44 (Abdo et al. 2010a), IC 443 (Tavani et al. 2010; Abdo et al. 2010b), and W28 (Abdo et al. 2010c). Of these, TeV emission is also detected in W51C (Aleksić et al. 2012), IC 443 (Albert et al. 2007) and W28 (Aharonian et al. 2008). In the cases of W28 (Aharonian et al. 2008) and W44 (Uchiyama et al. 2012), there is γ-ray emission external to the remnants that may be associated with the remnants. The high energy emission from these sources has generally been interpreted in terms of pion-decays from cosmic ray (CR) interactions.

Two scenarios have been proposed to explain the properties of these middle-aged SNRs associated with MC interaction. In one, relativistic particles escape from a SNR and interact with a nearby MC; TeV emission is produced by interaction between escaping CR particles and the MC, while GeV emission is produced by interaction between galactic CR background particles and the MC (Gabici et al. 2009; Torres et al. 2010). In view of the two components, this scenario naturally produces double peaked γ-ray spectra.

The other scenario, discussed here, involves radiative shock waves (Chevalier 1977; Blandford & Cowie 1982; Chevalier 1999; Bykov et al. 2000; Uchiyama et al. 2010). The compressed region downstream from a radiative shock is promising because of the high particle number density and energy density. Uchiyama et al. (2010) presented a crushed cloud model for W44, IC 443, and W51C, based on remnant parameters from Reach et al. (2005) for W44. In this view, the SNR has a $500\,\mathrm{km\,s^{-1}}$ nonradiative shock in most of the volume and drives $100\,\mathrm{km\,s^{-1}}$ radiative shock waves into clouds with a density of 200 $\mathrm{cm^{-3}}$. Ambient CRs experience diffusive shock acceleration (DSA) as well as adiabatic compression in the shell. The cooling region downstream from the shock front is presumed to be the site of γ-ray emission and radio synchrotron emission.

Here, we examine the γ-ray emission properties of IC 443, W28, and W51C in order to gain insight into the emission processes (Section 2). In Section 3, we discuss the structure of the magnetically supported radiative shell and the interaction region between shell and the MC clump (Chevalier 1999). In Section 4, we model the evolution of relativistic protons in both regions and calculate their π^0-decay emission. We compare our results with the observations of all three remnants and discuss the results in Section 5.

3.2 Emission properties

Three well observed remnants, IC 443, W51C and W28, have been detected at both GeV and TeV energies. The following points can be made based on these objects:

1) The GeV and TeV emission regions are well correlated with each other. In the case of IC 443, the centroids of the GeV and TeV emission differ, but the spatially extended regions of emission largely overlap in the southeast part of the remnant (Abdo et al. 2010b). For W28, Figure 1 of Aharonian et al. (2008) shows that the H.E.S.S. TeV source J1801-233 is correlated with the GeV source from *EGRET* and both are in the eastern part of the remnant. For W51C, the TeV emission measured by

MAGIC correlates with the GeV emission observed by *Fermi*, although the situation is complicated by a possible pulsar wind nebula (Figure 4 of Aleksić et al. 2012).

2) The high energy γ-ray emission is spatially correlated with regions of molecular shock interaction. In IC 443, the GeV and TeV emission are correlated with the region where there are shocked CO clumps (Figure 5 of Abdo et al. 2010b). In W28, the H.E.S.S J1801-233 source closely overlaps a region of shocked molecular emission (Figures 1 and 2 of Nicholas et al. 2012). Figure 1 of Uchiyama (2011) shows that the highest surface brightness GeV emission in W51C correlates well with a region of shocked MC (Koo & Moon 1997).

3) The three remnants have similar γ-ray spectra from GeV to TeV energies and are distinct from younger remnants (Figure 1 in Cardillo et al. 2012). The spectra do not clearly show evidence for more than one component. The shape of the spectra at low energies is consistent with γ-rays from π^0-decays (Ackermann et al. 2013). The similar GeV to TeV flux ratios for the remnants can also be seen in Figure 1 of Fernandez et al. (2013).

4) The brightest γ-ray emission is not well correlated with nonthermal radio emission, e.g., IC 443 and W28 (Figure 1 of Uchiyama 2011), although Uchiyama (2011) notes that the spatial extent of the GeV emission region is comparable to the radio remnant for these 3 objects. However, the radio structure in IC 443 is well correlated with optical emission from radiative shock fronts with velocities of $65 - 100\,\mathrm{km\,s^{-1}}$ and preshock densities of $10 - 20$ cm^{-3} (Fesen & Kirshner 1980). In W28, the radio emission is brightest on the north side of the remnant (Brogan et al. 2006), while the high energy emission is to the east and northeast. In W51C, there is radio emission overlapping the GeV emission, but there is also more radio emission to the north (Figure 1 of Uchiyama 2011).

The close correlation of GeV and TeV emission with MC interactions as well as the single component spectra suggests that the emission is not from escaping CRs for these 3 remnants, but from radiative shock waves. However, there is a distinction between regions of high radio brightness, which are not particularly correlated with shocked molecular emission, and regions of high γ-ray brightness, which are. The emission can be interpreted in the context of the MC interaction model of Chevalier (1999). The radio emission is from the radiative shell formed when the shock front moves into the interclump medium (ICM) of the MC with a density of $\sim 5-25$ cm^{-3}. This shell may be the source of some high energy γ-ray emission, but the brightest emission is from the regions of molecular clump interaction. The collision of the radiative shell with a molecular clump produces a region of especially high energy density which is promising for γ-ray emission.

3.3 Clump interaction

We assume that the radiative shell in the ICM is thin and supported by magnetic pressure. The shock wave is strong, so $B_{ts}^2/8\pi = \rho_0 V_s^2$, where B_{ts} is the tangential magnetic field in the shell, $\rho_0 = \xi_H n_0 m_p$ is the density of the ICM, and V_s is the shock velocity. We assume a helium number abundance of 10% hydrogen nuclei ($\xi_H = 1.4$); from here on, ambient number density refers to hydrogen nuclei. Based on the conservation of mass and magnetic flux in the shell (Chevalier 1977), the density in the shell is

$$\rho_s = \frac{2}{3}\alpha\rho_0\frac{R_s^3 - R_b^3}{R_s^3 - R_b^2 R_s}, \tag{3.1}$$

where $\alpha = B_{ts}/B_{t_0}$ is the compression factor, R_s is the shock radius, and R_b is the radius at the cooling time $t_b = (t_{sf} + t_{PDS})/2$, where t_{sf} and t_{PDS} are as in Cioffi et al. (1988). For an ambient magnetic field B_0 tangled on a scale much smaller than R_s, $B_{t_0}^2 = (2/3)B_0^2$. Zeeman measurements of diffuse and molecular clouds show that the total magnetic field B within clouds tends to be constant $\lesssim 10\ \mu$G ($n_0 < 300$ cm^{-3}) and $\propto n_0^{\kappa}$ where $\kappa \approx 0.65$ ($n_0 > 300$ cm^{-3}) (Crutcher 2012).

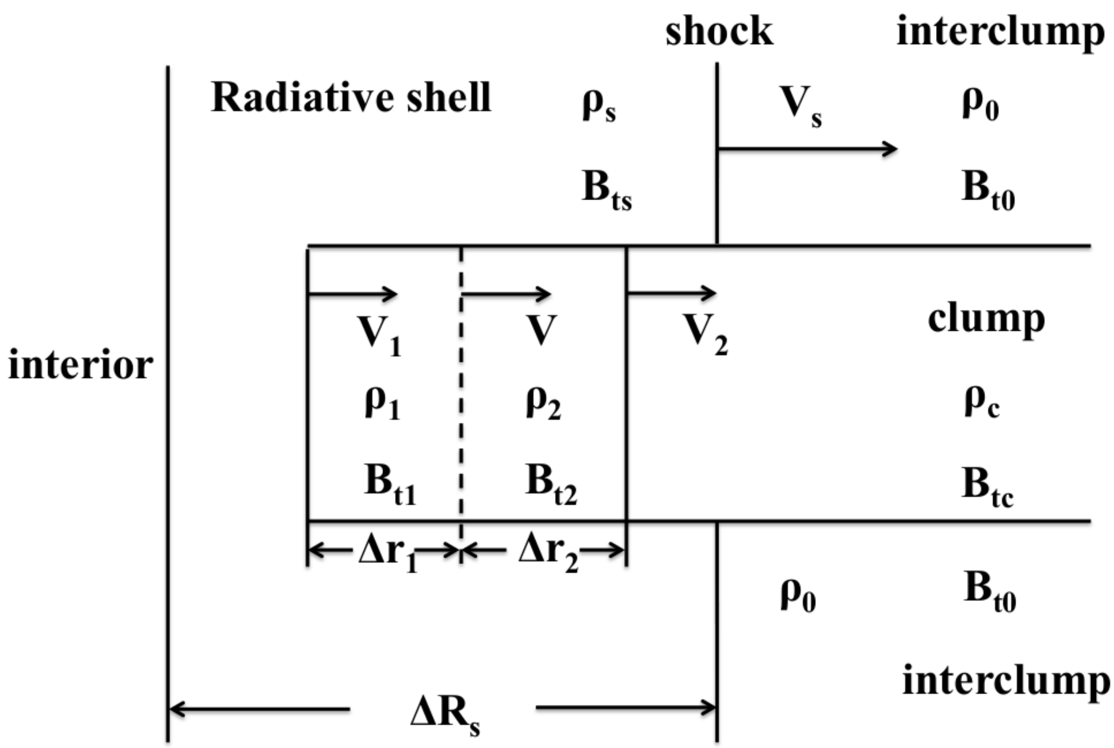

Fig. 3.1.— Schematic figure of the interaction between the radiative shell and a molecular clump. See the text for definitions.

We simplify the collision between the radiative shell and MC clump to a one-dimensional (1-D) problem in order to obtain an analytical solution for the structure of layers 1 and 2 (Figure 3.1). We assume both cooled layers are supported by magnetic pressure. The thicknesses of layers 1 and 2 follow the kinetic relations $\Delta r_1 = (V - V_1)t_c$ and $\Delta r_2 = (V_2 - V)t_c$,, where t_c is the time since collision and V_1 and

V_2 are the velocity for layer 1 and layer 2. V is the velocity of the discontinuity between layers 1 and 2. Mass conservation yields $(V_s - V_1)t_c\rho_s = \Delta r_1\rho_1$ and $V_2 t_c\rho_c = \Delta r_2\rho_2$ where ρ_1, ρ_2 and ρ_c are density for layer 1, layer 2 and the MC clump, respectively. Magnetic flux conservation gives $(V_s - V_1)t_c B_{ts} = \Delta r_1 B_{t1}$ and $V_2 t_c B_{tc} = \Delta r_2 B_{t2}$, where B_t, B_{t1}, B_{t2} and B_{tc} denote the tangential magnetic field for the shell, layer 1, layer 2, and MC clump, respectively. Magnetic pressure support for layers 1 and 2 requires $B_{t2}^2/8\pi = \rho_c V_2^2$ and $B_{t1}^2/8\pi = \rho_s(V_s - V_1)^2$, where we have neglected the preshock magnetic pressure because it is only a few % of the ram pressure. Pressure balance at the discontinuity gives $B_{t1}^2/8\pi = B_{t2}^2/8\pi$. In the above relations, V_s and V are from observations while ρ_s and B_{ts} can be calculated for a magnetically supported shell. At the time t_{MC} that layer 1 breaks out the shell, i.e. $\Delta r_1 = \Delta R_s$, all the unknown parameters can be found, using the relation between B_{tc} and ρ_c (Crutcher 2012). The parameters for IC 443 are listed in Table 3.1 based on van Dishoeck et al. (1993), Chevalier (1999), and Cesarsky et al. (1999). These values are only representative, as there are expected to be variations in different parts of the remnant and among different clumps.

3.4 Relativistic particle evolution and emission

In the radiative shock models of Blandford & Cowie (1982) and Uchiyama et al. (2010), pre-existing CRs were assumed to be accelerated at the shock by DSA and then accumulated in the dense shell due to adiabatic compression. Bykov et al. (2000) considered cases where there is injection of thermal particles into the acceleration process. When clump interaction occurs (Chevalier 1999), CRs trapped in the radiative shell and pre-existing CRs in the clumps undergo acceleration after being swept up by the clump interaction shock and then accumulated in layers 1 and 2 respectively. We

Table 3.1: Basic parameters for the IC 443 model

SNR dynamics	
Explosion energy, E	0.45×10^{51} erg
Age, t_{age}	22.3 kyr
SNR radius, R	7.4 pc
Shock velocity, V_s	100 km/s
Shock compression ratio, λ_s	4
Simulation start time, t_b	4.4 kyr
MC clump and ICM	
Preshock ICM density, n_0	15 cm^{-3}
Magnetic field in ICM, B_0	5 μG
MC clump density, n_c	1×10^4 cm^{-3}
Magnetic field in MC clump, B_c	51 μG
Radiative shell and MC clump interaction region	
Discontinuity velocity of clump shock, V	25 km/s
MC clump interaction break out time, $t_{\rm MC}$	0.37 kyr
Density in the radiative shell at t_{age}, n_s	9×10^2 cm^{-3}
Magnetic field in the radiative shell at t_{age}, B_{ts}	3×10^2 μG
Density in layer 1, n_1	6×10^3 cm^{-3}
Magnetic field in layer 1, B_{t1}	2×10^3 μG
Layer 1 velocity, V_1	12 km/s
Shock compression ratio for layer 1, λ_1	3.4
Density in layer 2, n_2	5×10^5 cm^{-3}
Magnetic field in layer 2, B_{t2}	2×10^3 μG
Layer 2 velocity, V_2	26 km/s

use the same number density of pre-existing CR protons $n_{GCR}(p) = 4\pi J\beta^{1.5}p_0^{-2.76}$ as in Uchiyama et al. (2010) but with a low energy cutoff of 3 MeV and a high number density limit of 2.5 cm^{-2} s^{-1} sr^{-1} GeV^{-1} to approximate the Voyager 1 data (Stone et al. 2013). This result also provides a reasonable approximation up to several TeV; a detailed fit to the proton spectrum in Adriani et al. (2011) does not significantly affect our results. We assume that the CR properties in clumps are the same as in the ICM and they are similar to those in the rest of the Galaxy. *Fermi* observations of nearby MCs show evidence for a relativistic particle population that is similar to that observed near Earth (Yang et al. 2014).

We assume all the γ-ray emission comes from the shell and the clump interaction region, and we only model the radiative phase of the SNR from t_b to t_{age}. The time evolution of the total number of CR protons $N(E,t)$ in the shell follows (Sturner et al. 1997)

$$\frac{\partial N(E,t)}{\partial t} = \frac{\partial b(E,t)N(E,t)}{\partial E} + Q(E,t) - \frac{N(E,t)}{\tau_{pion}}, \tag{3.2}$$

where $b(E,t) = -dE/dt$ is the energy loss term for protons including adiabatic expansion and Coulomb collisions. τ_{pion} characterizes the loss time of CR protons due to $p-p$ interactions, $\tau_{pion}(E_p) = 1/(c\beta_p n\sigma_{pp})$, where the $p-p$ cross section σ_{pp} is from Kelner et al. (2006). The particle injection rate is

$$Q(E,t) = \frac{Q(p,t)}{v(p)} = \frac{4\pi R_s^2(t)V_s(t)(1-w)}{v(p)s(t)} n_{in}(p,t), \tag{3.3}$$

where $v(p)$ is the proton velocity for momentum p, $s(t) = n_s(t)/n_0$ is the total density compression ratio in the shell, and w is the surface area filling factor. The shell radius and velocity, $R_s(t)$ and $V_s(t)$, are from the analytical solution of Cioffi et al. (1988). For the injected CR number density after acceleration, $n_{in}(p,t)$, we considered two cases. In one, DSA at the shock and further adiabatic compression in the cooling shell gave (Uchiyama et al. 2010)

$$n_{in}(p,t) = [s(t)/\lambda_s]^{2/3} n_{DSA}([s(t)/\lambda_s]^{-1/3} p), \tag{3.4}$$

where $n_{DSA}(p)$ is the number density of pre-existing CRs after DSA and $\lambda_s = 4$ is the strong shock compression ratio. The other case is pure adiabatic compression, with $n_{in}(p,t) = s^{2/3}(t)\ n_{GCR}[s^{-1/3}(t)p]$.

After obtaining $N(E, t_{age})$ in the shell from equation (3.2), the total number of CR protons in layer 1, $N_1(E, t_c)$, and layer 2, $N_2(E, t_c)$, could be found in the same way as for the clump interaction from t_{age} to $t_{age} + t_{MC}$, but with a different source term. Because the collision time t_c is coupled to the filling factor w in the 1-D case, we set $t_c = t_{MC}$ and then fit the data by varying w; this gives the minimum value for w. Our model only applies to the situation $t_c \le t_{MC}$; if $t_c > t_{MC}$, layer 1 breaks out of the shell, complicating the situation, and the emission is expected to fade. With the parameters of interest here, we find the breakout time $t_{MC} = \Delta R_s/(V_s - V_1) \sim 0.4$ kyr $\ll t_{age} - t_b$, so we can neglect the evolution of the radiative shell when we calculate the structure of layers 1 and 2.

The shock at layer 2 is a slow nonionizing shock so we only consider the pure adiabatic case,

$$Q_2(E, t_c) = \frac{Q_2(p, t_c)}{v(p)} = \frac{4\pi R_s^2 (V_2 - V) w}{v(p)} s_2^{2/3} n_{GCR}(s_2^{-1/3} p). \tag{3.5}$$

For layer 1,

$$Q_1(E, t_c) = \frac{Q_1(p, t_c)}{v(p)} = \frac{4\pi R_s^2 (V - V_1) w}{v(p)} n_{in,1}(p). \tag{3.6}$$

In the pure adiabatic case, $n_{in,1}(p) = s_1^{2/3}\ n_{age}(s_1^{-1/3} p)$, where $n_{age}(p)$ is the number density in the radiative shell at t_{age}, while for the DSA case $n_{in,1}(p) = (s_1/\lambda_1)^{2/3}$ $n_{DSA,1}((s_1/\lambda_1)^{-1/3}p)$ where $n_{DSA,1}(p)$ is the number density $n_{age}(p)$ after DSA. s_1 and s_2 are the density compression ratios for layers 1 and 2. λ_1 is the shock compression ratio for layer 1 and is calculated from the jump conditions for a perpendicular shock (Draine & McKee 1993). Equation (3.2) is calculated numerically with the Crank-Nicolson method for both shell and clump interaction region.

The efficiency of DSA is limited by the available particle acceleration time, t_{acc}. For shell evolution $t_{acc} = t_{age} - t_b$, while for clump interaction $t_{acc} = t_{MC} - t_c$. By comparing t_{acc} with the timescale for DSA $t_{DSA} \simeq (10/3)\eta c r_g v_{shock}^{-2}$, where r_g is the gyro radius and $\eta \geq 1$ is the gyro factor, we introduce an exponential cutoff at p_{max} (Uchiyama et al. 2010) for the CR number density in both the shell and layer 1. Here, we assume $\eta = 1$ to obtain the most efficient DSA. When $p > p_{max}$, $t_{acc} < t_{DSA}$, limiting the energy particles can reach. For a typical radiative SNR, $p_{max} \approx 96\ (10/\eta)(t_{acc}/20\ \mathrm{kyr})\ (B_0/5\ \mu\mathrm{G})(V_s/100\,\mathrm{km\,s^{-1}})^2\ \ \mathrm{GeV}/c$. For a shock with $V_s \lesssim 100\,\mathrm{km\,s^{-1}}$ running into a dense medium, the shock precursor is not strongly ionized and ion neutral damping of Alfven waves becomes important. As a result, high energy CR particles can escape the DSA site, bringing a steepening factor p_{br}/p to the particle spectrum when $p > p_{br}$; the break momentum is $p_{br} \approx 9.4(B_0/1\ \mu\mathrm{G})^2$ $(T/10^4\ \mathrm{K})^{-0.4}\ (1\ \mathrm{cm}^{-3}/n_0)(1\ \mathrm{cm}^{-3}/n_i)^{1/2}\ \mathrm{GeV}/c$ (Malkov et al. 2011).

Trapping of CR particles in the cooling region due to the high tangential magnetic field might also limit DSA. By comparing the column density of the downstream acceleration region $N_c = n_0 V_s t_{DSA}$ with that for gas to cool down to 10^4 K and become radiative $N_{cool} \approx 3 \times 10^{17}(V_s/10^2\,\mathrm{km\,s^{-1}})^4$ for $60 < V_s < 150\,\mathrm{km\,s^{-1}}$ (McKee et al. 1987), we obtain a critical momentum $p_{cr} \approx 9.1(1/\eta)(B_0/1\ \mu\mathrm{G})(1\ \mathrm{cm}^{-3}/n_0)$ $(V_s/100\,\mathrm{km\,s^{-1}})^5\ \mathrm{GeV}/c$. When $p \gtrsim p_{cr}$, particles may be trapped in the dense region before DSA is complete.

The γ-ray emission from π^0-decays in the radiative shell and clump interaction region is calculated based on Kamae et al. (2006), which gives results consistent with Dermer (1986) within 15%. The scaling factor χ for helium and heavy nuclei is taken to be 1.8 (Mori 2009). The γ-ray flux density at E_γ is (Sturner et al. 1997; Kamae et al. 2006)

$$F_{\pi^0}(E_\gamma, t_{age}) = \frac{\chi E_\gamma}{4\pi d^2} \int dV \int_{E_{p,thresh}}^{\infty} dE_p 4\pi n_s(t_{age}) J_p(E_p, t_{age}) \frac{d\sigma(E_\gamma, E_p)}{dE_\gamma}. \tag{3.7}$$

Given the proton flux density $J_p(E, t_{age}) = c\beta_p n_{in}(E, t_{age})/4\pi$ and assuming that the shell is uniform, after some calculation we obtain

$$F_{\pi^0}(E_\gamma, t_{age}) = \frac{\chi E_\gamma c n_s(t_{age})}{4\pi d^2} \int_{E_{p,thresh}}^{\infty} dE_p \beta_p \frac{d\sigma(E_\gamma, E_p)}{dE_\gamma} N(E_p, t_{age}). \tag{3.8}$$

In the above equation, $n_s(t_{age})$ and $N(E_p, t_{age})$ need to be replaced by $n_1(t_{MC})$ and $N_1(E_p, t_{MC})$ for layer 1, and $n_2(t_{MC})$ and $N_2(E_p, t_{MC})$ for layer 2 when calculating emission from the clump interaction region.

We calculated the electron bremsstrahlung component for our models, assuming a 1 to 100 abundance ratio of cosmic ray electrons to protons. The leptonic emission is not significant compared to the hadronic emission in view of the low abundance of electrons.

3.5 Results and discussion

We calculated the emission from IC 443 for both standard DSA and pure adiabatic cases, with our radiative shell plus MC clump interaction model and the parameters shown in Table 3.1. Ion neutral damping and a finite acceleration time were taken into account in the DSA simulation but not the limited cooling region argument due to its uncertainty. The ionization in the layer 1 precursor is low so we only considered ion neutral damping for the shell, finding that $p_{br} \sim 10$ GeV/c gives a good fit to the GeV part of the spectrum with $w = 8\%$ (Figure 3.2). The resulting γ-ray spectrum is narrower than the observed spectrum, falling below the observed emission at high energy due to the limited acceleration time. The observed spectra from GeV to TeV energies have slopes which are similar to the input CR spectrum. While pure adiabatic compression maintains the shape of the input CR spectrum, pion-decay emission also traces the energy distribution of the parent spectrum above a few GeV. We found that the pure adiabatic case can approximately fit the spectra of IC 443 from GeV to TeV energies, but with a higher $w \approx 21\%$ (Figure 3.3), which implies that the remnant is in a special phase of evolution. Alternatively, a higher value for the ICM density would reduce the value of w.

The γ-ray spectrum of W28 has a similar shape to that of IC 443, except for the low energy part (Figure 3.2; Abdo et al. 2010c; Aharonian et al. 2008). W51C's γ-ray spectrum also has a shape similar to IC 443 but the luminosity is larger (Figure 3.2; Abdo et al. 2009; Aleksić et al. 2012). W51C is a large remnant compared to the other two, and may have an unusually large energy (Koo & Moon 1997; Koo et al. 2005), which could account for the high luminosity. We do not attempt detailed models for W28 and W51C, but note the similar spectral shapes for the three remnants may be a result of the similar parent CR spectrum.

Other possible tests of the models are the shocked MC mass and the relative intensities of the three components: radiative shell, layer 1 and layer 2. In the pure adiabatic case the shocked MC mass required for IC 443 is $m_{MC} \approx V_2 t_{MC} \rho_c 4\pi R_s^2 w \approx$

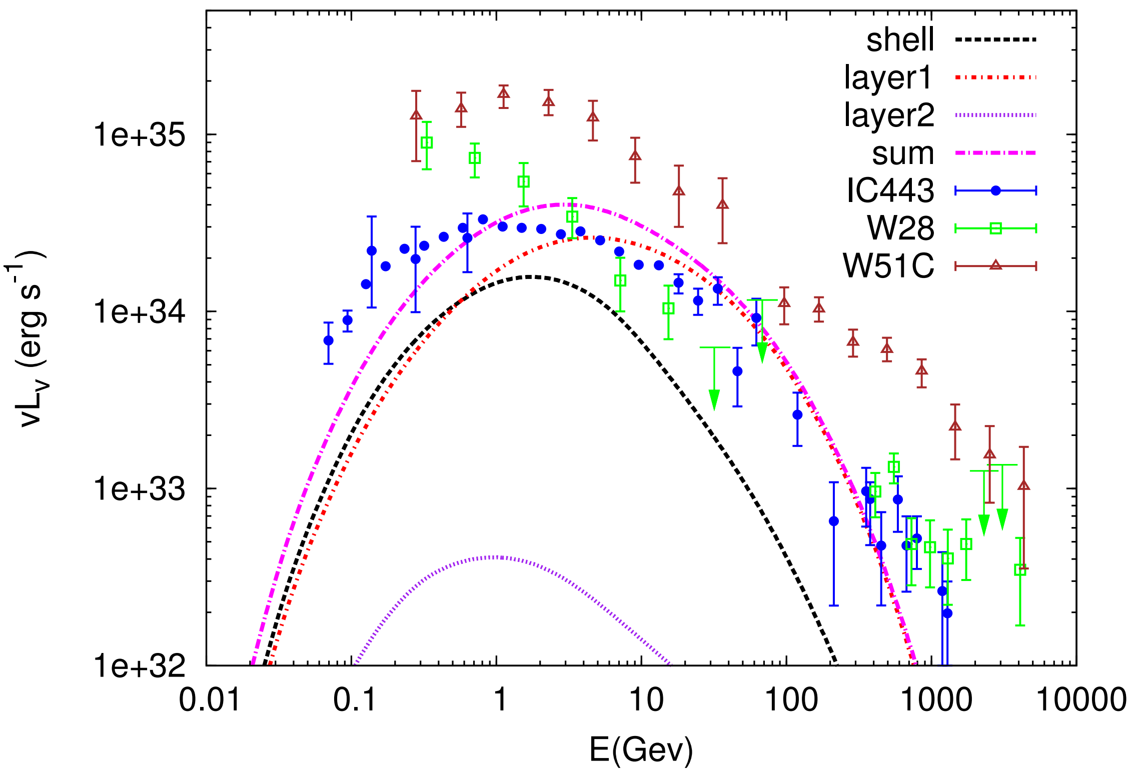

Fig. 3.2.— γ-ray emission from IC 443 in a model with DSA plus adiabatic compression. The data points for IC443 are from Ackermann et al. (2013); Albert et al. (2007); Acciari et al. (2009); Tavani et al. (2010) with a distance of 1.5 kpc; W28 from Abdo et al. (2010c) and Aharonian et al. (2008) with a distance of 2 kpc; W51C from Abdo et al. (2009) and Aleksić et al. (2012) with a distance of 4.3 kpc (Tian & Leahy 2013).

500 $M_\odot$ which is more consistent with the molecular observations (Dickman et al. 1992; Lee et al. 2008) than the 190 $M_\odot$ in our DSA model. In the pure adiabatic case, the γ-ray emission from IC 443 is naturally dominated by the MC interaction region, especially layer 1, while for the DSA case the emission from the MC interaction region is comparable to the shell component at low energy but becomes dominant at high energy. However, the surface brightness is coupled with the angle between the collision direction and the line of sight. Considering the uncertainty in both theoretical models

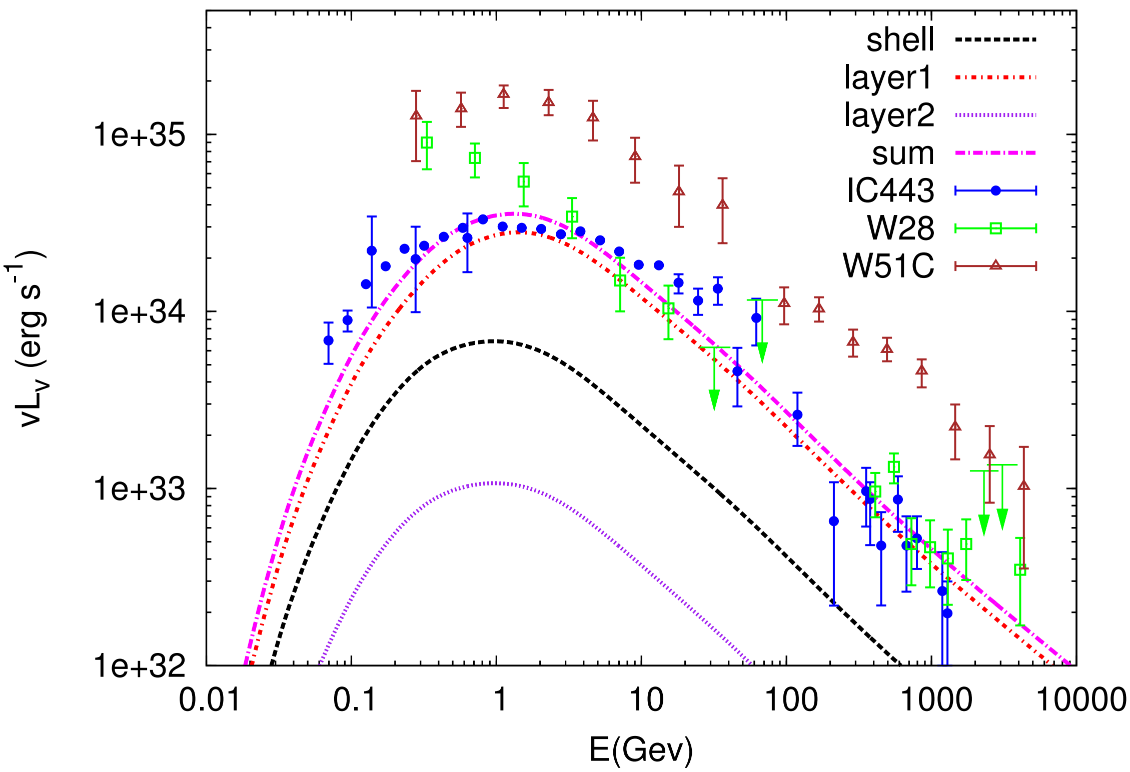

Fig. 3.3.— γ-ray data as in Fig. 3.2 compared to the pure adiabatic compression model for IC 443.

and observations, these tests are not definitive.

Here we have sought a model for the γ-ray emission from SNRs that is consistent with the emission properties given in Section 2. The correlation of GeV and TeV emission with molecular clump interaction implies that the γ-ray emission is related to slow radiative shock waves in dense matter. Standard DSA is not efficient at high energies. Pure adiabatic compression could reproduce the ratio of TeV to GeV emission but requires a large covering factor (Figure 3). Particle acceleration process in the middle-aged SNRs are still not very clear. There are other possibilities; Bykov et al. (2008) have found nonthermal X-ray emission near a clump interaction region in IC 443 which they interpret as the result of ejecta knots hitting the molecular gas. More detailed observations of the remnants discussed here, as well as other remnants with molecular cloud interaction, would improve our understanding of CR acceleration in SNRs.

Acknowledgements

We are grateful to Charles Dermer for the code used to calculate the π^0-decay emission, and to A. Bykov for useful comments. This research was supported in part by NASA *Fermi* grant NNX12AE51G.

Chapter 4

Time-dependent Diffusive Shock Acceleration in Slow Supernova Remnant Shocks

Tang, X., & Chevalier, R. A. 2015, ApJ, 800, 103

Abstract

Recent γ-ray observations show that middle-aged supernova remnants (SNRs) interacting with molecular clouds can be sources of both GeV and TeV emission. Models involving re-acceleration of pre-existing cosmic rays (CRs) in the ambient medium and direct interaction between SNR and molecular clouds have been proposed to explain the observed γ-ray emission. For the re-acceleration process, standard diffusive shock acceleration (DSA) theory in the test particle limit produces a steady-state particle spectrum that is too flat compared to observations, which suggests that the high-energy part of the observed spectrum has not yet reached a steady state. We derive a time-dependent DSA solution in the test particle limit for situations involving

re-acceleration of pre-existing CRs in the preshock medium. Simple estimates with our time-dependent DSA solution plus a molecular cloud interaction model can reproduce the overall shape of the spectra of IC 443 and W44 from GeV to TeV energies through pure π^0-decay emission. We allow for a power law momentum dependence of the diffusion coefficient, finding that a power-law index of 0.5 is favored.

4.1 Introduction

Diffusive shock acceleration (DSA) is believed to be the particle acceleration mechanism in most astrophysical environments involving shock waves (e.g., Blandford & Eichler 1987). The theory naturally produces a power law energy spectrum of energetic particles in the steady state. Accelerated particles can produce γ-ray emission through either bremsstrahlung and Inverse Compton emission of leptonic origin, or π^0-decay emission of hadronic origin, making γ-ray observations important diagnostics for particle acceleration processes in astronomical objects. Recent observations from both space-based GeV observatories and ground-based TeV observatories show that middle-aged supernova remnants (SNRs) interacting with molecular clouds can be sources of both GeV (Uchiyama 2011) and TeV (Albert et al. 2007; Aharonian et al. 2008; Aleksić et al. 2012) emission. The characteristic π^0-decay signature identified in IC 443 and W44 (Giuliani et al. 2011; Ackermann et al. 2013) provides possible direct evidence for cosmic ray (CR) particle acceleration in supernova remnants.

Two scenarios have been proposed to explain the observed GeV and TeV emission from middle-aged SNRs. In one, nearby molecular clumps are illuminated by the accelerated CR particles escaping from a SNR in addition to the pre-existing CR background, producing the GeV and TeV emission (Gabici et al. 2009; Fujita et al. 2009; Li & Chen 2010; Ohira et al. 2011); the other involves direct interaction between the SNR and the molecular clumps (Bykov et al. 2000; Uchiyama et al. 2010; Inoue et al. 2010; Tang & Chevalier 2014). In Tang & Chevalier (2014) we noted evidence that in middle-aged SNRs with both GeV and TeV emission (IC 443, W28, W51C), the emission regions are co-located and spatially correlated with the shocked molecular clump region (Abdo et al. 2010b; Uchiyama 2011; Nicholas et al. 2012), which indicates there is direct interaction between the SNR and molecular clumps. In the direct interaction scenario, re-acceleration of pre-existing CRs has been considered while particle injection through the thermal pool is neglected in view of the slow radiative shock (Blandford & Cowie 1982; Uchiyama et al. 2010). Recent observations of nearby giant molecular clouds by *Fermi* reveal γ-ray emission as a result of interaction between the Galactic CR background and giant molecular clouds (Yang et al. 2014), showing the importance of the pre-existing CR component. The standard DSA theory produces too flat a steady state particle spectrum compared to that indicated by observations, so it has been suggested that there is insufficient time to reach the steady state particle spectrum in the energy region of interest; the upper limit based on the acceleration timescale has been implemented as an exponential cutoff in the particle spectrum (Uchiyama et al. 2010; Tang & Chevalier 2014). While this model compares well to data in the GeV range, it falls below the observations in the TeV range (Uchiyama et al. 2010; Tang & Chevalier 2014). Tang & Chevalier (2014) further found that a model, in which the energetic particles are compressed in the radiative shock fronts with no DSA, is able to reproduce the observed spectral shapes of the high energy γ-ray emission. Although this model has attractive features, it requires a high covering factor for the shock wave emission and it is unclear why DSA is not occurring.

Here, we examine in more detail the case, where DSA is occurring but it has not had time to reach a steady state. Time-dependent test particle DSA was first discussed in detail by Toptygin (1980). An analytic solution for continuous injection of a monoenergetic spectrum at the shock front with source term $S = \delta(x)\delta(p - p_0)$ (where p is particle momentum and p_0 is the injected momentum), was obtained in the special case that the shock velocity U and diffusion coefficient κ are constant, and the ratio $\kappa_1/U_1^2 = \kappa_2/U_2^2$, where the subscript 1 refers to upstream and 2 to downstream. Forman & Drury (1983) solved the case that κ has a power law dependence on momentum in the limit that $p \gg p_0$. Drury (1991) extended the solution to a more general case in which the flow velocity U and diffusion coefficient κ also have spatial dependence.

The monoenergetic spectrum assumed in the above discussions made it possible to decouple the time-dependent solution into the product of the steady-state solution and a time evolution factor, which is useful for investigating the acceleration timescale for individual particle in the system. The resulting acceleration time is in good agreement with the discussion from the microscopic method (Lagage & Cesarsky 1983). However there has been less attention to the evolution of the spectral shape for a group of particles with an arbitrary spectrum. Here, we consider the case where the upstream region is filled with seed particles, in particular, pre-existing CRs. We limit our discussion to DSA in the test particle limit for simplicity, as has been assumed in previous discussions of middle-aged remnants with slow shock waves (Blandford & Cowie 1982; Uchiyama et al. 2010)

In Section 2, the time-dependent DSA solution for a shock wave interacting with pre-existing CRs is derived for both energy independent diffusion and energy dependent diffusion. In Section 3, we then calculate the π^0-decay emission from IC 443 and W44 based on our time-dependent solution and compare the results to observations. Aspects of our model are discussed in Section 4.

4.2 Particle spectrum

We consider a plane parallel shock wave and constrain our discussion to the shock frame. The shock front is at $x = 0$ and the flow is moving toward the positive x direction with flow velocity $U = U_1 + (U_2 - U_1)H(x)$, where the subscripts 1 and 2 refer to upstream and downstream, respectively, throughout the paper and $H(x)$ is the step function. Here, we are mostly interested in the radiative phase of the SNR when the shock is slow and the test particle theory may be applicable. In the early phases of the SNR, the shock is fast and non-linear effects may be important. As a result, the accelerated particle distribution in the early phase of a SNR is difficult to model. Fortunately, the total number of CR particles accelerated in a remnant before the radiative phase is likely to be small compared to the pre-existing CRs swept up in the radiative phase for the energy range we are interested in. The remnant spends most of its time and sweeps up most of its volume in the radiative phase. We ignore the particles accelerated in the early phase of the remnant to simplify the calculation and consider only re-acceleration of pre-existing CRs in the radiative phase. We investigate a situation with seed particles in the shock upstream region; the shock front starts to interact with the seed particles at time $t = 0$. The advection and diffusion equation we need to solve becomes (Drury 1983)

$$\frac{\partial f}{\partial t} + U\frac{\partial f}{\partial x} = \frac{\partial}{\partial x}\left(\kappa\frac{\partial f}{\partial x}\right) + \frac{\partial U}{\partial x}\left(\frac{p}{3}\frac{\partial f}{\partial p}\right) + Q(p)\delta(t)H(-x), \tag{4.1}$$

where $f(x,t,p)$ is the isotropic part of the particle phase space density, $\kappa = \kappa_1 + (\kappa_2 - \kappa_1)H(x)$ is the diffusion coefficient and $Q(p)\delta(t)H(-x)$ is the source term representing the pre-existing CRs in the upstream region. The above equation is correct only when $v \gg U \gg U_A$, where v is the particle velocity and U_A is the Alfven velocity for the magnetic irregularities. The condition $v \gg U$ implies that the result cannot be applied to relativistic shocks. The condition $U \gg U_A$ requires that the magnetic field cannot be too strong or second order Fermi acceleration would be important and we would need to add a momentum diffusion term to equation (4.1). The presence of the shock discontinuity requires a matching condition at the shock front to solve the equation. The easiest way to obtain the matching condition is to integrate equation (4.1) from $x = -0$ to $x = +0$ with weight function 1 and $\int dx/\kappa$. The resulting matching conditions are

$$[f]_{-0}^{+0} = 0 \qquad \text{and} \qquad \left[\kappa\frac{\partial f}{\partial x} + \frac{U}{3}p\frac{\partial f}{\partial p}\right]_{-0}^{+0} = 0. \tag{4.2}$$

In this paper, we are primarily interested at the time evolution of the spectral shape in the downstream region, which is determined by the ratio t/τ. τ is a time scale characterizing the DSA in the system, which will be chosen in a form to simplify the calculation. It is more convenient to use the dimensionless time factor t/τ than time t. Defining $\Theta = t/\tau$ and assuming $h(x, \Theta, p) = f(x, t, p)$, we find that the advection and diffusion equation becomes

$$\frac{1}{\tau}\frac{\partial h}{\partial \Theta} + U\frac{\partial h}{\partial x} = \frac{\partial}{\partial x}\left(\kappa\frac{\partial h}{\partial x}\right) + Q(p)H(-x)\frac{\delta(\Theta)}{\tau}, \tag{4.3}$$

while the matching conditions are now

$$[h]_{-0}^{+0} = 0 \qquad \text{and} \qquad \left[\kappa\frac{\partial h}{\partial x} + \frac{U}{3}p\frac{\partial h}{\partial p}\right]_{-0}^{+0} = 0. \tag{4.4}$$

Following the procedure in Drury (1991), we perform a Laplace transform of the advection and diffusion equation, assuming

$$g(x, s, p) = \int_0^\infty h(x, \Theta, p)e^{-s\Theta}d\Theta. \tag{4.5}$$

Then equation (4.3) becomes

$$\frac{sg}{\tau} + U\frac{\partial g}{\partial x} = \kappa\frac{\partial^2 g}{\partial x^2} + \frac{Q(p)H(-x)}{\tau}. \tag{4.6}$$

Since $f \to 0$ when $x \to +\infty$ and $f \to Q(p)H(t)H(-x)$ when $x \to -\infty$, we have $g \to 0$ when $x \to +\infty$ and $g \to Q(p)H(-x)/s$ when $x \to -\infty$. With these boundary conditions, the solution to the ordinary differential equation has the form

$$g(x,s,p) = \begin{cases} c_1(s,p)e^{(A_1+2)xU_1/2\kappa_1} + Q(p)/s, & \text{if } x < 0 \\ c_2(s,p)e^{-A_2xU_2/2\kappa_2}, & \text{if } x > 0, \end{cases} \tag{4.7}$$

where

$$A_1 = \sqrt{1+\tau_1 s/\tau} - 1, \qquad A_2 = \sqrt{1+\tau_2 s/\tau} - 1, \tag{4.8}$$

and

$$\tau_1 = \frac{4\kappa_1}{U_1^2}, \qquad \tau_2 = \frac{4\kappa_2}{U_2^2}. \tag{4.9}$$

The quantities $c_1(s,p)$ and $c_2(s,p)$ can be calculated by applying the matching conditions, equation (4.4). After some calculation we obtain the downstream solution

$$\begin{aligned} g(x,s,p) &= c_2(s,p)e^{-A_2xU_2/2\kappa_2} \\ &= \alpha p^{-\alpha} e^{-A_2xU_2/2\kappa_2} \int_0^p p'^{\alpha-1}\, Q(p')\, dp'\, \frac{A_1+2}{2s}\, e^{-\int_{p'}^{p} \Delta\alpha\, dp''/p''} \end{aligned} \tag{4.10}$$

where $\alpha = 3U_1/(U_1 - U_2)$ and $\Delta\alpha = 3(U_1A_1 + U_2A_2)/2(U_1 - U_2)$.

In this paper we limit our discussion to the situation that the shock velocity U is constant while the diffusion coefficient κ can have an energy dependence. We assume κ is constant in space because the spatial dependence of κ requires detailed information about the shock structure, which is beyond the discussion here. The spatially independent diffusion coefficient κ applied in the following discussion can be considered as a spatially averaged value. We assume $\tau_1 = \tau_2$ for simplicity, which requires $\kappa_1 = 16\kappa_2$ for a strong shock by the definition $\tau = 4\kappa/U^2$. It is a strong constraint not always satisfied in actual situations. We denote the quantities in the general situation with a hat symbol $\hat{()}$. In the case $\hat{\tau_1} \neq \hat{\tau_2}$, the spectral shape of the time-dependent solution is mainly determined by the $\max\{\hat{\tau_1}, \hat{\tau_2}\}$, since $\hat{\tau_1}$ and $\hat{\tau_2}$ together characterize the DSA time scale of the system. The simplified τ derived in our spectral fits can be considered as a good approximation to the $\max\{\hat{\tau_1}, \hat{\tau_2}\}$ (i.e. $\tau = \tau_1 = \tau_2 \approx \max\{\hat{\tau_1}, \hat{\tau_2}\}$). For the SNR forward shock, it is likely that $\hat{\kappa_1} \gg 16\hat{\kappa_2}$ and $\hat{\tau_1} \gg \hat{\tau_2}$, because the diffusion coefficient in the upstream region gradually increases from a value close to Bohm limit near the shock front to the value of the CR diffusion coefficient in the ISM far away from the shock front. The result $\tau \approx \max\{\hat{\tau_1}, \hat{\tau_2}\} = \hat{\tau_1}$ thus can provide information on the spatially averaged diffusion coefficient in the upstream region, which can also be taken as an upper limit to the CR diffusion coefficient close to the shock front. We start with the case where κ is independent of energy and then discuss the situation where κ has a power law dependence on particle momentum.

4.2.1 Energy Independent Diffusion

For the case U and κ are constant and satisfy $\tau_1 = \tau_2$, the analytic solution for $f(x,t,p)$ can be obtained by performing an inverse Laplace transform on equation (4.10). Defining $\tau = \tau_1 = \tau_2$, we obtain the analytic solution

$$\begin{aligned} f(x,t,p) &= h(x,\Theta,p) = \mathcal{L}^{-1}\{g(x,s,p)\} \\ &= \alpha p^{-\alpha} \int_0^p p'^{\alpha-1} Q(p')\, dp' \, \frac{1}{2} \left\{ \frac{1}{\sqrt{\pi\Theta}} e^{-w^2} + \mathrm{erfc}(w) \right\}, \end{aligned} \tag{4.11}$$

where $w = \beta/2\sqrt{\Theta} - \sqrt{\Theta}$ and $\beta = \Delta\alpha \ln(p/p')/A_2 + xU_2/2\kappa_2$. The result can also be obtained by integrating the solution in Toptygin (1980) over the source position z_0 from $-\infty$ to 0.

We assume strong shock conditions throughout the paper except for the slow molecular shock discussed later, and that $Q(p)$ follows the same CR spectrum as in Tang & Chevalier (2014). The calculated downstream particle spectrum at the shock front ($x = 0$) for various Θ is shown in Fig 4.1. In the Appendix, we provide a simple argument for understanding the resulting spectral shape with energy independent diffusion. There is a critical momentum below which the spectrum reaches the steady-state solution, while above it the spectrum recovers the steep power law shape of the input CR spectrum at high energy. The particle spectrum of interest for comparison

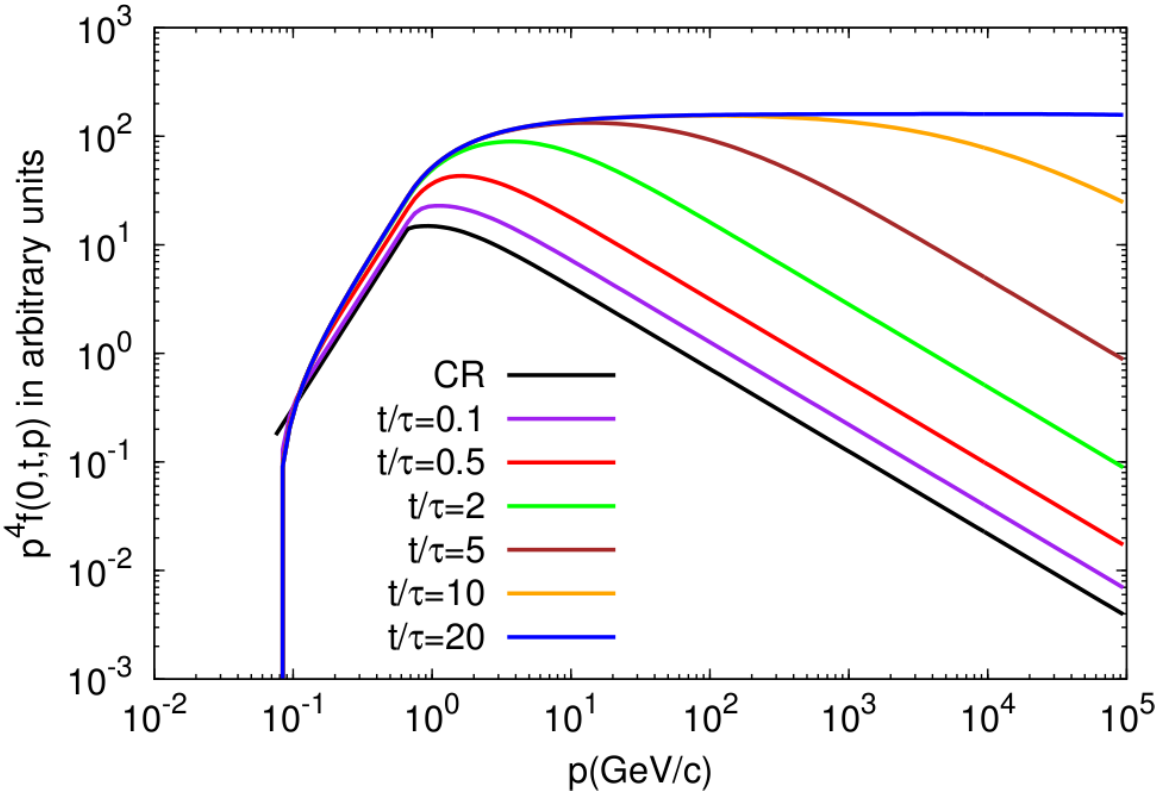

Fig. 4.1.— Time evolution of the particle momentum spectrum at the shock front for various time ratios. CR denotes the ambient cosmic ray spectrum. The diffusion coefficient is taken to be independent of energy.

with observations is the spectrum of all the accumulated particles integrated over the downstream region, which is calculated by

$$
\begin{aligned}
F(t,p) &= \mathcal{L}^{-1}\left\{\int_0^\infty g(x,s,p)dx\right\} \\
&= \frac{U_2 t}{2\Theta}\alpha p^{-\alpha}\int_0^p p'^{\alpha-1}Q(p')dp'\left[\sqrt{\frac{\Theta}{\pi}}e^{-b^2}+\left(\frac{1}{2}-b\sqrt{\Theta}\right)\mathrm{erfc}(b)\right],
\end{aligned}
\tag{4.12}
$$

where $b = \Delta\alpha\ln(p/p')/2A_2\sqrt{\Theta} - \sqrt{\Theta}$. For a planar shock, $U_1 t$ is the length scale of preshock medium swept up by the shock at time t, while $U_2 t$ is the length scale of the shocked medium accumulated in the postshock region. The quantity $F_{avg}(t,p) = F(t,p)/U_2 t$ then can be considered as the spatially averaged downstream phase space density. We plot the spatially averaged downstream particle spectrum $F_{avg}(t,p)$ as a function of p for various Θ in Fig 4.2. The spectral shape evolution of $F_{avg}(t,p)$ basically follows the same trend as for $f(0,t,p)$, with a critical energy characterizing the shape of the resulting spectrum. The transition between the steady-state solution and the steep power law shape of the input CR spectrum is smoother for the spatially averaged case. The critical energy discussed here is different from the maximum energy defined in a situation in which a monoenergetic particle input spectrum is assumed. In that case there is a maximum energy that particles can achieve during the acceleration process. For our situation of re-acceleration of pre-existing CR, the concept of maximum energy is not relevant to the critical energy discussed here.

4.2.2 Energy Dependent Diffusion

When κ depends on particle momentum, the situation becomes more complicated. Forman & Drury (1983) provide the solution for a diffusion coefficient κ with a power law energy dependence but for a monoenergetic input spectrum and particle momentum much greater than particle injected momentum ($p \gg p_0$). Thus we cannot

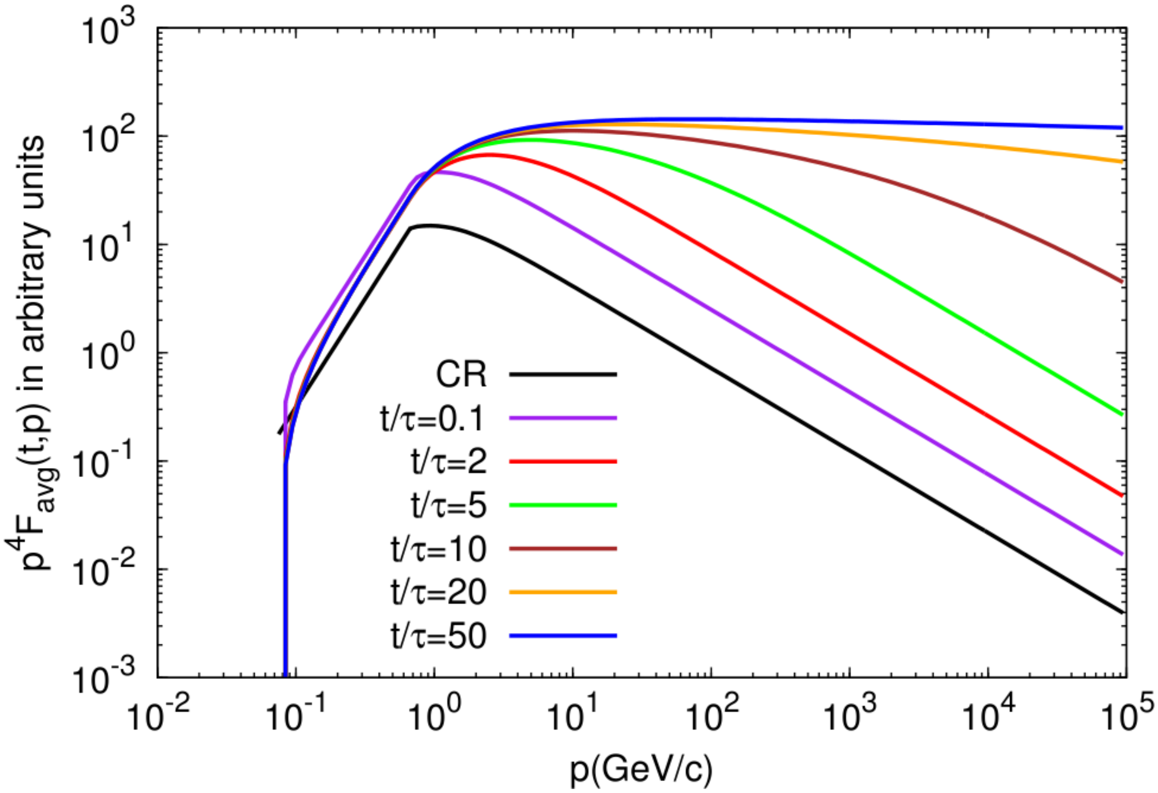

Fig. 4.2.— Spatially averaged downstream particle momentum spectrum for various time ratios; see text for details. The cosmic ray spectrum denoted by CR has arbitrary scaling.

use their solution to investigate the evolution of the spectral shape. Here we assume $\kappa = \overline{\kappa}\,\overline{p}^{\sigma}$, where $\overline{p} = pc/(1\text{ GeV})$ is the dimensionless particle momentum, and $\overline{\tau_1} = \overline{\tau_2} = 4\overline{\kappa_1}/U_1^2 = 4\overline{\kappa_2}/U_2^2$ to simplify the calculation. Following the procedure we used to solve the energy independent diffusion case, the spatially integrated particle spectrum in the downstream region is now

$$\begin{aligned} F(t,p) &= \mathcal{L}^{-1}\left\{\int_0^\infty g(x,s,p)dx\right\} \\ &= \mathcal{L}^{-1}\left\{\alpha p^{-\alpha}\int_0^p p'^{\alpha-1}\,Q(p')\,dp'\,\frac{\kappa_2[A_1(p')+2]}{A_2(p)U_2 s}\,e^{-\int_{p'}^{p}\Delta\alpha\,dp''/p''}\right\}, \end{aligned} \tag{4.13}$$

where all the parameters are the same as defined before except we now have an energy dependent diffusion coefficient $\kappa = \overline{\kappa}\,\overline{p}^{\sigma}$. Taking $\tau = \overline{\tau_1} = \overline{\tau_2}$, we have

$$
\begin{aligned}
g(s,p) = \int_0^\infty g(x,s,p)dx = \alpha p^{-\alpha} \int_0^p p'^{\alpha-1} Q(p') dp' \frac{\kappa_2}{U_2} \\
\times \frac{e^{2\Delta\alpha(\sqrt{1+sp'_\sigma}-\sqrt{1+sp_\sigma})/A_2\sigma}(1+\sqrt{1+sp_\sigma})^{(2\Delta\alpha/A_2\sigma)+1}}{p_\sigma s^2(1+\sqrt{1+sp'_\sigma})^{(2\Delta\alpha/A_2\sigma)-1}},
\end{aligned}
\tag{4.14}
$$

where $p_\sigma = \overline{p}^{\sigma}$. The corresponding spatially averaged downstream particle spectrum is

$$
\begin{aligned}
F_{avg}(t,p) = \frac{f_d(t,p)}{U_2 t} = \frac{\alpha}{4\Theta} p^{-\alpha} \int_0^p p'^{\alpha-1} Q(p') dp' \\
\times \mathcal{L}^{-1} \left\{ \frac{e^{2\Delta\alpha(\sqrt{1+sp'_\sigma}-\sqrt{1+sp_\sigma})/A_2\sigma}(1+\sqrt{1+sp_\sigma})^{(2\Delta\alpha/A_2\sigma)+1}}{s^2(1+\sqrt{1+sp'_\sigma})^{(2\Delta\alpha/A_2\sigma)-1}} \right\}.
\end{aligned}
\tag{4.15}
$$

It is difficult to calculate the above inverse Laplace transform analytically, so we used Talbot's method to do the inversion of the Laplace transform numerically (Talbot 1979). Before we applied Talbot's method to equation (4.15), we did some tests of the numerical method by comparing the numerical results with the analytical solution we derived for the energy independent diffusion case. The results based on Talbot's method were completely consistent with the analytical solution. We note that the energy dependent solution in equation (4.15) cannot be extended to the energy independent diffusion case with $\sigma = 0$.

We used Talbot's method to calculate the spatially averaged downstream particle spectrum $F_{avg}(t,p)$ for energy dependent diffusion. Here, we are particularly interested in two cases: Bohm-like diffusion with $\sigma = 1$, and $\sigma = 0.5$, which is consistent with observations of Galactic CR (e.g., Berezinskii et al. 1990). The resulting particle spectra for the two cases are shown in Figs. 4.3(a) and 4.3(b), respectively, for various time ratios at $p = 1$ GeV/c. In both spectra there is a critical momentum below which the spectrum reaches the steady-state solution as in the energy independent diffusion case, while above the critical momentum, the particle spectrum gradually hardens by a $\sigma/2$ power of momentum compared to the input CR spectrum. This is because above the critical momentum, $\Theta(p) = t/\tau(p)$ becomes much smaller than 1 and the particle motion is dominated by the diffusion process. When diffusion dominates, the length scale for particle motion $L_{diff} \sim \sqrt{6\kappa t} \propto p^{\sigma/2}$. As a result, over a certain time interval t, high energy particles moving into the downstream region can trace back to a region further away in the preshock medium, which hardens the spectrum by a $\sigma/2$ power.

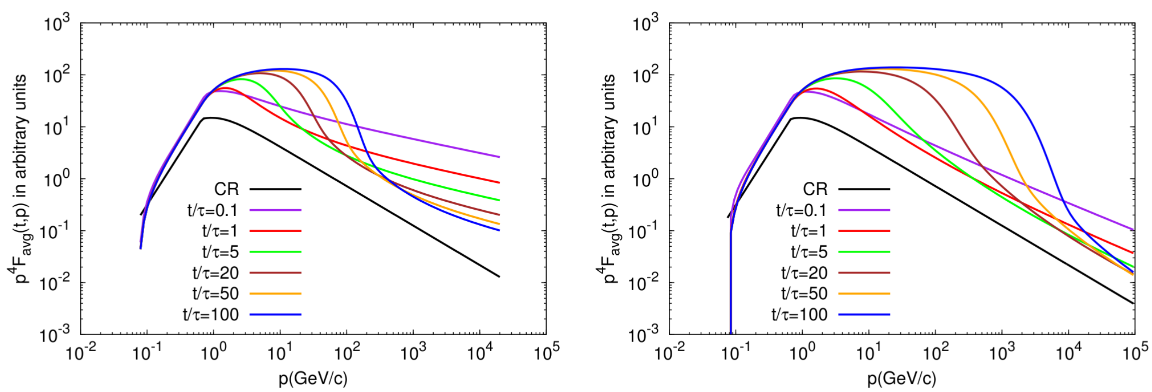

(a) (b)

Fig. 4.3.— Time evolution of the spatially averaged downstream particle momentum spectrum. The cosmic ray spectrum denoted by CR has arbitrary scaling. (a) Bohm-like diffusion with diffusion coefficient $\kappa \propto p$; (b) diffusion coefficient $\kappa \propto p^{0.5}$.

In Tang & Chevalier (2014), we found that the observed γ-ray emission from middle-aged SNRs like IC 443, W28 and W51C implies an accelerated particle spectrum that is similar in shape to the pre-existing CR spectrum at high energy. In the above discussion, we have shown that the time-dependent DSA solution in the test particle limit naturally produces an accelerated particle spectrum similar to the input CR spectrum at high energy when Θ is not large. The resulting particle spectrum follows the steady-state solution at low energy, but at high energy the particle spectrum is determined by both the input CR spectrum and the possible energy dependent diffusion. In the energy independent diffusion case, the spectrum simply recovers the steep power law shape of the input CR spectrum when approaching high energy, while for energy dependent diffusion the power law shape of the input CR spectrum gradually hardens by a $\sigma/2$ power at high energy.

4.3 Pion-decay emission

Assuming the γ-ray emission from those middle-aged SNRs interacting with molecular clouds has a hadronic origin (e.g., Ackermann et al. 2013), here we estimate the π^0-decay emission from IC 443 and W44 based on our time-dependent DSA solution and then compare the emission with observations. We take the model in Tang & Chevalier (2014) for molecular clump interaction, which is simplified from the following picture in Chevalier (1999): the remnant becomes radiative in the interclump medium of the molecular cloud, forming a cool shell, and the shell collides with dense molecular clumps, producing a layer of shocked shell (layer 1) and a layer of shocked molecular clump (layer 2). The radiative shell, layer 1 and layer 2 are all potential sources of γ-ray emission. According to the calculations in Tang & Chevalier (2014), emission from layer 2 is much smaller than the other two components, so in the following discussion we only model the π^0-decay emission from the radiative shell and layer 1.

Considering an emission region of volume V with uniformly distributed ambient protons of number density n_a and accelerated CR protons of number density n_{acc}, the resulting π^0-decay luminosity from the system is

$$L_{\pi^0}(E_\gamma, t) = \chi E_\gamma c \int_{E_{p,thresh}}^{\infty} dE_p \beta_p \frac{d\sigma(E_\gamma, E_p)}{dE_\gamma} n_a(t) n_{acc}(t, E_p) V, \tag{4.16}$$

where E_p is the CR proton energy, E_γ is the emitted photon energy, t is the age of the system, $d\sigma(E_\gamma, E_p)/dE_\gamma$ is the π^0-decay cross section, and χ is the scaling factor for helium and heavy nuclei which is taken to be 1.8 (Mori 2009). For this estimate, we ignore the dynamic evolution of the remnant and the accompanying particle loss through escape and energy loss through radiative cooling. CR particles are accelerated through both DSA and adiabatic compression. For seed particles with number density n_{seed}, we define the number density of CR that undergoes DSA for a time interval of t as $n_{DSA}(t, p, n_{seed}) = 4\pi p^2 F_{avg}(t, p)$. Then the accelerated CR spectrum with both DSA and adiabatic compression becomes

$$n_{acc}(t, E_p) = \frac{n_{acc}(t, p)}{v(p)} = \frac{(\lambda/4)^{2/3} n_{DSA}(t, (\lambda/4)^{-1/3} p, n_{seed})}{v(p)}, \tag{4.17}$$

where $v(p)$ is the particle velocity and λ is the total compression ratio for the emission region.

For the radiative shell, t equals the age of the remnant t_{age}, $n_a(t_{age})$ equals the shell density $n_s(t_{age})$, the seed particles are the pre-existing CRs which are taken to be the same as n_{GCR} in Tang & Chevalier (2014), and the emission volume is $V \approx 4\pi R(t_{age})^3\ (1 - w)/3\lambda_s$, where $R(t_{age})$ is the remnant radius, $\lambda_s = n_s/n_0$ is the shell compression ratio, and w is the volume filling factor for molecular clump interaction. The resulting accelerated CR number density in the shell then becomes

$$n_{acc,\,s}(t_{age}, E_p) = \frac{n_{acc,\,s}(t_{age}, p)}{v(p)} = \frac{(\lambda_s/4)^{2/3} n_{DSA,\,s}(t_{age}, (\lambda_s/4)^{-1/3} p, n_{GCR})}{v(p)}. \tag{4.18}$$

For layer 1, $t = t_{MC}$ which is the time since molecular clump interaction started and is taken to be the time that layer 1 is about to break out of the shell (see details in Tang & Chevalier 2014), $n_a(t_{MC})$ becomes the density of layer 1, $n_{l_1}(t_{MC})$, and the emission volume $V \approx 4\pi R(t_{age})^3 w/3\lambda_s\lambda_{l_1}$, where $\lambda_{l_1} = n_{l_1}/n_s$ is the layer 1 compression ratio. The number density of seed particles now becomes $n_{acc,\,s}$ and the resulting accelerated CR number density in layer 1 is

$$n_{acc,\,l_1}(t_{MC}, E_p) = \frac{n_{acc,\,l_1}(t_{MC}, p)}{v(p)} = \frac{(\lambda_{l_1}/4)^{2/3} n_{DSA,\,l_1}(t_{MC}, (\lambda_{l_1}/4)^{-1/3}p, n_{acc,\,s})}{v(p)}. \tag{4.19}$$

Pre-existing CRs in the ambient medium undergo two periods of DSA in reaching layer 1, so the resulting accelerated CR spectrum in layer 1 is determined by two time ratios Θ_f and Θ_{l_1}, which correspond to the SNR forward shock and the layer 1 shock, respectively. Due to the two DSA episodes, the resulting CR spectrum for energy dependent diffusion is hardened by one σ power instead of $\sigma/2$ power at high energy. The time-dependent DSA solution we derived here is under the assumption that there are seed particles uniformly distributed in the preshock medium extending to infinity. This is a good assumption for the SNR forward shock but, for the layer 1 shock sweeping up the radiative shell material, it breaks down especially when layer 1 is about to break out of the shell. Here we use the time-dependent solution for both the SNR forward shock and the layer 1 shock for simplicity. We expect the hardening at high energy will be less significant if the seed particles are only distributed in a limited size region of preshock medium.

Following the procedure in Kamae et al. (2006), we calculate the π^0-decay emission from IC 443 and W44, and then use the results as examples to show that simple estimates based on time-dependent DSA and π^0-decay emission can reproduce the γ-ray emission with the observed overall spectral shape. Combining the observational data and the molecular interaction model in Tang & Chevalier (2014) we can obtain the parameters for the SNR and the molecular interaction region, leaving only three variables in our spectrum fitting: the remnant forward shock time ratio Θ_f, the layer

1 shock time ratio Θ_{l_1}, and the volume filling factor w. The time ratios Θ_f and Θ_{l_1} obtained through spectrum fitting can be further used to estimate the diffusion coefficient of CR particles around the remnant and the molecular interaction region. By definition $\Theta_f = t_{age}U_f^2/4\kappa_0$, where U_f is the forward shock velocity and κ_0 is the diffusion coefficient in the upstream region of the forward shock, while $\Theta_{l_1} = t_{MC}(U_f - U_{l_1})^2/4\kappa_s$, where U_{l_1} is the layer 1 shock velocity and κ_s is the diffusion coefficient in the upstream region of the layer 1 shock. For typical parameters in middle-aged SNRs and the molecular interaction region, we find

$$\Theta_f \approx 8\left(\frac{t_{age}}{10^4 \text{ yrs}}\right)\left(\frac{U_f}{100\,\mathrm{km\,s^{-1}}}\right)^2\left(\frac{10^{24}\text{ cm}^2\text{ s}^{-1}}{\overline{\kappa_0}}\right)\left(\frac{1\text{ GeV/c}}{p}\right)^\sigma \tag{4.20}$$

and

$$\Theta_{l_1} \approx 0.08\left(\frac{t_{MC}}{100 \text{ yrs}}\right)\left(\frac{U_f - U_{l_1}}{100\,\mathrm{km\,s^{-1}}}\right)^2\left(\frac{10^{24}\text{ cm}^2\text{ s}^{-1}}{\overline{\kappa_s}}\right)\left(\frac{1\text{ GeV/c}}{p}\right)^\sigma \tag{4.21}$$

under the assumption that $\kappa = \overline{\kappa}\,\overline{p}^\sigma$. $\overline{\kappa_0}$ and $\overline{\kappa_s}$ are unknown parameters depending on the shock environment, especially the surrounding magnetic irregularities, and may be related to each other. For example, in the special case of Bohm-like diffusion, $\overline{\kappa} = \eta pc^2/3eB$ where $\eta > 1$ is the gyro-factor. If we assume η is constant within the SNR and molecular interaction region, then $\overline{\kappa_0}/\overline{\kappa_s} = B_s/B_0$, where B_0 is the magnetic field in the ambient medium and B_s is the magnetic field in the radiative shell. As a result, $\Theta_f/\Theta_{l_1} = t_{age}U_f^2B_0/t_{MC}(U_f - U_{l_1})^2B_s \approx 1$ for both IC 443 and W44 with our parameters. For energy dependent diffusion with arbitrary power law index σ, there is no theory for the ratio Θ_f/Θ_{l_1}, so we leave Θ_f and Θ_{l_1} as two independent parameters for our fits. We do require that the ratio Θ_f/Θ_{l_1} fall between the value from Bohm-like diffusion and the value from assuming $\overline{\kappa_0} = \overline{\kappa_s}$. In fitting the spectrum, we allow for three different situations: energy independent diffusion with $\sigma = 0$, Bohm-like diffusion with $\sigma = 1$, and energy dependent diffusion with $\sigma = 0.5$. For Bohm-like diffusion we apply the relation $\Theta_f = \Theta_{l_1}$, as discussed above, while for the other two cases we require $1 \lesssim \Theta_f/\Theta_{l_1} \lesssim t_{age}U_f^2/t_{MC}(U_f - U_{l_1})^2$. In the above calculation, we ignore the dynamical evolution of the SNR and assume $U_f(t) = U_f(t_{age})$. This might affect our estimate of $\overline{\kappa_0}$, but our result can at least provide order of magnitude information on the diffusion coefficient because U_f has a weak dependence on time. In our spectral modeling, we have not attempted to obtain a best fit in view of the complex physical situation and model uncertainties, but aim to show the importance of the time-dependent DSA solution in improving the fit to the spectrum. Self-consistent models or simulations with time-dependent DSA coupled with the dynamical evolution of the SNR are required in the future for detailed comparisons with observations.

For IC 443, we use parameters from Table 1 in Tang & Chevalier (2014) for the remnant and molecular interaction region. In the energy independent diffusion case, we show an example fit with $\Theta_f = 2\Theta_{l_1} = 2$ at $p = 1$ GeV/c and a filling factor $w = 0.2$ (Fig. 4.4(a)). The resulting spectrum is similar to the pure adiabatic compression case in Tang & Chevalier (2014), since DSA with energy independent diffusion can reproduce the input CR spectrum at small Θ. In the energy independent diffusion case, the spectral shape is mainly determined by Θ_f and is not very sensitive to Θ_{l_1}, which is coupled with w. For Bohm-like diffusion with $\sigma = 1$ and assuming $\Theta_f \approx \Theta_{l_1}$, we can roughly fit the observed γ-ray emission with $\Theta_f = \Theta_{l_1} = 40$ at $p = 1$ GeV/c and $w = 0.06$ (Fig 4.4(b)). The spectral hardening at high energy produces too flat a spectrum compared to observations, which implies that Bohm-like diffusion is probably not a good assumption for these middle-aged SNRs in the context

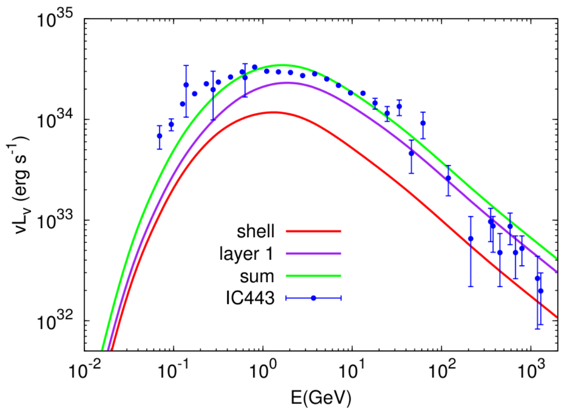

(a)

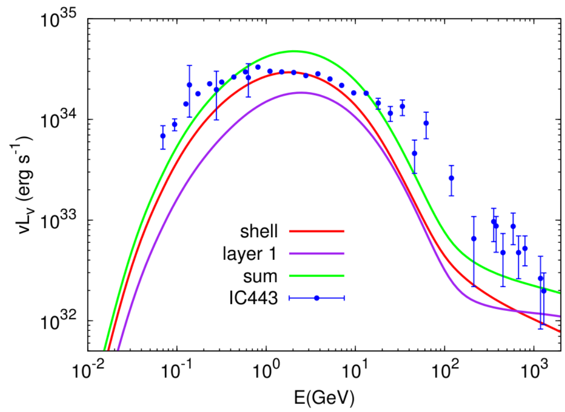

(b)

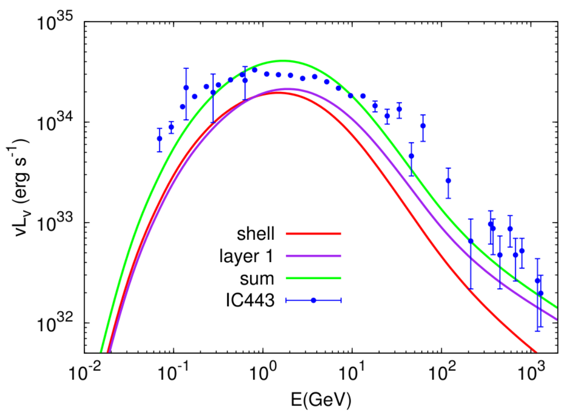

(c)

Fig. 4.4.— π^0-decay emission from IC 443 for different energy dependence of diffusion coefficient. Shell is the radiative shell of remnant, layer 1 is the shocked shell, and sum is the sum of the 2 components. (a) Energy independent diffusion with $\Theta_f = 2\Theta_{l_1} = 2$ at $p = 1$ GeV/c and $w = 0.2$ compared to observations; (b) energy dependent diffusion with $\kappa \propto p$, $\Theta_f = \Theta_{l_1} = 40$ at $p = 1$ GeV/c and $w = 0.06$; (c) energy dependent diffusion with $\kappa \propto p^{0.5}$, $\Theta_f = 16\Theta_{l_1} = 8$ at $p = 1$ GeV/c and $w = 0.15$. The data points are taken from the same references as in Tang & Chevalier (2014).

of our model. For $\sigma = 0.5$, an example fit with $\Theta_f = 16\Theta_{l_1} = 8$ at $p = 1$ GeV/c and $w = 0.15$ is presented in Fig 4.4(c). The π^0-decay emission due to energy dependent diffusion is characterized by a hardening at high energy compared to the energy independent diffusion case. For IC 443 the hardening is likely to be around 100 GeV according to our fit. The significance of the hardening is simply determined by σ. It is clear that energy dependent diffusion with $\sigma = 0.5$ fits the observations better than Bohm-like diffusion. This is comparable to the σ value inferred for Galactic CR (Berezinskii et al. 1990). With the values of Θ_f and Θ_{l_1} obtained above, we can estimate the diffusion coefficient of CR particles around the SNR and the molecular interaction region. We only discuss the CR diffusion coefficient around the remnant forward shock because t_{MC} for the molecular interaction is uncertain, although we assume t_{MC} equals the break out time to simplify the calculation. The calculated values of $\overline{\kappa_0}$ for $\sigma = 0$, $\sigma = 0.5$, and $\sigma = 1$ at $p = 1$ GeV/c are 9×10^{24} cm^2 s^{-1}, 2×10^{24} cm^2 s^{-1}, and 4×10^{23} cm^2 s^{-1} respectively, which are much smaller than the CR diffusion coefficient at $p = 1$GeV/c in the ISM, $\sim 3 \times 10^{27}$ cm^2 s^{-1} (Berezinskii et al. 1990), but are closer to the Bohm limit at $p = 1$ GeV/c, $\sim 7 \times 10^{21}$ cm^2 s^{-1}. According to the discussion in Section 2, for the SNR forward shock our simplified model parameter $\tau = \tau_1 = \tau_2 \approx \hat{\tau}_1$ reflects the value of the spatially averaged diffusion coefficient in the upstream region. The CR diffusion coefficient close to the shock front should be lower than the estimated $\overline{\kappa_0}$ above and close to the Bohm limit.

W44 (G34.7 - 0.4) is a mixed morphology SNR with centrally filled X-ray emission and shell-like radio emission. The distance to the remnant is estimated to be $\sim$ 3 kpc based on both HI 21cm absorption measurements (Caswell et al. 1975) and molecular observations (Castelletti et al. 2007). Wolszczan et al. (1991) discovered a 267 msec pulsar, PSR 1853 + 01, in the southern part of W44 well within its radio shell. The pulsar has a spin down age $\sim 2 \times 10^4$ years and a dispersion measure distance consistent with the remnant distance, which implies the pulsar is likely to be associated with the W44. The remnant is elongated with a size of 11×15 pc at a distance of 3 kpc, so we take 13 pc for the remnant radius as in Chevalier (1999). The forward shock velocity is taken to be $150\,\mathrm{km\,s^{-1}}$ since Koo & Heiles (1995) found an expanding HI shell moving at velocity of $150\,\mathrm{km\,s^{-1}}$, which may be the expanding cool shell formed in the radiative phase. Millimeter wavelength observations of CO and CS lines indicate a molecular shock velocity of $20-30\,\mathrm{km\,s^{-1}}$ (Reach et al. 2005), so we take a molecular clump shock velocity U_c of $30\,\mathrm{km\,s^{-1}}$ in our calculation. The preshock magnetic field is taken to be 6 μG, similar to Tang & Chevalier (2014). W44 has a γ-ray luminosity about one order of magnitude higher than IC 443. In order to obtain such a high γ-ray luminosity we require a larger SN explosion energy, $\sim 3 \times 10^{51}$ erg. The other parameters for the remnant and the molecular interaction region can be obtained from the radiative SNR model in Cioffi et al. (1988) and the molecular clump interaction model in Tang & Chevalier (2014), respectively. The parameters we use for W44 are listed in Table 4.1.

W44 has a steeper γ-ray spectrum than IC 443 in the GeV range (Ackermann et al. 2013), while in the TeV range there are only upper limits so far (Buckley et al. 1998; Aharonian et al. 2002; Ong et al. 2009). The steep spectrum above 1 GeV makes it difficult to fit the W44 data with an energy independent diffusion model as it reproduces the pre-existing CR spectrum at high energy which has a shallower shape. We focus our attention on the energy dependent diffusion cases. Bohm-like diffusion with $\sigma = 1$ produces too flat a spectrum at high energy which is also disfavored by the data, so for W44 we only show the result for $\sigma = 0.5$. An example fit with $\Theta_f = 3\Theta_{l_1} = 3$ at $p = 1$ GeV/c and $w = 0.3$ is shown in Fig. 4.5. The corresponding

Table 4.1: Basic parameters for the W44 model

SNR dynamics	
Explosion energy, E	3×10^{51} erg
Age, t_{age}	27 kyr
SNR radius, R	13 pc
Remnant forward shock velocity, U_f	150 km/s
Shock compression ratio, Ω_s	4
Molecular clump and interclump medium(ICM)	
Preshock ICM density, n_0	10.3 cm^{-3}
Magnetic field in ICM, B_0	6 μG
Molecular clump density, n_c	1.4×10^4 cm^{-3}
Magnetic field in molecular clump, B_c	71 μG
Radiative shell and molecular clump interaction region	
Discontinuity velocity of clump shock, U_c	30 km/s
Molecular clump interaction break out time, t_{MC}	0.3 kyr
Density in the radiative shell at t_{age}, n_s	6.6×10^2 cm^{-3}
Magnetic field in the radiative shell at t_{age}, B_{ts}	3.7×10^2 μG
Density in layer 1, n_{l_1}	4.9×10^3 cm^{-3}
Magnetic field in layer 1, B_{t1}	2.7×10^3 μG
Layer 1 velocity, U_{l_1}	11 km/s
Shock compression ratio for layer 1, Ω_{l_1}	3.5
Density in layer 2, n_{l_2}	6.4×10^5 cm^{-3}
Magnetic field in layer 2, B_{t2}	2.7×10^3 μG
Layer 2 velocity, U_{l_2}	31 km/s

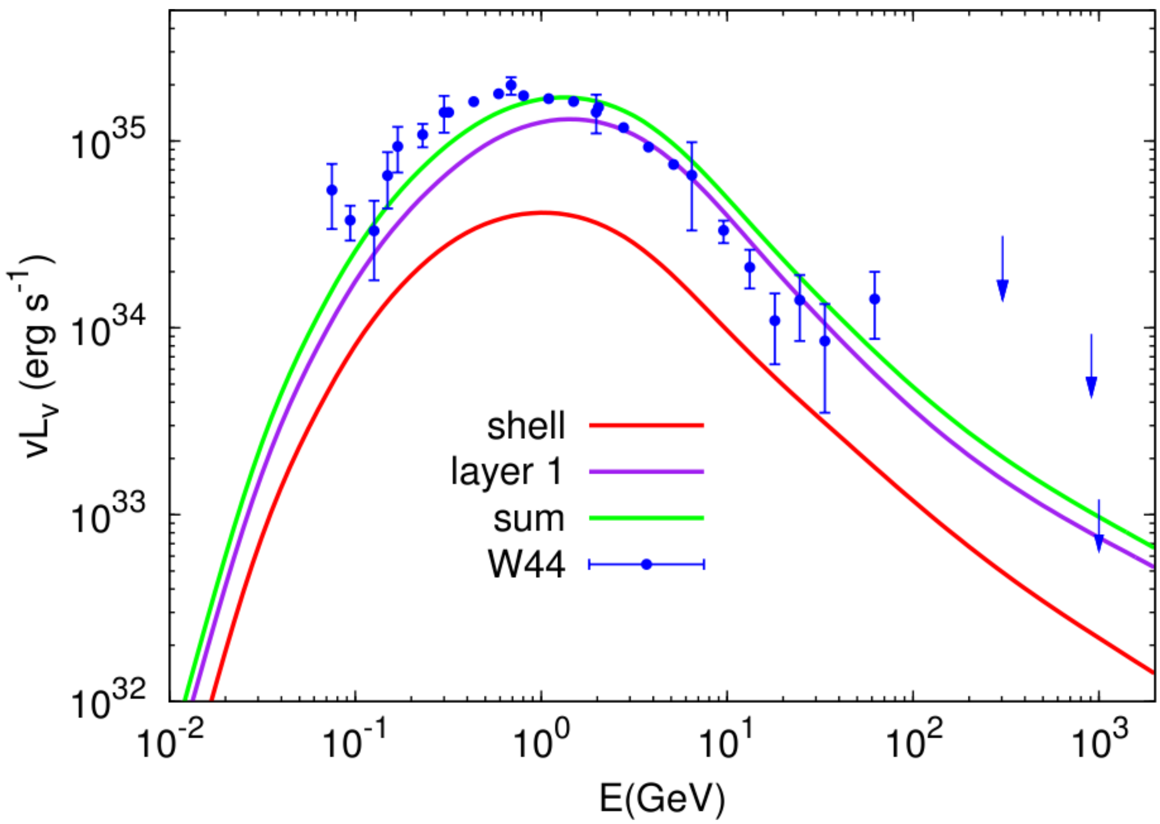

Fig. 4.5.— Like Fig. 4.4 but for the W44 remnant and models with $\kappa \propto p^{0.5}$, $\Theta_f = \Theta_{l_1} = 3$ at $p = 1$ GeV/c and $w = 0.3$. The data points are taken from Ackermann et al. (2013); Buckley et al. (1998); Aharonian et al. (2002); Ong et al. (2009)

$\overline{\kappa_0} \approx 2 \times 10^{25}$ cm^{2}s^{-1} at $p = 1$ GeV/c is about one order of magnitude larger than that in IC 443 and is about 3000 times larger than the Bohm diffusion coefficient at $p = 1$ GeV/c. In the fit for W44, our TeV spectrum is close to the upper limit provided by VERITAS (Ong et al. 2009). However, there are factors that could reduce the emission in the TeV range. For the layer 1 shock the pre-existing CR are only distributed in a limited region, which could soften the spectrum at high energy. A smaller σ could also soften the spectrum at high energy.

4.4 Discussion

We have obtained a time-dependent DSA solution in the test particle limit for a planar parallel shock with pre-existing CRs in the preshock region. By combining the time-dependent DSA solution derived here and the molecular clump interaction model in Tang & Chevalier (2014), we can produce π^0-decay emission that compares well to observations. The derived time ratio Θ_f can be further used to estimate the diffusion coefficient of CR particles around the SNR, but the estimated diffusion coefficient should be considered as a spatially averaged value and be taken as an upper limit for the diffusion coefficient near the shock front. We discussed three situations for our time-dependent DSA solution: energy independent diffusion, Bohm-like diffusion with energy index $\sigma = 1$, and energy dependent diffusion with $\sigma = 0.5$. For both IC 443 and W44, the best fit is with energy dependent diffusion with $\sigma = 0.5$, which is roughly consistent with Galactic CR observations. The resulting time-dependent DSA spectrum is characterized by a critical energy below which the spectrum reaches the steady-state solution while above it the spectrum recovers the steep power law shape of the pre-existing CR spectrum with possible hardening due to energy dependent diffusion. Based on the above spectral shape we expect the γ-ray emission from these middle-aged SNRs interacting with molecular clouds to show a spectral hardening in the TeV range which might be detectable by future advanced instruments. If observed, the hardening could be used to derive information about CR diffusion around the SNR shock.

Malkov et al. (2011) have shown that the steep spectrum of W44 can be explained if accelerated particles can escape from the shock region due to the ion neutral damping mechanism, which steepens the spectrum by exactly one power. Under the assumption of the test particle limit, the high shock velocity, $\gtrsim 120\,\mathrm{km\,s^{-1}}$, in W44 is inconsistent with the weakly ionized preshock medium required for ion neutral damping (Hollenbach & McKee 1989). But if non-linear effects are strong, efficient CR acceleration and escape could modify the shock structure and allow ion neutral damping in W44 (Bykov et al. 2013). A self-consistent model with DSA coupled to the SNR evolution is needed in the future to fully understand the role of ion neutral damping in W44.

Here, we did not take escape of CR particles into account because it may not be important for the energy range of interest. There have been simulations using CR escape to explain the γ-ray emission from the middle-aged SNRs discussed here (e.g., Ohira et al. 2011), but these models require that accelerated CR particles with energies down to ~ 1 GeV escape from the remnant and illuminate the nearby dense clump. This assumption needs more detailed investigation. Here we use Bohm diffusion as an example, because the diffusion coefficients we estimated are close to the Bohm diffusion limit and there is also observational evidence indicating possible Bohm diffusion in young SNR (e.g., Uchiyama et al. 2007). Following the discussion in Ohira et al. (2011), the critical momentum for CR particles that can escape the remnant satisfies $p_{esc} = \kappa D_0^{-1} R_{sh} u_{sh}$ (eq. (17) in Ohira et al. (2011); see the definitions there for the parameters in the formula). Assuming that SNRs are the CR accelerators up to the energy of CR knee $\sim 10^{15}$ eV i.e. $p_{esc}(t_{Sedov}) \sim 10^{15}$ eV/c, where t_{Sedov} is the transition time from the free expansion phase to the Sedov-Taylor phase, then the critical momentum for escaping CR particles at t_{age} now becomes $p_{esc}(t_{age}) = p_{esc}(t_{Sedov})R_{sh}(t_{age})u_{sh}(t_{age})D_0(t_{Sedov})/D_0(t_{age})R_{sh}(t_{Sedov})u_{sh}(t_{Sedov})$. The escape models developed so far focus on the Sedov-Taylor phase of the SNR in which $R_{sh} \propto t^{2/5}$ and $u_{sh} \propto t^{-3/5}$. In such a situation,

$$p_{esc}(t_{age}) = p_{esc}(t_{Sedov}) \left(\frac{t_{age}}{t_{Sedov}}\right)^{-1/5} \frac{B_{t_{age}}}{B_{t_{Sedov}}}. \tag{4.22}$$

As a result, for the evolution of a middle-aged SNR from $t_{Sedov} \sim 100$ yrs to $t_{age} \sim 10^4$ yrs and a magnetic field amplification factor of $B_{t_{Sedov}}/B_{t_{age}} \sim 100$, the critical momentum of escaping CR particles right now is $t_{age} \approx 4\times10^{12}$ eV/c, above the energy range discussed here. The escaping CR particles which reach the nearby dense clumps and illuminate them would have even higher energy. Obtaining $p_{esc}(t_{age}) \sim 1$ GeV/c requires extreme conditions for parameters like the magnetic field amplification factor, or the diffusion coefficient of CR particles must have a weak dependence on particle momentum and relatively strong dependence on magnetic field, which is not clear from observations.

In our model we assume a parallel shock for simplicity, but in reality the magnetic field in the ambient medium is likely to be randomly distributed while the molecular shock is likely to be a perpendicular shock due to a magnetically supported shell. For an oblique shock with angle ϕ between the magnetic field direction and the shock normal, the diffusion coefficient $\kappa = \kappa_{||}\cos^2\phi + \kappa_{\perp}\sin^2\phi$ where $\kappa_{||}$ is the diffusion coefficient along the magnetic field lines and $\kappa_{\perp}$ is the diffusion coefficient across the field lines (e.g., Reynolds 1998). In general, if we take the obliquity of the shock into account it would affect our estimate of the CR diffusion coefficient depending on the angle ϕ and the relation between $\kappa_{||}$ and $\kappa_{\perp}$, but it does not affect the time ratios Θ_f and Θ_{l_1} derived in the fits to spectra.

In our molecular clump interaction model we only consider the situation that layer 1 has not broken out of the radiative shell. In reality, layer 1 could break out of the radiative shell after a sufficient time of interaction. In that case the emission from layer 2 might become dominant. Unlike the shocked shell matter in layer 1, the shocked clump matter accumulated in layer 2 only undergoes one episode of DSA, which produces a spectrum with less hardening, by $\sigma/2$ at high energy compared to layer 1. As a result, when layer 2 dominates the γ-ray emission, the Bohm-like diffusion case would produce a steeper spectrum and fit the observations better. Anderl et al. (2014) found evidence for non-stationary shocks in W44 with age $\sim 10^3$ yrs through a radiation transfer model of the CO(7-6) and CO(6-5) transitions. The ages suggest that in W44 layer 1 may already have broken out of the radiative shell.

In our spectral fits for both IC 443 and W44, the γ-ray emission from layer 1 is either comparable to or larger than the emission from the shell component. Considering the small filling factor w in the fit, emission from layer 1 would have a larger γ-ray surface brightness than the shell. After projection effects, the shell is expected to show a ring-like or filamentary structure in γ-rays while the morphology for molecular interaction region could be complex. Instead of interacting with one single large clump, the remnant is likely to be interacting with multiple clumps at the same time. The γ-ray morphology of the molecular interaction region is also determined by the angle between the molecular shock normal and the viewing angle direction. If the shock normal is perpendicular to the line of sight, we would expect γ-ray morphology with a ring or arc-like feature plus some bright spots on the edge of the ring. If the molecular shock normal is more or less along the line of sight, we might observe a roughly uniform disk-like morphology or center bright morphology with multi-clump interaction. In order to disentangle all the different situations we require more detailed observations of the molecular interaction region.

Finally, we note that the time-dependent DSA model presented here should also be applicable to other interaction models with re-acceleration of pre-existing CR in the preshock medium (e.g., Uchiyama et al. 2010).

Acknowledgements

We thank A. Bykov for comments of the paper. This research was supported in part by NASA *Fermi* grant NNX12AE51G.

4.5 Appendix

In order to elucidate our results on the spectral shape, we need to understand the micro-physics of the DSA process. In DSA, particles are bouncing back and forth across and around the shock discontinuity as a result of the magnetic turbulence. Every time a particle comes across the shock discontinuity it receives a mean momentum gain $\Delta p = 2(U_1 - U_2)p/3v$, where v is the particle velocity, and the mean time taken for a particle to complete one cycle of back and forth motion is $\Delta t = 4\left(\kappa_1/U_1 + \kappa_2/U_2\right)/v$ (Drury 1983). The corresponding momentum gain rate for a particle undergoing DSA is then

$$\frac{dp}{dt} = \frac{2\Delta p}{\Delta t} = \frac{U_1 - U_2}{3}\left(\frac{\kappa_1}{U_1} + \frac{\kappa_2}{U_2}\right)^{-1} p. \tag{4.23}$$

Particles entering the downstream region have a chance to escape the DSA site and move to $+\infty$ in the downstream region due to the advective flow towards the positive

x direction. The probability for a particle not returning back to the acceleration site is given by $\Gamma = 4U_2/v$ (Drury 1983). Considering a particle with initial momentum p_i, after n cycles of acceleration the particle momentum becomes

$$p_n \sim \prod_{k=1}^{n} \left[1 + \frac{4(U_1 - U_2)}{3v_k}\right] p_i, \tag{4.24}$$

leading to

$$\ln(p_n/p_i) \sim \frac{4(U_1 - U_2)}{3} \sum_{k=1}^{n} \frac{1}{v_k}. \tag{4.25}$$

The probability for a particle to stay at the acceleration site after n cycles of back and forth motion is

$$\Gamma_n \sim \prod_{k=1}^{n} \left(1 - \frac{4U_2}{v_k}\right) \tag{4.26}$$

so that

$$\begin{aligned} \ln\Gamma_n &\sim -4U_2 \sum_{k=1}^{n} \frac{1}{v_k} && (4.27) \\ &= -\frac{3U_2}{U_1 - U_2} \ln(p_n/p_i). && (4.28) \end{aligned}$$

After a time $t = n\Delta t$, the particle momentum changes from p_i to p_n. For constant U and κ, the energy gain rate $dp/dt \propto p$ which implies that the time taken for a particle to increase its momentum by an arbitrary factor is the same for all particle momenta. The energy gain during DSA simply shifts the input spectrum in the momentum direction by a factor of p_n/p_i. Based on the conservation of particle number, the new particle spectrum $R_n(p_n)$ is related to the input CR spectrum $R(p_i)$ by

$$R_n(p_n)dp_n = R(p_i)\Gamma_n dp_i, \tag{4.29}$$

where Γ_n is the probability for a particle to stay at the DSA site after a time $t = n\Delta t$. For a strong shock, $\Gamma_n = p_i/p_n$ [equation (4.28)] and, based on our energy gain rate, we have $dp_n/dp_i = p_n/p_i$. After some calculation we obtain $R_n(p_n)p_n^2 = R(p_i)p_i^2$. As the particle number density $R(p)$ and the phase space density $f(p)$ are related by $R(p) = 4\pi f(p)p^2$, we obtain the relation $f_n(p_n)p_n^4 = f(p_i)p_i^4$ for the downstream particle spectrum at the shock front, which indicates that in the $\log(f(p)p^4) - \log(p)$ plane, the whole DSA process works like a horizontal shift of the function $f(p)p^4$. The amount of shift is determined by

$$\ln\left(\frac{p_n}{p_i}\right) = \frac{U_1 - U_2}{3}\left(\frac{\kappa_1}{U_1} + \frac{\kappa_2}{U_2}\right)^{-1} t, \tag{4.30}$$

so that p_n/p_i depends on time t exponentially. As a result, the accumulated CR particle spectrum at the shock front after time t is determined by the sum of the input CR spectrum shifted by various amounts along the $\log(p)$ axis due to various injection times in the $\log(f(p)p^4) - \log(p)$ plane. Because of the exponential dependence on time t, in the $\log(f(p)p^4) - \log(p)$ plane all the shifted spectra have the same weight for the sum.

Based on the shape of the input CR spectrum which follows roughly a broken power law, the accumulated downstream particle spectrum at the shock front would have three parts according to above discussion. The low energy and high energy parts of the accumulated particle spectrum maintain the two power law shape of the input CR spectrum because all the shifted spectra share the same power law index. At intermediate energies, the accumulated particle spectrum shows a plateau which is due to the break in the input CR spectrum. The plateau starts at the break momentum p_b of the input CR spectrum and ends at the momentum p_t, which is determined by equation (4.30). p_t serves as a critical momentum for the accumulated downstream particle spectrum at the shock front; below p_t the resulting spectrum follows the steady state DSA solution while above p_t the spectrum recovers the steep power law shape of the input CR spectrum at high energy. Our discussion here only provides the overall shape of the accumulated particle spectrum roughly as all the calculations are based on the mean acceleration time and energy gain

Chapter 5

Future Work

Thanks to the new generation of TeV observatories (e.g., HESS and MAGIC), a large population of very high energy (VHE) sources have been revealed in the last decade. PWNe are observed to dominate the identified VHE sources, making them important sources of leptonic CRs (Kargaltsev et al. 2013). In addition, there are still many unidentified VHE sources, some of which have neither radio nor X-ray counterparts. I would like to investigate two possible explanations of these dark VHE sources, based on the topics discussed in this thesis. One explanation is that MCs are illuminated by CRs escaping from a SNR, and the other is old PWNe with low energy relic counterparts that are too faint to be detected.

In Chapters 3 and 4, I presented a model for γ-ray emission from middle-aged SNRs interacting with MCs. The next step would be to investigate the multi-wavelegth emission. Accelerated electrons within the SNR can produce synchrotron emission in the radio band, providing another important window for understanding CR acceleration in SNRs. Recent Planck data (Plank Collaboration et al. 2014) shows a possible break at high frequency in SNRs (e.g., W44 and IC 443), which is worth further study.

The picture presented in this thesis for middle-aged SNRs interacting with MCs is different from the previous one proposed in Uchiyama et al. (2010). In our model, we consider a remnant that is in the radiative phase, while a non-radiative SNR is assumed in Uchiyama et al. (2010). In our case, both the radiative shell and MC interaction regions contribute to the γ-ray emission while the MC interaction regions dominate the hadronic emission. The radio emission is not necessarily spatially correlated with the γ-ray emission region, as it is dominated by emission from the radiative shell. IC 443 seems to be a good example for our case. In our picture, we expect to observe faint γ-ray emission from the dense shell of a radiative SNR, even if it is not interacting with MCs. The γ-ray and radio emission are likely spatially correlated with each other for SNRs not interacting with MCs, since they both originate from the dense shell. S147 is probably a remnant falling into this category, as it shows no signature of MC interaction and has a much lower γ-ray luminosity than those remnants interacting with MCs. In addition, the γ-ray emission region is spatially correlated with the radio and optically bright regions. The radio and γ-ray emission from S147 has been studied by Katsuta et al. (2012) under the picture of Uchiyama et al. (2010), but they required a very small filling factor that appears to be inconsistent with observations. I am currently working on a project to explain the γ-ray and radio emission from SNR S147 with the picture described in this thesis.

In the theory of DSA, energetic seed particles are injected into the acceleration process, through a still not fully understood mechanism, to initiate and maintain the DSA process. The energetic seed particles can either be extracted from the shock-heated thermal particles in the downstream region, or they can come from a pre-existing population of energetic particles in the upstream region. In young SNR, it is usually assumed that energetic particles in the high energy tail of the thermal population in the postshock region act as the seed particles. Young remnants have fast shocks that can heat the swept-up particles to higher energies. However, for the middle-aged SNRs discussed in this thesis (with slow shocks) we assumed that the seed particles are pre-existing CRs in the ambient medium, and we found that re-acceleration of pre-existing CRs can reproduce the observed hadronic like γ-ray emission. More solid evidence supporting the re-acceleration of pre-existing CRs in slow shocks comes from 1-dimensional hydrodynamic simulations with coupled CR acceleration in Lee et al. (2015). Radio and γ-ray emission are calculated for both cases of seed particles. It was found that the re-acceleration of pre-existing CRs case can reproduce both the radio and γ-ray emission, while the thermal particle case can't. Moreover, the thermal particle case requires strong turbulence and large particle acceleration efficiency $> 30\%$ (defined to be the fraction of the shock kinetic energy used for CR acceleration), which is probably hard to achieve in the slow shocks. If the seed particles in old remnants are dominated by pre-existing CRs while shocked-heated thermal particles dominate the seed particles in young SNRs, it implies a transition in seed particles from the downstream thermal population to pre-existing CRs in the ambient medium as the remnant evolves. Then a few points we need to address include when the transition happens, what causes the transition and how the transition affects the evolution and emission of a SNR.

In Chapter 1, I presented our current understanding of SNR evolution in a uniform medium, without including magnetic fields or dynamical back-reaction due to CR acceleration, which is a very simplified situation. There are several factors which can potentially affect the dynamical evolution and emission of a SNR.

1. *Inhomogeneous ISM.* Multi-wavelength high resolution spectra and images reveal complex MC structures around middle-aged SNRs interacting with MCs (e.g.,

Slane et al. 2014), which implies that the surrounding medium is far from uniform. Some efforts have recently been made for SNR evolution in an inhomogeneous ISM with 3D hydrodynamic simulations (multi-phase ISM in Kim & Ostriker (2015) and turbulent-driven ISM in (Martizzi et al. 2014)). But they focused on the SN feedback into the ISM which is characterized by the amount of momentum injected into MCs by the SN explosion.

2. *Magnetic fields.* Magnetic fields are very important for CR acceleration in SNRs, as they determine the maximum attainable energy of CR particles in the SNR evolution. Magnetic fields are also crucial for the dynamical evolution of SNRs. For middle-aged SNRs, involving radiative shocks, the magnetic pressure in the radiative shell can dominate the thermal pressure (Chevalier 1999) and thus might affect the dynamical evolution of the remnant. Iffrig & Hennebelle (2014) performed 3D MHD simulations of SNR evolution with radiative cooling, but again focused on the SN feedback on the MCs. The dynamical evolution of SNRs under different environments however is not discussed.

3. *Coupling between CR acceleration and SNR evolution.* CR acceleration is coupled with SNR evolution, as the back-reaction of the accelerated CR particles can modify the shock structure. A self-consistent calculation with CR acceleration coupled to the SNR evolution is necessary to understand the broadband emission and the dynamical evolution of a SNR. With enhanced computational facilities and advanced observational instruments, we are now able to investigate how these factors change the evolution and emission of a SNR by comparing simulation results with multi-wavelength images and spectra.

The study of turbulence in MCs has recently attracted a lot of attention. A variety of observations, including non-thermal line broadening in molecular emission (e.g., Heyer & Brunt 2004) and hierarchical structures (e.g., Vazquez-Semadeni 1994), have revealed the existence of turbulence in MCs. In SNRs, the observed filamentary structures are believed to be induced by instabilities (e.g., Rayleigh-Taylor instability) triggered within the remnant. When turbulence is present in the surrounding medium, it will be interesting to investigate how the turbulence in the ambient medium affects the evolution and emission of the remnant, especially the filamentary structures. A more ambitious idea would be to use SNRs as a tool to probe the turbulence in the surrounding ISM.

Bibliography

Abdo, A. A., Ackermann, M., Ajello, M., et al. 2009, ApJ, 706, L1

Abdo, A. A., Ackermann, M., Ajello, M., et al. 2010a, Science, 327, 1103

Abdo, A. A., Ackermann, M., Ajello, M., et al. 2010b, ApJ, 712, 459

Abdo, A. A., Ackermann, M., Ajello, M., et al. 2010c, ApJ, 718, 348

Abraham, J., Abreu, P., Aglietta, M., et al. 2010, Physics Letters B, 685, 239

Acciari, V. A., Aliu, E., Arlen, T., et al. 2009, ApJ, 698, L133

Ackermann, M., Ajello, M., Allafort, A., et al. 2013, Science, 339, 807

Adriani, O., Barbarino, G. C., Bazilevskaya, G. A., et al. 2009, Nature, 458, 607

Adriani, O., Barbarino, G. C., Bazilevskaya, G. A., et al. 2011, Science, 332, 69

Aguilar, M., Alberti, G., Alpat, B., et al. 2013, Physical Review Letters, 110, 141102

Aharonian, F. A., Akhperjanian, A. G., Beilicke, M., et al. 2002, A&A, 395, 803

Aharonian, F., et al. 2004, ApJ, 614, 897

Aharonian, F., Akhperjanian, A. G., Bazer-Bachi, A. R., et al. 2008, A&A, 481, 401

Ahn, H. S., Allison, P., Bagliesi, M. G., et al. 2010, ApJ, 714, L89

Albert, J., Aliu, E., Anderhub, H., et al. 2007, ApJ, 664, L87

Aleksić, J., Alvarez, E. A., Antonelli, L. A., et al. 2012, A&A, 541, A13

Amato, E., Salvati, M., Bandiera, R., Pacini, F., & Woltjer, L. 2000, A&A, 359, 1107

Amato, E., & Arons, J. 2006, ApJ, 653, 325

Amato, E. 2014, International Journal of Modern Physics D, 23, 1430013

Anderl, S., Gusdorf, A., Güsten, R. 2014, A&A, accepted (arXiv:1407.8429)

Arendt, R. G., George, J. V., Staguhn, J. G., et al. 2011, ApJ, 734, 54

Baade, W., & Zwicky, F. 1934, Proceedings of the National Academy of Science, 20, 259

Baars, J. W. M., Genzel, R., Pauliny-Toth, I. I. K., & Witzel, A. 1977, A&A, 61, 99

Balsara, D., Benjamin, R. A., & Cox, D. P. 2001, ApJ, 563, 800

Bamba, A., Anada, T., Dotani, T., et al. 2010, ApJ, 719, L116

Begelman, M. C. 1998, ApJ, 493, 291

Bell, A. R. 1978, MNRAS, 182, 147

Berezhko, E. G. 2008, ApJ, 684, L69

Berezinskii, V. S., Bulanov, S. V., Dogiel, V. A., Ginzburg, V.L., & Ptuskin, V. S. 1990, Astrophysics of Cosmic Rays (Amsterdam: North-Holland)

Bietenholz, M. F. 2006, ApJ, 645, 1180

Bietenholz, M. F., Kassim, N., Frail, D. A., Perley, R. A., Erickson, W. C., & Hajian, A. R. 1997, ApJ, 490, 291

Bietenholz, M. F., Kassim, N. E., & Weiler, K. W. 2001, ApJ, 560, 772

Bietenholz, M. F., Hester, J. J., Frail, D. A., & Bartel, N. 2004, ApJ, 615, 794

Bietenholz, M. F., & Bartel, N. 2008, MNRAS, 386, 1411

Blandford, R. D., & Cowie, L. L. 1982, ApJ, 260, 625

Blandford, R., & Eichler, D. 1987, Phys. Rep., 154, 1

Blasi, P. 2013, A&A Rev., 21, 70

Blondin, J. M., Chevalier, R. A., & Frierson, D. M. 2001, ApJ, 563, 806

Bocchino, F., Warwick, R. S., Marty, P., Lumb, D., Becker, W., & Pigot, C. 2001, A&A, 369, 1078

Bocchino, F., van der Swaluw, E., Chevalier, R., & Bandiera, R. 2005, A&A, 442, 539

Brogan, C. L., Gelfand, J. D., Gaensler, B. M., Kassim, N. E., & Lazio, T. J. W. 2006, ApJ, 639, L25

Bucciantini, N., Amato, E., Bandiera, R., Blondin, J. M., & Del Zanna, L. 2004, A&A, 423, 253

Bucciantini, N. 2011, in High-Energy Emission from Pulsars and their Systems, ed. N. Rea & D. Torres (Berlin: Springer), 473 (arXiv:1005.4781)

Bucciantini, N., Arons, J., & Amato, E. 2011, MNRAS, 410, 381

Buckley, J. H., Akerlof, C. W., Carter-Lewis, D. A., et al. 1998, A&A, 329, 639

Bykov, A. M., Chevalier, R. A., Ellison, D. C., & Uvarov, Y. A. 2000, ApJ, 538, 203

Bykov, A. M., Krassilchtchikov, A. M., Uvarov, Y. A., et al. 2008, ApJ, 676, 1050

Bykov, A. M., Malkov, M. A., Raymond, J. C., Krassilchtchikov, A. M., & Vladimirov, A. E. 2013, Space Sci. Revs., 178, 599

Caprioli, D., Kang, H., Vladimirov, A. E., & Jones, T. W. 2010, MNRAS, 407, 1773

Camus, N. F., Komissarov, S. S., Bucciantini, N., & Hughes, P. A. 2009, MNRAS, 400, 1241

Cardillo, M., Giuliani, A., & Tavani, M. 2012, in High Energy Gamma-Ray Astronomy, AIP Conf. Series, 1505, 221

Castelletti, G., Dubner, G., Brogan, C., & Kassim, N. E. 2007, A&A, 471, 537

Caswell, J. L., Murray, J. D., Roger, R. S., Cole, D. J., & Cooke, D. J. 1975, A&A, 45, 239

Cesarsky, D., Cox, P., Pineau des Forêts, G., et al. 1999, A&A, 348, 945

Chang, J., Adams, J. H., Ahn, H. S., et al. 2008, Nature, 456, 362

Chevalier, R. A. 1977, Supernovae, 66, 53

Chevalier, R. A. 1982, ApJ, 258, 790

Chevalier, R. A. 1999, ApJ, 511, 798

Chevalier, R. A., & Reynolds, S. P. 2011, ApJ, 740, L26

Cioffi, D. F., McKee, C. F., & Bertschinger, E. 1988, ApJ, 334, 252

Clay, J. (1927). "Title unknown". Proceedings of the Section of Sciences, Koninklijke Akademie van Wetenschappen te Amsterdam 30: 633.

Crutcher, R. M. 2012, ARA&A, 50, 29

de Jager, O. C., & Djannati-Ataï, A. 2009, in Neutron Stars and Pulsars, ed. W. Becker (Berlin: Springer), 451 (arXiv:0803.0116)

de Jager, O. C., Harding, A. K., Michelson, P. F., Nel, H. I., Nolan, P. L., Sreekumar, P., & Thompson, D. J. 1996, ApJ, 457, 253

Del Zanna, L., Amato, E., & Bucciantini, N. 2004, A&A, 421, 1063

Del Zanna, L., Volpi, D., Amato, E., & Bucciantini, N. 2006, A&A, 453, 621

Dermer, C. D. 1986, A&A, 157, 223

Dickman, R. L., Snell, R. L., Ziurys, L. M., & Huang, Y.-L. 1992, ApJ, 400, 203

Dodson, R., Lewis, D., McConnell, D., & Deshpande, A. A. 2003, MNRAS, 343, 116

Draine, B. T., & McKee, C. F. 1993, ARA&A, 31, 373

Draine, B. T. 2011, Physics of the Interstellar and Intergalactic Medium by Bruce T. Draine. Princeton University Press, 2011. ISBN: 978-0-691-12214-4,

Drury, L. O. 1983, Reports on Progress in Physics, 46, 973

Drury, L. O. 1991, MNRAS, 251, 340

Esposito, J. A., Hunter, S. D., Kanbach, G., & Sreekumar, P. 1996, ApJ, 461, 820

Fang, K., Kotera, K., & Olinto, A. V. 2012, ApJ, 750, 118

Felten, J. E. 1974, in IAU Colloq. 23: Planets, Stars, and Nebulae: Studied with Photopolarimetry, ed. T. Gehrels (Tucson: U. of Az. Press), 1014

Fesen, R. A., & Kirshner, R. P. 1980, ApJ, 242, 1023

Fernandez, D., Dalton, M., Eger, P., et al. 2013, Proc. of Rencontres de Moriond 2013, in press (arXiv:1305.6396)

Forman, M. A., & Drury, L. O. 1983, International Cosmic Ray Conference, 2, 267

Fujita, Y., Ohira, Y., Tanaka, S. J., & Takahara, F. 2009, ApJ, 707, L179

Gabici, S., Aharonian, F. A., & Casanova, S. 2009, MNRAS, 396, 1629

Gaensler, B. M., & Slane, P. O. 2006, ARA&A, 44, 17

Gelfand, J. D., Slane, P. O., & Zhang, W. 2009, ApJ, 703, 2051

Gratton, L. 1972, Ap&SS, 16, 81

Green, D. A., & Scheuer, P. A. G. 1992, MNRAS, 258, 833

Greisen, K. 1966, Physical Review Letters, 16, 748

Giuliani, A., Cardillo, M., Tavani, M., et al. 2011, ApJ, 742, L30

Helder, E. A., Vink, J., Bassa, C. G., et al. 2009, Science, 325, 719

Hester, J. J., Scowen, P. A., Sankrit, R., et al. 1995, ApJ, 448, 240

Hester, J. J., Stone, J. M., Scowen, P. A., et al. 1996, ApJ, 456, 225

Hester, J. J., Mori, K., Burrows, D., et al. 2002, ApJ, 577, L49

Hester, J. J. 2008, ARA&A, 46, 127

Hewish, A., Bell, S. J., Pilkington, J. D. H., Scott, P. F., & Collins, R. A. 1968, Nature, 217, 709

Heyer, M. H., & Brunt, C. M. 2004, ApJ, 615, L45

Hinton, J., Funk, S., Parsons, R., & Ohm, S. 2011, ApJ, 743, L7

Hollenbach, D., & McKee, C. F. 1989, ApJ, 342, 306

Hörandel, J. R. 2003, Astroparticle Physics, 19, 193

Hörandel, J. R. 2004, Astroparticle Physics, 21, 241

Iffrig, O., & Hennebelle, P. 2014, arXiv:1410.7972

Inoue, T., Yamazaki, R., & Inutsuka, S.-i. 2010, ApJ, 723, L108

Jun, B.-I. 1998, ApJ, 499, 282

Kamae, T., Karlsson, N., Mizuno, T., Abe, T., & Koi, T. 2006, ApJ, 647, 692

Kang, H., Ryu, D., & Jones, T. W. 1996, ApJ, 456, 422

Kargaltsev, O., & Pavlov, G. G. 2008, in 40 Years of Pulsars: Millisecond Pulsars, Magnetars and More, ed. C.G. Bassa, Z. Wang, A. Cumming, V.M. Kaspi (Melville, NY: AIP), 171

Kargaltsev, O., Rangelov, B., & Pavlov, G. G. 2013, arXiv:1305.2552

Katsuta, J., Uchiyama, Y., Tanaka, T., et al. 2012, ApJ, 752, 135

Kelner, S. R., Aharonian, F. A., & Bugayov, V. V. 2006, Phys. Rev. D, 74, 034018

Kennel, C. F., & Coroniti, F. V. 1984a, ApJ, 283, 694

Kennel, C. F., & Coroniti, F. V. 1984b, ApJ, 283, 710

Kim, C.-G., & Ostriker, E. C. 2015, ApJ, 802, 99

Komissarov, S. S., & Lyubarsky, Y. E. 2003, MNRAS, 344, L93

Komissarov, S. S., & Lyutikov, M. 2011, MNRAS, 414, 2017

Koo, B.-C., & Heiles, C. 1995, ApJ, 442, 679

Koo, B.-C., & Moon, D.-S. 1997, ApJ, 485, 263

Koo, B.-C., Lee, J.-J., Seward, F. D., & Moon, D.-S. 2005, ApJ, 633, 946

Kothes, R., Reich, W., & Uyanıker, B. 2006, ApJ, 638, 225

Lagage, P. O., & Cesarsky, C. J. 1981, ESA Special Publication, 161, 317

Lagage, P. O., & Cesarsky, C. J. 1983, A&A, 118, 223

Lee, J.-J., Koo, B.-C., Yun, M. S., et al. 2008, AJ, 135, 796

Lee, S.-H., Patnaude, D. J., Raymond, J. C., et al. 2015, arXiv:1504.05313

Li, H., & Chen, Y. 2010, MNRAS, 409, L35

Lorimer, D. R., & Kramer, M. 2012, Handbook of Pulsar Astronomy, by D. R. Lorimer , M. Kramer, Cambridge, UK: Cambridge University Press, 2012,

Malkov, M. A., & Drury, L. O. 2001, Reports on Progress in Physics, 64, 429

Malkov, M. A., Diamond, P. H., & Sagdeev, R. Z. 2011, Nature Communications, 2,

Malyshev, D., Cholis, I., & Gelfand, J. 2009, Phys. Rev. D, 80, 063005

Manchester, R. N., Hobbs, G. B., Teoh, A., & Hobbs, M. 2005, AJ, 129, 1993

Martizzi, D., Faucher-Giguère, C.-A., & Quataert, E. 2014, arXiv:1409.4425

Massaro, E. 1985, Ap&SS, 108, 369

Matheson, H., & Safi-Harb, S. 2010, ApJ, 724, 572

McKee, C. F., Hollenbach, D. J., Seab, G. C., & Tielens, A. G. G. M. 1987, ApJ, 318, 674

Mészáros, P. 2007, Astrophysics at Ultra-High Energies, 97

Mizuno, Y., Lyubarsky, Y., Nishikawa, K.-I., & Hardee, P. E. 2011, ApJ, 728, 90

Mori, M. 2009, Astroparticle Physics, 31, 341

Nicholas, B. P., Rowell, G., Burton, M. G., et al. 2012, MNRAS, 419, 251

Ohira, Y., Murase, K., & Yamazaki, R. 2011, MNRAS, 410, 1577

Ong, R., et al. 2009, talk at 31st ICRC (arXiv:0912.5355)

Pacholczyk, A. G. 1970, Radio Astrophysics (San Francisco: Freeman)

Pacini, F., & Salvati, M. 1973, ApJ, 186, 249

Plank Collaboration, Arnaud, M., Ashdown, M., et al. 2014, arXiv:1409.5746

Ptuskin, V. S., & Zirakashvili, V. N. 2005, A&A, 429, 755

Reach, W. T., Rho, J., & Jarrett, T. H. 2005, ApJ, 618, 297

Rees, M. J., & Gunn, J. E. 1974, MNRAS, 167, 1

Reynolds, S. P. 2003, preprint submitted to Proceedings of IAU Colloquium 192, 10 Years of SN1993J (Valencia, Spain, April 2003) (arXiv:astro-ph/0308483)

Reynolds, S. P., & Chevalier, R. A. 1984, ApJ, 278, 630

Reynolds, S. P., & Jones, F. C. 1991, International Cosmic Ray Conference, 2, 400

Reynolds, S. P. 1998, ApJ, 493, 375

Reynolds, S. P. 2008, ARA&A, 46, 89

Safi-Harb, S., Harrus, I. M., Petre, R., Pavlov, G. G., Koptsevich, A. B., & Sanwal, D. 2001, ApJ, 561, 308

Schmidt, G. D., Angel, J. R. P., & Beaver, E. A. 1979, ApJ, 227, 106

Schuster, P. M. 2014, Astroparticle Physics, 53, 33

Sedov, L. I. 1959, Similarity and Dimensional Methods in Mechanics, New York: Academic Press, 1959,

Seward, F. D., Tucker, W. H., & Fesen, R. A. 2006, ApJ, 652, 1277

Shikaze, Y., Haino, S., Abe, K., et al. 2007, Astroparticle Physics, 28, 154

Sironi, L., & Spitkovsky, A. 2009, ApJ, 698, 1523

Sironi, L., & Spitkovsky, A. 2011, ApJ, 741, 39

Slane, P., Chen, Y., Schulz, N. S., Seward, F. D., Hughes, J. P., & Gaensler, B. M. 2000, ApJ, 533, L29

Slane, P. O., Helfand, D. J., & Murray, S. S. 2002, ApJ, 571, L45

Slane, P., Helfand, D. J., van der Swaluw, E., & Murray, S. S. 2004, ApJ, 616, 403

Slane, P., Helfand, D. J., Reynolds, S. P., Gaensler, B. M., Lemiere, A., & Wang, Z. 2008, ApJ, 676, L33

Slane, P., Bykov, A., Ellison, D. C., Dubner, G., & Castro, D. 2014, Space Sci. Rev., 26

Stone, J. M., & Gardiner, T. 2007, ApJ, 671, 1726

Stone, E. C., Cummings, A. C., McDonald, F. B., et al. 2013, Science, 341, 150

Strong, A. W., Moskalenko, I. V., & Reimer, O. 2004, ApJ, 613, 962

Strong, A. W., Moskalenko, I. V., & Ptuskin, V. S. 2007, Annual Review of Nuclear and Particle Science, 57, 285

Sturner, S. J., Skibo, J. G., Dermer, C. D., & Mattox, J. R. 1997, ApJ, 490, 619

Talbot, A. 1979, Journal of the Institute of Mathematics and its Applications, 23, 97

Tang, X., & Chevalier, R. A. 2012, ApJ, 752, 83

Tang, X., & Chevalier, R. A. 2014, ApJ, 784, L35

Tang, X., & Chevalier, R. A. 2015, ApJ, 800, 103

Tavani, M., Giuliani, A., Chen, A. W., et al. 2010, ApJ, 710, L151

Temim, T., Gehrz, R. D., Woodward, C. E., et al. 2006, AJ, 132, 1610

Tian, W. W., & Leahy, D. A. 2013, ApJ, 769, L17

Toptygin, I. N. 1980, Space Sci. Rev., 26, 157

Torres, D. F., Marrero, A. Y. R., & de Cea Del Pozo, E. 2010, MNRAS, 408, 1257

Truelove, J. K., & McKee, C. F. 1999, ApJS, 120, 299

Uchiyama, Y., Aharonian, F. A., Tanaka, T., Takahashi, T., & Maeda, Y. 2007, Nature, 449, 576

Uchiyama, Y., Blandford, R. D., Funk, S., Tajima, H., & Tanaka, T. 2010, ApJ, 723, L122

Uchiyama, Y., & on behalf of the Fermi LAT collaboration 2011, Proceedings, 25th Texas Symposium on Relativistic Astrophysics (eds. F. Rieger & C. van Eldik), in press (arXiv:1104.1197)

Uchiyama, Y., Funk, S., Katagiri, H., et al. 2012, ApJ, 749, L35

van der Swaluw, E., Achterberg, A., Gallant, Y. A., & Tóth, G. 2001, A&A, 380, 309

van der Swaluw, E., Downes, T. P., & Keegan, R. 2004, A&A, 420, 937

van Dishoeck, E. F., Jansen, D. J., & Phillips, T. G. 1993, A&A, 279, 541

Van Etten, A., & Romani, R. W. 2011, ApJ, 742, 62

Vazquez-Semadeni, E. 1994, ApJ, 423, 681

Veron-Cetty, M. P., & Woltjer, L. 1993, A&A, 270, 370

Volpi, D., Del Zanna, L., Amato, E., & Bucciantini, N. 2008, A&A, 485, 337

Vink, J. 2012, A&A Rev., 20, 49

Weinberg, S. L., & Silk, J. 1976, ApJ, 205, 563

Weisskopf, M. C., Hester, J. J., Tennant, A. F., et al. 2000, ApJ, 536, L81

Wilson, A. S. 1972, MNRAS, 160, 355

Wolszczan, A., Cordes, J. M., & Dewey, R. J. 1991, ApJ, 372, L99

Woltjer, L. 1972, ARA&A, 10, 129

Xiao, L., Fürst, E., Reich, W., & Han, J. L. 2008, A&A, 482, 783

Yang, R.-z., de Oña Wilhelmi, E., & Aharonian, F. 2014, A&A, 566, A142

Zatsepin, G. T., & Kuz'min, V. A. 1966, Soviet Journal of Experimental and Theoretical Physics Letters, 4, 78